CATHODOLUMINESCENCE SPECTROSCOPY STUDIES OF ALUMINUM GALLIUM NITRIDE AND SILICON DEVICE STRUCTURES AS A FUNCTION OF IRRADIATION AND PROCESSING

DISSERTATION

Presented in Partial Fulfillment of the Requirements for the Degree Doctor of Philosophy

in the Graduate School of The Ohio State University

By

Brad Derek White, B.S., M.S.

****

The Ohio State University

2006

Dissertation Committee:

Dr. Leonard J. Brillson, Adviser

Dr. Wu Lu

Dr. Betty Lise Anderson

Approved by

_____

Adviser

Graduate Program in Electrical Engineering

ABSTRACT

Electronic device performance is critically dependent on the presence of deep-level and shallow states in the electronic band gap. A uniform or localized distribution of defects throughout a device structure can adversely affect doping and carrier transport, and result in changes to device saturation current, threshold voltage, ohmic contact resistivity, and Schottky barrier properties, including leakage currents. Process-induced atomic intermixing effects at heterostructure interfaces can cause decreases in sheet density and mobility of channel layers. For the presence of all such effects, the spatial variation across a given wafer can result in significant variation in device performance depending on spatial position. Spatially-resolved cathodoluminescence spectroscopy (CLS) has been used to identify the presence of radiative point and extended defects in the semiconductor band gap produced by irradiation and processing conditions for Si and GaN-based devices. Changes in deep level emission in Al-SiO_2-Si capacitor structures revealed a gradient in relative defect concentrations across the SiO_2 film after x-ray irradiation, indicating interface-specific defect creation. CLS measurements also revealed changes in the near-band edge signatures of AlGaN-GaN high-electron mobility transistor (HEMT) structures subjected to 1.8 MeV proton irradiation. These changes were indicative of alloying of AlGaN and GaN at the charge confinement interface and relaxation of piezoelectric strain in the AlGaN film. Alloying was investigated with secondary-ion mass spectrometry, which confirmed a broadened interface after a high

fluence of proton irradiation. Both mechanisms contributed to the measured degradation in HEMT channel transport properties. Ni-GaN Schottky barrier height decreases and ideality factor increases were observed at lower fluences than the degradation in HEMT channel figures. Additionally, 1.0 MeV protons resulted in ~1.5 times higher damage than 1.8 MeV protons, which was shown to be consistent with simulations of total non-ionizing energy loss for the two energies. The properties of Schottky contacts on AlGaN were also investigated for x_{Al}~0.4 versus pre-deposition surface cleaning procedure. Two inductively-coupled plasma reactive-ion etching (ICP-RIE) procedures were compared with a standard HCl etching routine. The ICP-RIE treated samples exhibited higher uniformity than the HCl surface, as characterized by electrical and CLS measurements. The presence of a spectral emission at ~4.08 eV in the HCl-etched piece correlated with the presence of a secondary Schottky barrier at ~1 eV. The emergence of a second spectral peak at ~4.05 eV after ICP treatment also resulted in pinned barriers near 1 eV. The addition of a pre-metallization rapid-thermal annealing process after the ICP-RIE treatment results in the disappearance of both peaks, and correlated with the best diode properties in terms of ideality factors and dependence on metal workfunction. The degree of surface pinning from interface states, inferred from plots of extracted barrier height versus metal workfunction, was characterized for all processing conditions. Estimated interface state density was reduced by an order of magnitude for the rapid-thermal anneal process. Lastly, temperature dependent CLS data was used to assign physical origins to the defects that control the Schottky barrier properties, including leakage currents. Nitrogen vacancies in the AlGaN are the most probable assignment for one, or both, peaks, with the presence of screw dislocations suggested by the data.

Dedicated to my parents, Harold and Marla White.

ACKNOWLEDGMENTS

This work would not have been possible without the guidance, facilities, financial support, and academic and industrial contacts of my advisor, Dr. Leonard Brillson. His enthusiasm for my results was always an encouragement.

Former and current group members Shawn Bradley, Gregg Jessen, Dennis Walker, Jr., and Min Gao are also acknowledged for useful discussions and invaluable technique and equipment knowledge. Gregg and his present group at Wright Patterson AFB, Sensors Directorate, have been most helpful for my project (as well as the projects of several other group members).

At OSU, Dr. Steve Ringel's group was very helpful for the Hall measurement and x-ray diffraction work, among other techniques. In particular, Andy Armstrong, Aaron Arehart, and Yong Lin are acknowledged. Mr. Jim Jones, Dept. of Elec. Eng., was also helpful countless times for a wide variety of experimental and facilities issues.

Drs. Ron Schrimpf and Dan Fleetwood and their student Aditya Karmarkar at Vanderbilt University were outstanding collaborators for the irradiation effects work. For these studies, Dr. Umesh Mishra's group at UC-Santa Barbara and Dr. Bill Schaff at Cornell provided excellent nitride samples.

For the Schottky barrier on AlGaN work, Dr. Amir Dabiran at SVT Associates, Even Prairie, MN, did me an enormous favor by growing a custom wafer structure. His efforts are greatly appreciated.

VITA

April 6, 1975……..……..…Born—Sellersville, PA USA

1997……..…….. B.S. Physics,
University of Missouri—Rolla

2002…… M.S. Physics,
The Ohio State University

2000-2006……...….. Graduate Research Associate,
The Ohio State University

1999-2000……..Physics Department Fellowship,
The Ohio State University

1998-1999…….……Process Engineer,
Intevac, Inc., Santa Clara, CA

PUBLICATIONS

Research Publications

1. Karmarkar, A.P., White, B.D., Fleetwood, D.M., Schrimpf, R.D., Weller, R.A., Brillson, L.J., and Mishra, U.K., "Proton-Induced Damage in Gallium Nitride-Based Schottky Diodes", *IEEE Trans. Nucl. Sci.* 52 (6): 2239-2244, 2005.

2. Mosbacker, H.L., Strzhemechny, Y.M., White, B.D., Smith, P.E., Look, D.C., Reynolds, D.C., Litton, C.W., and Brillson, L.J., "Role of near-surface states in ohmic-Schottky conversion of Au contacts to ZnO", *Appl. Phys. Lett.* 87 (1): 012102, 2005.

3. Karmarkar, A.P., Jun, B.G., Fleetwood, D.A., Schrimpf, R.D., Weller, R.A., White, B.D., Brillson, L.J., and Mishra, U.K. "Proton irradiation effects on GaN-based high electron-mobility transistors with Si-doped $Al_xGa_{1-x}N$ and thick GaN cap layers", *IEEE Trans. Nucl. Sci.* 51 (6): 3801-3806, 2004.

4. Hu, X.W., Karmarkar, A.P., Jun, B., Fleetwood, D.M., Schrimpf, R.D., Geil, R.D., Weller, R.A., White, B.D., Bataiev, M., Brillson, L.J., and Mishra, U.K., "Proton-irradiation effects on AlGaN/AlN/GaN high electron mobility transistors", *IEEE Trans. Nucl. Sci.* 50 (6): 1791-1796, 2003.

5. White, B.D., Bataiev, M., Goss, S.H., Hu, X., Karmarkar, A., Fleetwood, D.M., Schrimpf, R.D., Schaff, W.J., and Brillson, L.J., "Electrical, spectral, and chemical properties of 1.8 MeV proton irradiated AlGaN/GaN HEMT structures as a function of proton fluence", *IEEE Trans. Nucl. Sci.* 50 (6): 1934-1941, 2003.

6. Koide, Y., Walker, D.E., White, B.D., Brillson, L.J., Itoh, T., McCreery, R.L., Murakami, M., Kamiyama, S., Amano, H., and Akasaki, I., "Influence of oxygen on luminescence and vibrational spectra of Mg-doped GaN", *Phys. Stat. Solidi B* 240 (2): 356-359, 2003.

7. Jessen, G.H., Fitch, R.C., Gillespie, J.K., Via, G.D., White, B.D., Bradley, S.T., Walker, D.E., and Brillson, L.J., "Effects of deep-level defects on ohmic contact and frequency performance of AlGaN/GaN high-electron-mobility transistors", *Appl. Phys. Lett.* 83 (3): 485-487, 2003.

8. White, B.D., Bataiev, M., Brillson, L.J., Choi, B.K., Fleetwood, D.M., Schrimpf, R.D., Pantelides, S.T., Dettmer, R.W., Schaff, W.J., Champlain, J.G., and Mishra, U.K., "Characterization of 1.8-MeV proton-irradiated AlGaN/GaN field-effect transistor structures by nanoscale depth-resolved luminescence spectroscopy", *IEEE Trans. Nucl. Sci.* 49 (6): 2695-2701, 2002.

9. White, B.D., Brillson, L.J., Bataiev, M., Brillson, L.J., Fleetwood, D.M., Schrimpf, R.D., Choi, B.K., Fleetwood, D.M., and Pantelides, S.T., "Detection of trap activation by ionizing radiation in SiO2 by spatially localized cathodoluminescence spectroscopy", *Jour. Appl. Phys.* 92 (10): 5729-5734, 2002.

10. Koide, Y., Walker, D.E., White, B.D., Brillson, L.J., Murakami, M., Kamiyama, S., Amano, H., and Akasaki, -I., "Simultaneous observation of luminescence and dissociation processes of Mg-H complex for Mg-doped GaN", *Jour. Appl. Phys.* 92 (7): 3657-3661, 2002.

11. Jessen, G.H., White, B.D., Bradley, S.T., Smith, P.E., Brillson, L.J., Van Nostrand, J.E., Fitch, R., Via, G.D., Gillespie, J.K., Dettmer, R.W., and Sewell, J.S., "Ohmic contact characterization of AlGaN/GaN device layers with spatially localized LEEN spectroscopy", *Sol.-Stat. Elec.* 46 (9): 1427-1431, 2000.

12. White, B.D., Brillson, L.J., Lee, S.C., Fleetwood, D.M., Schrimpf, R.D., Pantelides, S.T., Lee, Y.M., and Lucovsky, G., "Low energy electron-excited nanoscale luminescence: A tool to detect trap activation by ionizing radiation", *IEEE Trans. Nucl. Sci.* 47 (6): 2276-2280, 2000.

13. Brillson, L.J., Young, A.P., White, B.D., Schafer, J., Niimi, H., Lee, Y.M., and Lucovsky, G., "Depth-resolved detection and process dependence of traps at ultrathin plasma-oxidized and deposited SiO2/Si interfaces", *Jour. Vac. Sci. Tech. B* 18 (3): 1737-1741, 2000.

FIELDS OF STUDY

Major Field: Electrical Engineering
Physical Electronics

TABLE OF CONTENTS

Page

LIST OF TABLES

LIST OF FIGURES

CHAPTER 1

INTRODUCTION AND BACKGROUND

1.1 Gallium-nitride based devices

III-Nitride devices have attracted much interest in recent years for optoelectronic and high-power electronics applications. Alloying InN (room temperature bandgap 0.7 eV) with GaN (3.4 eV) and the latter with AlN (6.2 eV) comprises a spectral range from infrared to ultraviolet, and has resulted in the commercial production of blue LED structures, which were previously unattainable.[1] The large bandgaps of GaN and AlN imply these materials are suitable for high temperature applications compared to Si and GaAs (bandgaps 1.1 and 1.4 eV), since the transition to the intrinsic carrier concentration regime does not occur until much higher temperatures. Additionally, the high bond strengths for the constituent atoms in the nitride series, as compared with their counterparts in the arsenide or phosphide systems, for example, imply a high decomposition temperature[2] and relative hardness to particle irradiation.[3,4]

GaN and alloys exhibit unintentional n-type doping, arising mainly from nitrogen vacancies and unintentional impurity inclusion during growth. In recent years, improvements in growth quality have resulted in unintentional electron concentrations below the 10^{17} cm^{-3} range.[5] The intentional donor in GaN and (In,Al)N alloys is Si, which has been successfully implemented to controllably yield electron concentrations in

excess of 10^{19} cm^{-3} for the system. For AlGaN alloys with Al mole fraction <40%, the Si level in the bandgap is suitably shallow (i.e., close to the conduction band edge, <30 meV) as to yield complete activation of the dopant at room temperature.[6] The high doping capability combined with the high temperature figure of the system suggests suitability for high power applications, which require high current densities and exhibit elevated operating temperatures due to resistive heating. Additionally, high breakdown fields also allow for high power applications.[7] Furthermore, the high electron mobilities (i.e., drift velocity per applied electric field) observed in bulk GaN and alloys allows for high frequency operation of devices.

The combined power and frequency figures make the nitride system particularly attractive for long distance radio-frequency communication applications, as high power is required to transmit signals large distances. The radiation hardness adds an additional advantage for space and high altitude applications. The basic unit of power amplification circuitry is the transistor, and research has focused on GaN metal-semiconductor field effect transistor (MESFET) structures. In this device, a thin film of low resistivity GaN is epitaxially grown on an insulating substrate, and the conductive GaN layer forms the transistor channel. Current is passed through the channel by deposited metal ohmic source and drain contacts, and the channel is modulated on and off by the varying the voltage to a reverse biased Schottky (i.e., rectifying) metal contact between the source and drain. Application of increasing reverse biases to the Schottky contact increases the GaN conduction band energy relative to the Fermi level in the material, thus reducing the electron concentration in the band. A sufficiently high reverse bias effectively reduces the conduction band population to zero, and electron conduction ceases.[8] Using the

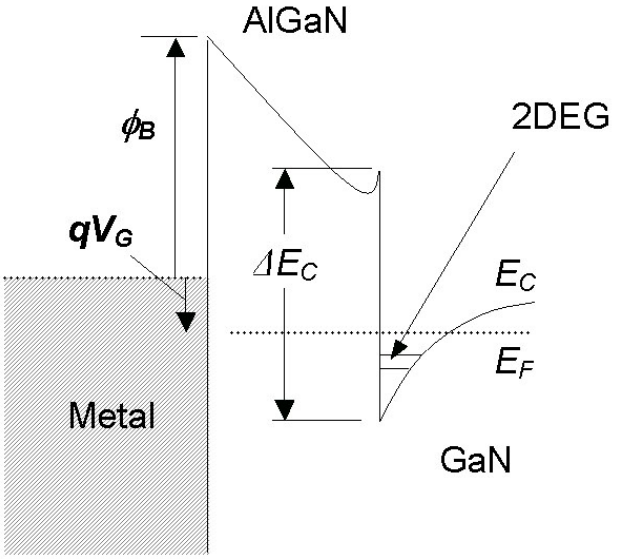

Figure 1.1. AlGaN-GaN HEMT band diagram. The 2DEG is populated when the conduction band at the AlGaN/GaN interface is below the Fermi level.

MESFET design on GaN, operating frequencies of ~28 GHz (unity gain) and current densities of ~1 A/cm have been reported.[9]

High frequency and power operation has also been achieved by the implementation of nitride based high-electron mobility transistor (HEMT) structures. In the device, pictured in Figure 1.1, a thin AlGaN film (mole fraction <0.35) is grown on top of a thick GaN layer. The high conduction band offset at the AlGaN/GaN heterointerface results in a depletion region in the AlGaN film and a corresponding accumulation layer in the GaN, near the interface. These accumulation electrons form the channel and are referred to as a two-dimensional electron-gas (2DEG).[10] High piezoelectric constants in the system result in an enhancement of the 2DEG layer to charge densities in excess of 10^{13} cm^{-2} at room temperature.[11] A significant advantage of 2DEG structures is high channel mobilities. Recent nitride HEMTs have exhibited electron mobilities near 2000 cm^2/Vs at room temperature.[12] As with the MESFET, the

source and drain contacts are formed directly on the AlGaN, and a Schottky barrier serves as the gate. For sufficiently high reverse biases on the gate, the 2DEG layer is extinguished by raising the channel energies above the Fermi position, and the channel flow is terminated.

The high power operation of the HEMTs requires ohmic contacts with low contact resistivity, to avoid power losses and heating effects at this metal-semiconductor interface. Specific resistivities $<10^{-7}$ Ω/cm^2 have been realized on n-type GaN using a multiple metal scheme consisting of (in order of deposition) Ti/Al/"x"/Au, with common "x" metals Ti, Pt, Mo, and other refractories. In this scheme, the first layer is a thin (~200Å) Ti layer, which upon rapid thermal annealing (typically ~850°C for ~30 sec.) removes nitrogen from the semiconductor through a chemical reaction forming TiN, leaving the resulting semiconductor locally highly n-type due to the presence of new nitrogen vacancies. This enhancement of effective doping in the immediate vicinity of the contact promotes a high degree of tunneling current (see Section 6.2), and results in a low contact resistance. The Al layer (typically 500Å) prevents excessive Ga outdiffusion from the semiconductor. The refractory (~1000Å) prevents oxidation of the Al, and is typically chosen to minimize visible morphological changes to the contact upon the annealing step, which may introduce errors into subsequent photolithography alignments. Furthermore, the thermal stability of this layer is important during high-power operation of the device after fabrication. The final Au layer (usually >500Å) facilitates wire bonding to the finished device. Optimized ohmic schemes have been shown to exhibit thermal stabilities in excess of 120 hours at 500°C.[13]

Schottky metals have primarily been chosen for their high workfunctions, which should result in large barrier heights. An advantage of high barrier heights for Schottky transistor gates is the low leakage (i.e., reverse) current observed from the gate to the channel when the channel current is off. This is an important effect contributing to power losses in the device. Moreover, gate leakage current is a main contributing factor to high frequency noise in HEMTs.[14,15]

1.2 Radiation effects overview

Charged particles trapped in Earth's radiation belts can penetrate spacecraft if sufficiently energetic.[16] This can result in ionization events in spacecraft electronics which may not be reversible. Cosmic rays and secondary ions can result in burnout of critical integrated circuits or an increased error rate from upset events.[17] Much work has been concentrated on assigning system level failure analysis and total dose hardness for classes of circuits, but comparatively little work has been done to clarify exact mechanisms of failure for many specific devices. Failure modes at the device level include cumulative effects such as resistivity and Fermi position changes from the formation of compensating point defects[18], changes to the electrical contacts, as well as more catastrophic mechanisms such as device burnout and other abrupt mechanisms. These abrupt failures have been attributed to solar events with very high doses of radiation in short periods.

In general, particle irradiation (e.g., protons) is more likely to create point defects, such as vacancies, in a material, although high energy ionizing irradiation (e.g., x-rays and γ-rays) can also create defects in less radiation tolerant materials. For each class of

devices, it is important to assign specific failure modes to determine what steps, if any, can be taken to make a device more radiation tolerant. The ability to characterize individual device layers and specific regions, such as near the electrical contacts, is highly important for determining precise irradiation-induced damage effects.

In general, gallium nitride and related alloys are assumed to be two orders of magnitude harder than corresponding gallium arsenide materials[19], but the effects of irradiation on the heterointerfaces and electrical contacts have not been well characterized for particle irradiation of GaN and related materials.

1.3 Processing effects overview

Specific growth procedures can have large effects on material and device quality. For example, for several materials there have been direct correlations of device performance with the presence of extended defects originating from the degree of lattice-mismatch for a substrate and epilayers grown above it.[20,21] Inclusion of defects during material growth and subsequent processing can change the local carrier concentration and adversely affect device performance. Surface processing can also have large effects on the resulting device. If there is a large density of surface states, the performance of electrical contacts and buried device layer performance can be adversely affected.[22] Processing effects are generally not well understood for novel material systems, and the empirical relations derived for previous systems may not be valid of the new case. For example, surface processing techniques are well understood for established technology, such as III-arsenides, but not for a novel system, such as III-nitrides. As established techniques are imported into the new system, the effects of these techniques will need to

be characterized. An example of such a technique is plasma etching technology for recessed-gate applications. The effects of this process on III-nitride alloys have not been thoroughly documented.

Another detrimental factor to device performance is high temperature effects. Continuous operation for prolonged periods at elevated temperatures can cause changes to the material and electrical contacts. For example, a well known effect in gallium arsenide transistors is gate sinking, where the gold gate layers migrate into the semiconductor at high temperatures, causing very high leakage currents and ultimately device failure.[23] Measuring operating temperatures to establish appropriate testing conditions is challenging, and numerical models may be inaccurate in estimating temperatures accurately. Ideally, any novel process should be assessed in the context of temperature stability, as well as common device figures obtained.

1.4 Research outline

A radiation-effect test case is given in Chapter 3. There, SiO_2 capacitor structures were irradiated with x-rays, and localized interfaces were probed for degradation effects. Chapters 4 and 5 describe particle irradiation effects in nitride transistor structures. The changes in electrical performance are explained by characterizing changes to the material. Chapter 5 suggests degradation of the Schottky contacts, and changes to Ni-GaN contacts is explored in detail in Chapter 6 for low energy proton irradiation. Chapters 7 and 8 are devoted to the fabrication of Schottky barriers on AlGaN for numerous metals versus three surface treatment conditions. Chapter 7 pertains to the electrical performance of the barriers, and the Chapter 8 data suggest physical mechanisms to account for the

difference between three processing cases. The main characterization technique used in this study is cathodoluminescence, which is described in detail in Chapter 2. Other techniques are employed where appropriate and feasible, and they are described in the appropriate chapter, as needed.

CHAPTER 2

CATHODOLUMINESCENCE

2.1 Introduction

Cathodoluminescence is main technique used in this report, and it is common to all systems studied. It is therefore described in detail in this chapter. Other techniques are described as needed in subsequent chapters.

Cathodoluminescence is the electron-excited analogue to photoluminescence. Electrons incident upon a sample generate electron-hole pairs, and the recombination of these carriers include luminescent transitions to states in the bandgap. These recombination transitions may include direct band-to-band, dopant-to-band, donor-acceptor, or deep point and extended defect transitions in the semiconductor.[24] With photoluminescence, the formation of electron-hole pairs is not possible for semiconductors with a bandgap in excess of the excitation energy of the photons. This limitation is absent in cathodoluminescence, and in practice probing large direct bandgap materials is limited principally by optical transmission limitations in the analysis equipment. Another significant advantage of cathodoluminescence is the depth dependence of incident electrons as a function of beam energy. By tuning the electron beam energy from hundreds of eV to a few keV, the electron-hole pair generation depth can be varied from tens of nanometers to about a μm, for practical beam energies.

Analytical expressions predict the peak electron stopping depth, and hence optical recombination vuolume, to vary $E_B^{1.75}$.[25] By noting the beam energy dependence of luminescence intensities of spectral features, these features can be associated with a particular layer or interface of a heterostructure, in accordance with the predicted penetration depth of the beam. Additionally, the shallow excitation depths achieved using low beam energies (~500 eV or less) provides a direct probe of the surface of the material, and may indicate the presence of near-surface defects on a scale of a few nm. This provides a distinct advantage over many competing techniques, such as photoluminescence, where typical characteristic absorption lengths are on the order of a micron and are fixed for a given optical excitation energy.

The number of electron-hole pairs created depends on the ionization energy of the material, which is empirically given by $E_i = 2.8E_g + M$, where E_g is the bandgap and M varies from 0 to 1 eV.[26] The generation rate of electron-hole pairs has been estimated by:[27]

$$G = V_B I_B (1-\gamma)/eE_i \tag{2.1}$$

where V_B is the beam voltage, I_B is the beam current, γ is the backscattered loss coefficient, and e is the electron charge. Assuming typical γ values are small, for a 10 keV, 1 nA beam (typical values for a scanning electron microscope), the generation rate of electron-hole for E_g ~ 3.0 eV is ~10^{12} s^{-1}. Should even a small fraction of these recombine radiatively, conventional photon detection equipment should be able to resolve the luminescence from such transitions. In this way, cathodoluminescence should

be sensitive to even a small density of radiative states in the bandgap of a semiconductor.

Using cathodoluminescence, evolution of spectral emissions and lineshapes has been observed as a function of material processing, thermal annealing, and radiation-induced degradation, among other applications, and has shed insight into physical mechanisms responsible for electrical degradation.[4,28,29]

2.2 Penetration depth of the electron beam

An analytical model developed by Everhart and Hoff predicts the stopping length, and in turn the excitation depth, of the electron beam. The model uses the following relation for the electron energy loss per unit length in the material:

$$\frac{\partial E}{\partial s} = -(2\pi N_A e^4)(Z\rho/A)(1/E)\ln(aE/I) \tag{2.2}$$

where N_A is Avagadro's number, Z is the atomic number of the matieral, ρ is the density, A is the gram atomic weight, I is the mean excitation energy, E is the beam energy, and a=1.166. Using this model, the maximum range for the electron is given by:

$$R_B = \int_o^{\xi(E_B)} \frac{\xi}{\ln(\xi)} \partial(\xi) \tag{2.3}$$

where ξ=aE/I. Empirically, the range is given, in microns, by

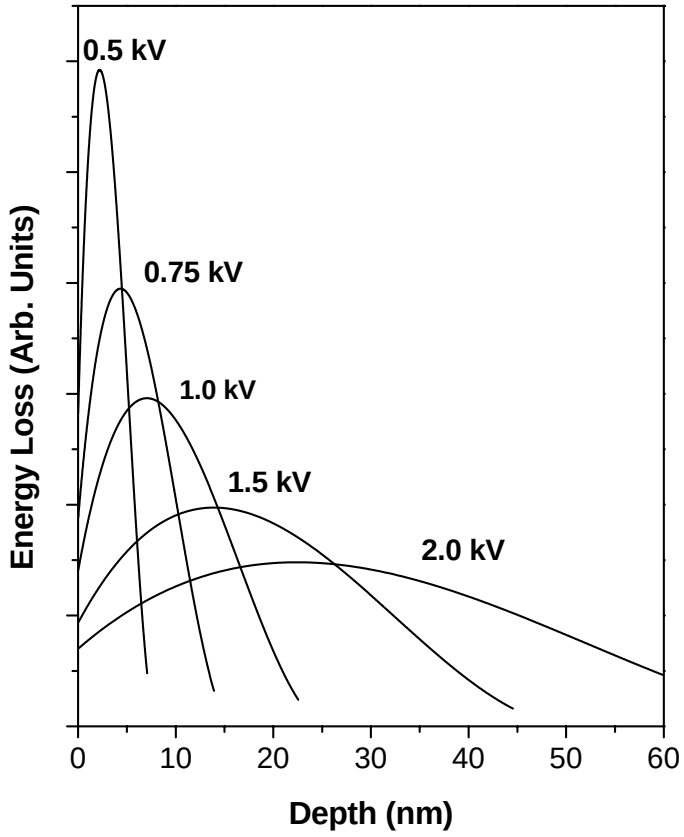

Figure 2.1. Predicted depth-dose curves using the Everhart-Hoff model, for GaN. The curves are from Ref. 30.

$$R_B = (0.0398/\rho) \times E^{1.75} \tag{2.4}$$

In the paper, Everhart and Hoff present a universal depth dose function for generating energy loss curves for any electron beam energy. The function is empirical and given as $g(z) = 0.6 + 6.21\ z - 12.40\ z^2 + 5.69\ z^3$. Here, $0<z<1$ and the z values are normalized to the range, R_B. A plot of the Everhart-Hoff predicted depths for gallium nitride is shown in Figure 2.1.[30] In this figure, the low energy curves are shown to be

highly surface sensitive, with the 500 eV beam excitation volume less than 10 nm into the sample.

The Everhart-Hoff model has been shown to be generally accurate for beam energies 1-25 keV, but for very low beam energies the predicted depth becomes less accurate. With modern computing power available, Monte-Carlo-based stopping power simulations of beam interaction can be used on a specific-case basis to predict excitation volumes, particularly in cases of multi-layered structures such as semiconductor heterostructures, which may include thin metal contacts. In these programs, the material density is added for each layer in the heterostructure, and collision events are computed using a random number generator for each collision until the electron comes to rest. The process is repeated for a large number of electrons, and a smooth energy loss curve can be generated. CASINO[31] is one such Monte Carlo simulator that is widely used to model depth curves. This program is used in the work in this report. The Monte Carlo techniques, which are expected to be more accurate than the simplified Everhart-Hoff model, tend to predict somewhat deeper penetration depths, although 500 eV and 1 keV beams are almost always shallow, being <10 and <20 nm for most matierals, respectively.

2.3 Micro-cathodoluminescence spectroscopy using a scanning electron microscope

A scanning electron microscope collects secondary electrons ejected from the surface of a material due to an energetic primary electron beam (typically keV). The secondary electrons are accelerated to a phosphor-coated collector which then fluoresces. The fluorescence is collected and converted to an electrical signal by a photomultiplier.

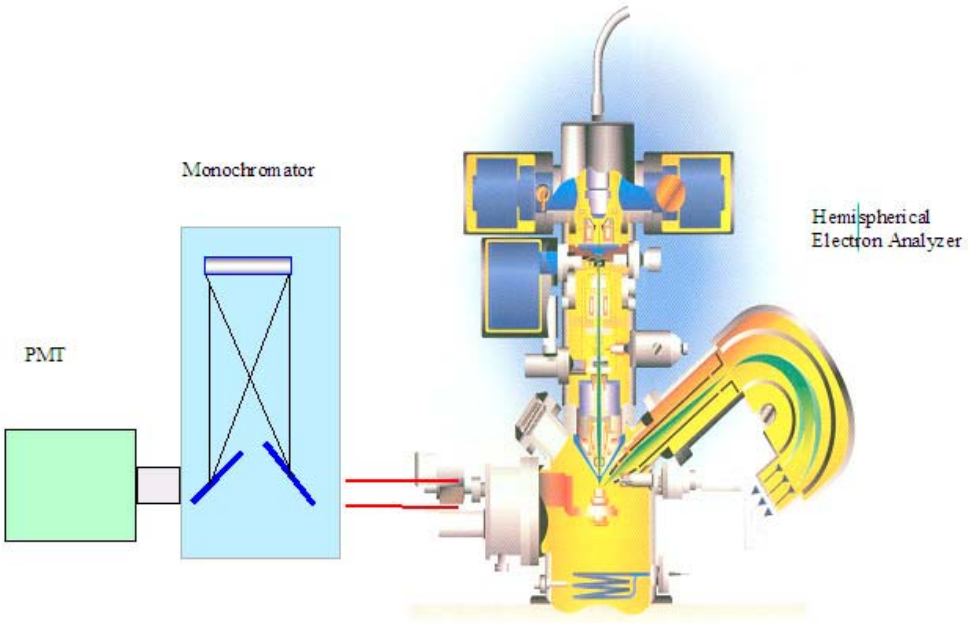

Figure 2.2 A Schematic of the JEOL 7800F SEM (right) and block figures of the Oxfird monochromator and PMT detector. The helium-cooled sample stage is not pictured.

By correlating this signal with the raster of the primary electron beam, an image is created. A primary advantage of electron microscopy is the high spatial resolutions permitted by using electrons, as compared with the standard diffraction limit of optical microscopes (~μm). The diffraction limit of keV electrons is much smaller, and the practical limitation on spatial resolution is determined principally from electron optics. Typical resolutions are hundreds of nanometers, and under certain beam conditions less than 10 nm resolution can be obtained.

The instrument used in this report is a JEOL JAMP 7800F field emission Auger micropobe. It is fitted with an Oxford Instruments MonoCL cathodoluminescence attachment and variable temperature helium-cooled sample stage. The Oxford apparatus

consists of a hemispherical polished aluminum mirror with a small hole through which the electron beam passes to the sample. Light generated in the sample is collected by the mirror and directed down a tube a passed out a vacuum window to a monochromator/PMT assembly. The maximum spectral resolution is 0.15 nm and the detection range is approximately 200-1000 nm. A high sensitivity germanium detector attachment is also available, which extends the spectral range to ~1600 nm. The sample stage can be cooled to ~10 K and is temperature-controllable to RT. The SEM beam can be controlled from ~500 eV to 25 keV with beam currents from 10^{-10} to 10^{-8} A (closer to the lower limit for beam energies less than ~2 keV). A schematic of the setup is pictured in Figure 2.2.

2.4 Comparison with photoluminescence and deep-level transient spectroscopy

Two other common techniques for monitoring point and extended defects and impurities in semiconductors are photoluminescence and deep-level transient spectroscopy (DLTS). There are three main advantages to cathodoluminescence over these techniques:

(1) Tunable depth dependence of excitation/recombination depth through varying the beam energy. The excitation depth of PL is not tunable for a given laser energy. DLTS, in addition to needing a fabricated diode with low leakage currents, can not sense shallower than the depletion width, which can be very large for lightly doped semiconductors.

(2) Wide bandgap compatibility. This is a clear advantage over photoluminescence, which is constrained by the laser excitation energy. In principle,

cathodoluminescence is constrained only by the detection optics. Indeed, recombination from the AlN near-bandedge (energy ~6.2 eV) has been observed using the equipment in this study.[32]

(3) Good spatial resolution. Since the diffraction limit of ~keV electrons is very small (wavelength < 1Å), the practical limitations to the resolution of CL are the beam spreading and minority carrier diffusion length. This is in contrast with PL, which is diffraction limited at the wavelength (~100's of nm) and DLTS, which is limited by the diode area. For scanning electron microscope studies, as performed here, the beam spreading issues are minimal, with the theoretical smallest beam size less than 5 nm for 25 keV electrons. For lower energy beams, the resolution is still 50 nm or less. Furthermore, for all but the highest quality samples with very low defect densities, or very light doping in the semiconductor, the minority carrier diffusion length is typically manageable.

CHAPTER 3

SPATIALLY-RESOLVED X-RAY IRRADIATION EFFECTS IN Si-SiO2 CAPACITOR STRUCTURES

3.1 Introduction

The design of microelectronic structures with improved resistance to the effects of space radiation involves the understanding and control of electrically active defect states that are created in the active regions of the device. In turn, such control requires understanding how the properties of such defects depend on the local chemical bonding environment and how ionizing radiation activates these defects. The spatial distribution of defects within the device structure can provide information on the microscopic formation and electronic evolution of such defects due to irradiation.

Thin oxide gate and isolation structures provide a good test system for identifying spatially localized radiation degradation mechanisms. Highly pure and uniform oxides can be grown under controlled oxidation conditions, and the resulting metal-oxide-semiconductor systems are well characterized and reproducible. Moreover, SiO_2 structures have direct relevance for radiation environments, as silicon based circuits are used extensively in the electronics systems of high altitude aircraft and space satellites. For this reason, reliable cumulative dosage figures have been previously determined, and component and device failure mechanisms have been the topic of much investigation, with an emphasis towards component failure. Study of the creation of radiation-induced

traps at the device level adds physical insight into specific mechanisms of failure. In particular, studies of the spatial localization of radiation damage in the SiO_2 structure add new information to the understanding of such radiation effects.

Cathodoluminescence spectroscopy (CLS) has been previously used to provide evidence for electronic traps in thin oxide structures. Depth-localized CLS can measure defects within SiO_2 ultrathin films and at SiO_2 thin film interfaces, as well as their change under process conditions.[33] Micro-CLS measurements often reveal new features associated with local interfaces.[34] There have been many CLS studies of defects in SiO_2, and their optical features in various forms of silica have been catalogued.[35] Extensive electron spin resonance studies of point defects in SiO_2 provide correlations between CLS optical features and the bonding nature of the corresponding point defects.[36,37,38,39,40] These and other studies reveal the presence of several defects common to most SiO_2 films, regardless of growth procedure. These common features include prominent emissions at ~1.9 and ~2.7 eV. The broad feature at 1.9-2.0 eV has been attributed to *a*-SiO_x bonding environments, interface microstructure, or associated point defects of the otherwise crystalline substrate. Broad features peaking at 1.9 eV or above are also reported for porous and hydrogenated amorphous Si films.[41] The 2.7 eV feature has been reported previously in crystalline SiO_2, amorphous SiO_2, SiO_x, and SiO_x at thermally-grown SiO_2-Si interfaces. It is associated either with self-trapped excitons, two-fold coordinated Si, or O vacancies. This E' center represents the most important trap center in silicon oxides and has been modeled to involve an unpaired electron localized on a Si atom back-bonded to three O atoms.[38]

In previous experiments, CLS has been specifically used to monitor the changes of defects in SiO_2 structures in response to electron or X-ray irradiation.[36,37,38,39,40] For these studies, the SiO_2/Si specimens consisted of a 10 Ohm-cm, B-doped p-type (100) Si substrate, an interfacial oxide layer 0.5-0.6 nm thick prepared by remote plasma assisted oxidation, followed by a 5.0 nm remote plasma enhanced chemical vapor deposition (RPECVD) carried out at 300°C.[42] X-ray irradiation was performed at Vanderbilt University with a 10 keV X-ray source. Fig. 3 illustrates the effects of 10 keV, 7.6 Mrad(SiO_2) [13.7 Mrad(Si)] and 15.2 Mrad (SiO2) X-ray irradiation on the optical emission is these structures in the near Si-SiO2 interface region. The prominent features in all spectra are the 1.9 and 2.7 eV emissions discussed previously. No significant changes are evident after the 7.6 Mrad (SiO_2) irradiation, and low energy CLS (1 and 2 keV beam energies, corresponding to the near-SiO_2 surface) shows no significant differences. However, the additional 7.6 Mrad irradiation of this specimen produces a significant increase of the 2.7 eV peak for the 3 keV beam energy. This energy corresponds to a beam excitation depth of just past the Si-SiO_2 interface, away from the bare surface. The spectra are shown with their absolute intensity, corrected only for the spectral response of the optical train. The multiple curves for the same energy in each panel of Figure 3.1 illustrate variations (~$\pm$8%) in spectra from point to point across the surface under identical conditions, separated only by millimeters or less. The relative increase in 2.7 eV emission apparent for the 15.2 Mrad irradiation case, increasing relative to the unirradiated case by over 20% for both 3 keV and 4 keV. The 15.2 Mrad

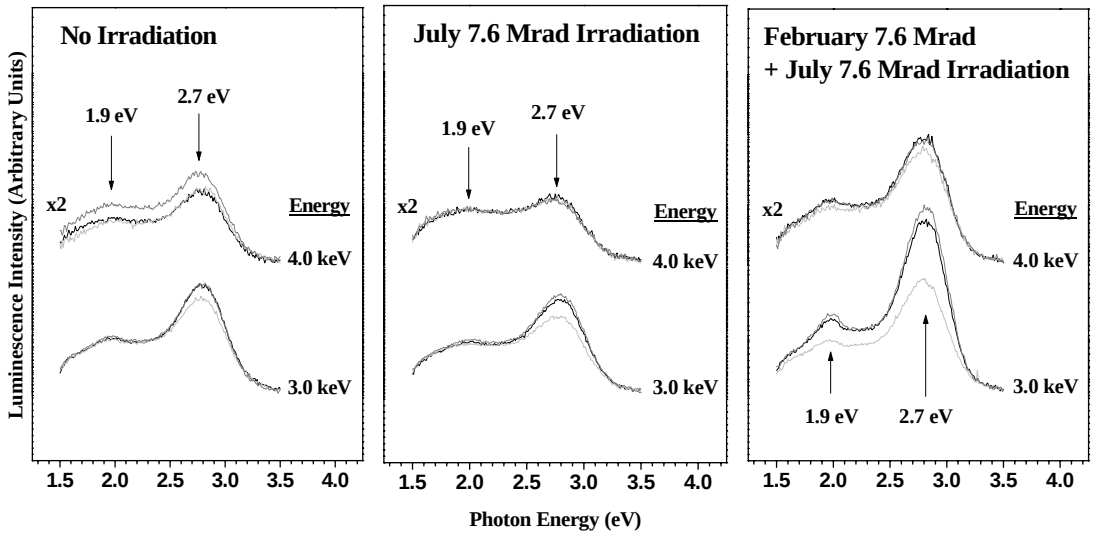

Figure 3.1. Depth-resolved spectra of ultra-thin SiO_2/Si interfaces 9-11 days after receiving the samples. No irradiation (left), 10 keV X-ray, 7.6 Mrad irradiation (middle), and 15.2, 10 keV x-ray irradiation (right). Different curves for the same energy indicate variations from point to point across SiO_2/Si free surface. All three sets of spectra exhibit peak features at 1.9 eV and 2.7 eV. A clear increase in 2.7 eV peak height is evident at 3 keV for the highest dose.

panel also indicates somewhat sharper emission spectra at 1.9 eV than in previous spectra, suggesting more than one origin for emission at these energies. Since this excitation occurs near the SiO_2/Si interface in all these spectra, and few if any new point defects are expected to be created by 10 keV X-ray irradiation in the bulk Si, this result suggests that the emissions occur from traps localized near the SiO_2/Si interface. Candidates for the post-irradiation peak at 1.9 eV are NBOHC or P_b centers (see below). Such traps have been observed in thin oxides using cathodoluminescence and reduced after annealing in previous studies, suggesting a common origin for both irradiation and interface bonding defects, namely Si dangling bonds at the interface.[43] These traps likely

result from the migration of H to the interface and its subsequent reaction with Si-H bonds.[44] The post-irradiation peak at 2.7 eV is also consistent with a common origin for irradiation and interface bonding defects, possibly due to electromigration of mobile hydrogen-associated defects within the SiO_2 film and across the Si interface.[45]

3.2 Growth and experimental procedure

Here, CLS has been implemented with a scanning electron microscope (SEM) to measure the optical emissions of defects within Al-SiO_2-Si gate dielectric structures, their spatial variations, and the effects of irradiation. The study of defects in SiO_2 in localized regions presents a significant challenge since electrons can introduce or alter defect features at sufficiently high doses.[45,46,47] The spatially-resolved measurement of optical emission due to traps formed at different bulk and interfacial regions of a MOS structure represents a novel approach to radiation studies. Thick oxides (~1 μm) were chosen to permit a clear discrimination of the metal and semiconductor interfaces.

The CLS experiment consists of the UHV SEM/optical collection system described in Chapter 2. Nominal spectral resolution was 2 nm and instrument response was slowly varying and monotonic in the spectral region of interest. The samples were cleaved ex-situ and mounted in an edge-on orientation to obtain cross-sectional SEM images. With this analysis method, all bulk and interfacial regions of interest are directly observable on the SEM image, and the electron beam can be selectively placed to obtain localized optical emissions from these regions. For all samples, optical emissions are characterized in the spectral range of 300-800 nm. In all cases the SEM electron beam energy was 10 keV, which corresponds to a median penetration depth of ~500 nm beyond

the cleaved surface. This implies that any observed luminescence originates from beneath the cleaved surface in material that was not exposed to any ex-situ contaminants. The 10 keV electron beam has a nominal 50 nm diameter spot size for beam currents employed in this study. The electron beam was operated in "scanning" mode inside a region defined by a square of ~200 nm per side, with an incident beam current of 0.5 nA.

Previous studies of SiO_2 showed[33,43] that the electron beam can alter optical emission intensities with cumulative dosage. The 0.5 nA beam current was carefully chosen such that the emission intensities were not affected during the length of an individual scan (~300 sec.). In general, the Si/SiO_2 system exhibits weak luminescence signals (~500 counts per second in this study), requiring multiple scans to achieve good signal-to-noise ratios. Successive scans were taken in adjacent spatial regions to assure there are no electron beam effects. Successive spectra taken at different lateral positions along the same interface were highly reproducible, confirming our ability to align the electron beam precisely. All figures shown in this study reflect an averaging of at least five successive spectra taken at different lateral positions.

The samples studied here were thick oxides grown under 1100 °C wet oxidation conditions.[48] The samples were comprised of structures consisting of patterned gate Al/1.05 μm SiO_2/ Si ($n=10^{15}$ cm^{-3}) MOS capacitors, the C-V curves for which were shifted by ~ 20 V after irradiation (total dose = 0.58 krad (SiO_2) with 10 keV x-rays). This shift corresponds to an effective areal charge density of ~ $4x10^{11}$ cm^{-2}, as extracted from capacitance-voltage measurements, projected to the interface. A nominal +0.5 MV/cm field was applied to the oxide during x-ray irradiation, by applying voltage from the Al gate to the metallization on the back of the specimen. Irradiation was performed at

Vanderbilt University and the samples were then immediately sent to Ohio State for spectroscopic analysis. All samples were analyzed as quickly as possible after arrival (less than seven days) to minimize any time degradation in radiation effects, and were not electrically biased during spectroscopic analysis. For each sample, a small amount of silver paste was applied from the aluminum metallization on the SiO_2 film to the sample mount, thereby providing an electrically conductive path to ground. This method was effective for minimizing charging effects observed in our SEM images, and allowed for a precise positioning of the electron beam for the duration of each spectral scan.

All results from irradiated samples were compared to results from reference samples that were not irradiated. The 10 keV incident electron beam provided the spatially-localized excitation for the CLS measurements in cleaved cross sectional view. The reference and irradiated samples were taken from the same wafer. All spectra were performed at room temperature (300 K).

3.3 Cross-sectional cathodoluminescence results

The cross section resulting from ex-situ wafer cleaving exposed cross sections of both Al-SiO_2-Si and SiO_2-Si interfaces at different locations along the cleaved wafer edge. Backscattered electron contrast differences between Si and SiO_2 in the SEM micrographs allowed for accurate determination (within ~20 nm) of the spatial location of the Si-SiO_2 interface for both types of interface. Figures 3.2 and 3.3 show representative low magnification SEM micrographs of the cross-sectional geometry for regions containing the Al metallization and terminated with bare SiO_2, respectively. In each figure, the labels adjacent to the individual scan regions boxes are defined such that

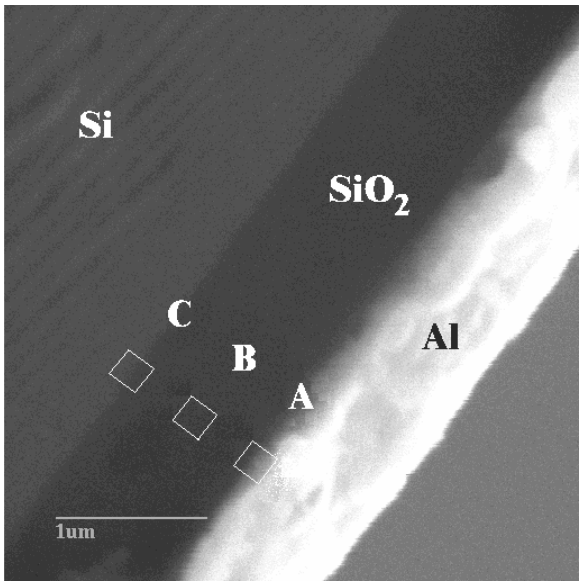

Figure 3.2. Scanning electron micrograph of a cross-sectional specimen in the region with Al evaporated on the SiO_2 film showing the Al metallization, SiO_2 layer, and Si substrate regions. Labels A, B and C represent specific locations within the interfacial and bulk regions representative of where CL spectra were obtained - the Al-SiO_2 interface, the center of the SiO_2 film, and the Si-SiO_2 boundary, respectively. The square boxes illustrate typical scanned areas.

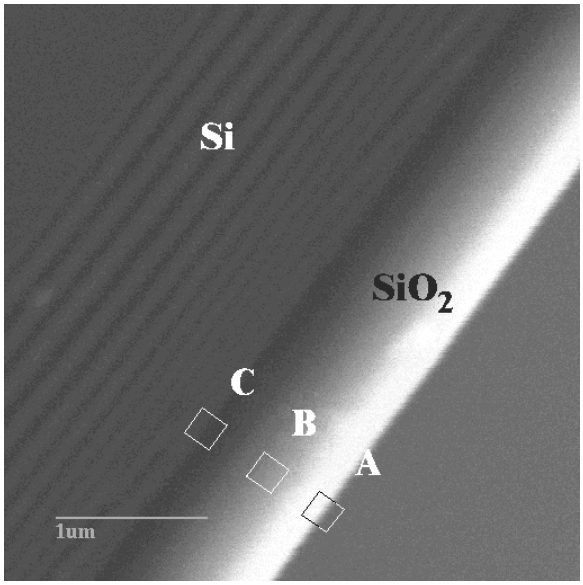

Figure 3.3. Scanning electron micrograph of a cross-sectional specimen in the region without metallization. Labels A, B and C represent the bare SiO_2 interface, the center of the SiO_2 film, and the Si-SiO_2 boundary, respectively. The square boxes show typical scanned areas.

B and C represent the SiO_2 bulk and Si-SiO_2 interface, respectively. Label A represents the Al-SiO_2 interface or the bare SiO_2 surface, as appropriate for the gated and un-gated regions. In the bare SiO_2 region, the boundary between the film and vacuum (i.e. edge of the sample) was also well defined. In the metallized region, the Al-SiO_2 cleaved interface was generally of poor quality, so care was taken to perform analysis in regions that permitted determination of the interface location with similar precision. The square boxes are drawn to scale and with proper orientation for the 200 nm scanning area and represent typical SEM beam positioning.

Figure 3.4(a) shows micro-CLS spectra of the Al-SiO_2-Si regions A, B, and C previously defined for both the irradiated vs. unirradiated (reference) samples. Figure 3.4(b) shows the analogous spectra for all un-gated SiO_2/Si regions. In both figures, the spectra from each of the three spatial regions have been arbitrarily normalized to the 1.9 eV emission, due to the possibility of slight deviations in the cross-sectional optical collection efficiency from sample to sample. In general, such deviations are not large since absolute spectral intensities vary by less than a factor of two from specimen to specimen. All spectra in these figures are uncorrected for optical response of our system, which we compensate for by our analysis method, i.e., quantitative comparison of the *relative* changes in emission before vs. after irradiation. CLS measurements in both figures show the presence of three peak features: pronounced emissions at 1.9 eV and 2.7 eV that have been reported previously for SiO_2 ultrathin films on Si as well as a weak emission at 2.2 eV. Each of these features are present in both the metallized and bare regions, and can be associated with specific defects (see below). The reference spectra

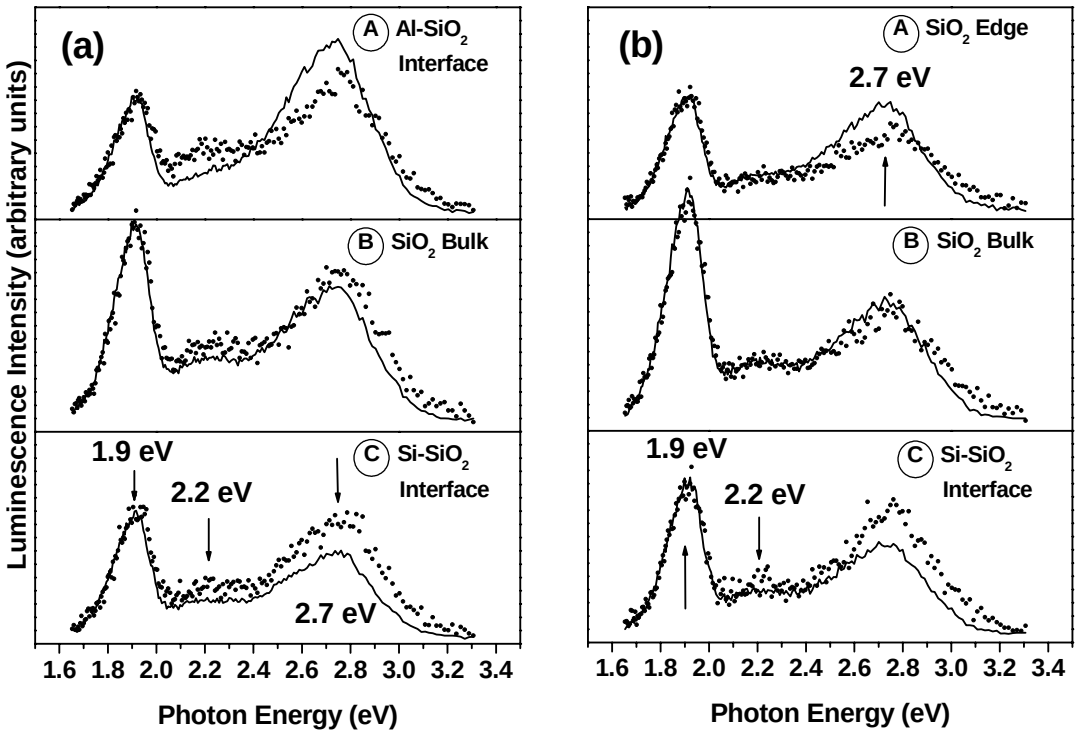

Figure 3.4. Cross-sectional optical spectra for the Al-SiO_2-Si structure, and the bare SiO_2 region at points A, B and C for irradiated (lines) versus reference (square dots) specimens. (Panel (a): Al covered portion; panel (b): bare SiO2 surface.) The irradiated spectra are plotted on the same scale in each frame, and the corresponding reference spectra are arbitrarily normalized to the 1.9eV feature.

(square dots) show a relatively weak 2.2 eV emission in all spatial locations, compared with the 1.9 and 2.7 eV intensities. Within the uncertainty of our measurements, the emission broadness (i.e., full width half-maximum) for the 1.9 and 2.7 eV emissions are unchanged for all conditions of beam positioning and irradiation. For this reason, we consider only peak emission intensity for each feature in subsequent analysis.

Comparison of the micro-CL spectra of the Al-SiO_2-Si regions A, B, and C after 10 keV X-ray irradiation in Figure 3.4(a) shows that the 2.7 eV defect peak increases with proximity to the Al interface, both relative to the 1.9 eV peak and relative to the analogous spectrum in the unirradiated specimen. At location A, irradiation appears to

increase the 2.7 eV peak and decrease the 2.2 eV feature. At location C, irradiation appears to decrease the 2.7 eV peak and reduce the 2.2 eV feature slightly. At location B, spectra for irradiated and unirradiated samples appear similar.

Comparison of the micro-CL spectra of the bare SiO_2-Si regions A, B, and C after 10 keV X-ray irradiation in Figure 3.4(b) shows analogous behavior. At location A, irradiation appears to increase the 2.7 eV peak. At location C, irradiation appears to decrease the 2.7 eV peak. At location B, no spectral changes are evident between irradiated versus unirradiated samples. Furthermore, there appear to be no significant changes in 2.2 eV features as a function of location or irradiation.

Comparison of the micro-CL spectra between the Al-SiO_2-Si and bare SiO_2-Si regions also show significant differences. At point A, the 2.7 eV peak for specimens both with and without irradiation is markedly enhanced for the metallized relative to the bare SiO_2-Si region. There appears to be no similar enhancement at points B or C between the metallized versus bare SiO_2-Si structures. Overall, the 1.9 eV and 2.2 eV peaks are comparable for both the metallized and bare regions for each sample at each point (A, B and C), and are of the strongest intensity in the middle of the SiO_2 film (points B in each figure).

Figure 3.5 illustrates the relative changes in peak intensities as a function of position for the spectra given in Figure 3.4. Even though variations in optical collection efficiency are small, we discuss only relative emission changes in order to eliminate any effect of such changes on our analysis. Figure 3.5 shows the ratio R(2.7 eV/1.9 eV) of the 2.7 eV to 1.9 eV signal strengths for the Al metallized region of the reference and irradiated specimens at the three different regions probed. As before, the dotted line

illustrates the reference while the solid line denotes the irradiated sample. At the Al-SiO_2 interface (position A), R(2.7 eV/1.9 eV) is 28% higher in the irradiated specimen than in the reference specimen. Both ratios remain higher than in the SiO_2 layer or at the SiO_2-Si interface, especially after irradiation. At position C, the irradiated specimen exhibits a 25% lower R(2.7 eV/1.9 eV) compared with the reference specimen.

Figure 3.6 reflects similar behavior for the bare SiO_2 region with and without irradiation. Changes occur similar to those in Figure 3.5 at regions A and C, with R(2.7 eV/1.9 eV) 40% higher for the irradiated versus unirradiated specimen at the vacuum-SiO_2 boundary. Similarly, R(2.7 eV/1.9 eV) is 30% lower at the Si-SiO_2 interface (region C). The close correspondence of the 1.9 and 2.2 eV features for the bare SiO_2/Si specimen between reference and irradiated peaks suggests that normalization to the 1.9 eV peak is appropriate and that the changes in R(2.7 eV/1.9 eV) are due primarily to changes in the 2.7 eV peak. An alternative normalization to the 2.2 eV shoulder has no effect on the ratios in Figures 3.5 and 3.6, nor the apparent changes in the 2.7 eV peak in Figure 3.4(b) versus location in the oxide. However, Figure 3.4(a) shows significant changes in the 2.2 eV feature vs. the 1.9 eV peak near the metal interface (A) of the Al/SiO_2/Si specimen. At this location, R(2.2 eV/1.9 eV) decreases by nearly 40% with irradiation compared to ~10% for locations B and C. Nevertheless, normalization to the 2.2 eV shoulder would serve to further emphasize the increase in the 2.7 eV peak near the metal interface, while preserving its (smaller) decrease at the Si/SiO_2 interface. Hence,

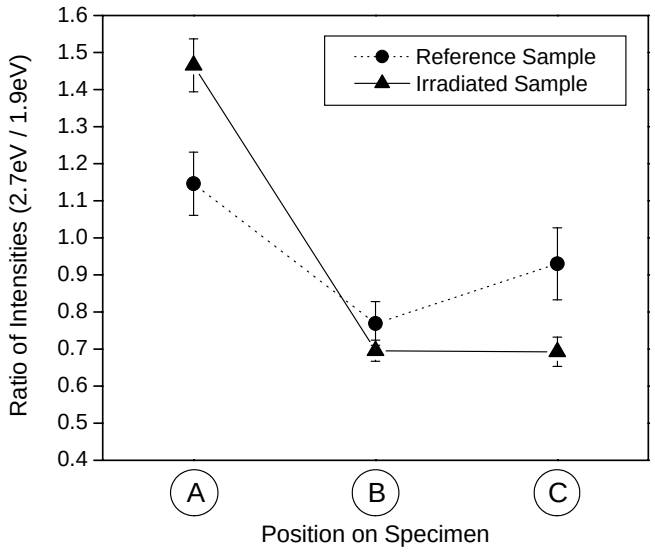

Figure 3.5. The ratio of the intensities of the 2.7eV feature to that of the 1.9eV feature for both the reference (dots) and irradiated (lines) cross-sectional samples at points A, B and C for the Al metallized region of the sample. R(2.7/1.9) is 28% higher for the irradiated sample than in the reference sample for the Al-SiO_2 interface (region A). At the Si-SiO_2 interface (C), R(2.7/1.9) of the irradiated specimen exhibits a 25% lower intensity ratio compared with the reference sample.

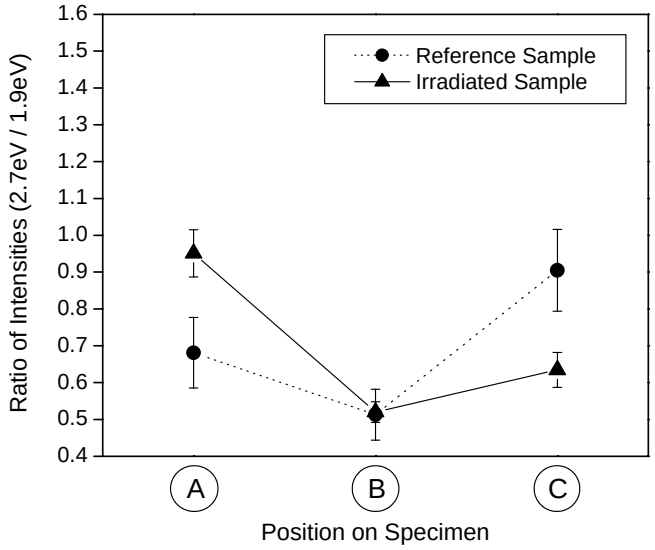

Figure 3.6. The ratio of the intensities of the 2.7eV feature to that of the 1.9eV feature for both the reference (dots) and irradiated (lines) cross-sectional samples at points A, B and C for the unmetallized region of the specimen. R(2.7/1.9) is 40% higher for the irradiated sample than in the reference sample for the vacuum-SiO_2 interface (region A). At the Si-SiO_2 interface (C), R(2.7/1.9) of the irradiated specimen exhibits a 30% lower intensity ratio compared with the reference sample. The graph is plotted on the same vertical scale as Figure 3.5.

either normalization indicates substantial variations in the 2.7 eV peak with location within the oxide.

Lateral intensity variations of the spectral features reveal that all emissions originated exclusively from the SiO_2 film. A CASINO[49] Monte Carlo simulation (described in Chapter 2) showed a characteristic (i.e., 1/e attenuation) excitation radius for backscattered electrons of ~ 0.7 μm for the 10 keV beam in Si. Indeed, fitting the exponential decay of the observed spectral intensities of trap emission into the Si, starting from the SiO_2/Si interface (not shown), yields a value of 0.6 μm. Furthermore, if the beam is positioned in the Si sufficiently far from the SiO_2 (>1.2 μm), no emission is detected. This behavior shows that all luminescence originates from the oxide or its interfaces. A similar electron beam characteristic radius is predicted by CASINO for the SiO_2 film, implying a large percentage of the beam is contained at the center of the film when positioned at location B. The large changes in R(2.7 eV/1.9 eV) at the two SiO_2 interfaces indicate the beam radius is in agreement with the simulation. Otherwise, such changes in R(2.7 eV/1.9 eV) would not be observable, as they would be averaged out.

In order to verify that the SEM electron beam was not inducing changes that could alter the results, time-dependent effects were monitored during the length of individual scans. For these measurements, the electron beam was positioned at a previously unanalyzed spot with beam current and raster size identical to those employed in all previous scans. Emissions were collected in monochromatic mode for each of the three defects previously identified (1.9, 2.2, and 2.7 eV) for the normal length of an individual spectrum (~ 300 s). Within the $\pm$5% noise level of the spectra, the 2.2 eV emission was unaffected by the electron beam in this time interval. The 1.9 and 2.7 eV

emissions each increased linearly over the 300 s time period, with a final increased intensity of <15%, compared with the initial values. This behavior was observed for both reference and irradiated cross-sectional samples. Previous SEM studies of electron beam effects in quartz with higher current densities project comparable or smaller effects under our conditions.[35] It is important to note that during spectral acquisition (e.g. Figure 3.4), 300 s represents the total length of the scan, at which point all defect intensities have already been measured. For example, the 2.7 and 1.9 eV emission intensities are recorded at ~100 s and ~200 s, respectively, from the beginning of the scan. Given the linear increase in emission, the adjusted electron beam effects for both emissions are <10%. This percentage change is 2.5 times smaller than any of the changes in R(2.7/1.9) discussed above. Note that such electron beam effects should appear systematically for each and every spectrum so that the net effect on relative R(2.7/1.9) is much smaller than 10%. Also, the changes in R(2.7/1.9) reproducibly exhibit both increases and decreases at the different interfaces, which would be difficult to explain by the electron beam effects we observe. We therefore conclude that electron beam effects produce relatively small or negligible effects on R(2.7/1.9) versus position plots shown in Figures 3.5 and 3.6.

3.4 Analysis of cathodoluminescence data

The CLS data presented in Figure 3.4 show that two defect emissions at 1.9 and 2.7 eV dominate the optical spectra from thick Al gate oxide structures. Additional emission at ~ 2.2 eV is present with much lower intensity. CLS measurements have reported the 2.7 eV feature previously in crystalline SiO_2, amorphous SiO_2, SiO_x, and SiO_x at thermally-grown SiO_2-Si interfaces.[33,44,45,50,51,52] Based on electron spin resonance studies, this 2.7 eV emission is generally associated with E' centers, namely positively charged O vacancies[36,37,53,54] and more specifically with its precursor, the electrically-neutral, unrelaxed, oxygen-deficient center termed ODCII.[55] The E' center is considered the most important trap center in silicon oxides and has been modeled as an unpaired electron localized on a Si atom back-bonded to three O atoms, denoted ≡ Si •, where ≡ denotes the three bonds and • represents an unpaired spin.[36,38] The ODCII precursor involves oxygen vacancies neighbored by two Si atoms (≡ Si . . Si≡). Its PL intensity correlates with the concentration of EPR-detected E' centers.[55]

The 1.9 eV feature has been also been previously reported in crystalline and amorphous SiO_2 by CLS.[35,36,47,56,57] Broad structure at 1.9–2.0 eV has been attributed to a-SiO_x bonding environments, interface microstructure, or associated point defects associated with the otherwise crystalline Si at the Si/SiO_2 interface. Well-defined CL and photoluminescence (PL) peaks at 1.9 eV are attributed to non-bridging O hole centers[52,57] (NBOHC), the leading interpretation for this feature.[35,36,37] The structure of the NBOHC has been inferred from ^{17}O ESR hyperfine structure and is denoted by ≡ Si-O• •Si ≡.[36,58] It can result from the fission of a strained Si-O-Si bond.

The 2.2 eV feature has also been reported in CL spectra previously.[35,59] It is more prominent in dry-grown versus chemical vapor deposited oxides and is related to the structure of SiO_2 thin films. PL and absorption studies show a 2.1 eV peak with characteristics of a self-trapped exciton.[60] CL studies of quartz using an SEM at 30 keV, 0.25 μA, and 0.6 μm beam diameter exhibit spectra similar to those in Figure 3.4, with a small 2.28 eV feature dominated by 1.9 and 2.7 eV peaks.

There have been numerous studies of defects induced by radiation in various forms of SiO_2. These include observations of 1.9 eV PL induced by X-ray irradiation in silica optical fibers,[61] X-ray induced PL at 1.9 eV in a-SiO_2, 2.7 eV PL and 1.9 eV absorption induced by C^{60} X-ray irradiation in thin film silica[62] and silica fibers[63], respectively.

By inspection of these figures, R(2.7 eV/1.9 eV) is unaffected by irradiation in the SiO_2 bulk region (position B). At position A, R(2.7 eV/1.9 eV) increases by 28% and 40% in the metallized and bare SiO_2 regions, respectively. At the Si-SiO_2 interface (position C) the opposite effect is observed, i.e., the ratio decreases upon irradiation by 25% and 30% in the metallized and bare regions, respectively. This analysis suggests that the effect of radiation in the SiO_2 film is to produce a gradient of change in the ratio of intensities for the 2.7 eV feature compared with the 1.9 eV feature. This gradient effect is present in both the metallized and bare SiO_2 regions.

The higher R(2.7eV/1.9eV) value before irradiation at the crystalline-Si/SiO_2 interface versus the SiO_2 bulk in Figures 3.5 and 3.6 may be due to O outdiffusion at the interface and resultant O vacancy formation in the SiO_2.[64] This is consistent with an asymmetry in the density of hole traps within metal-SiO_2-Si devices reported

previously.[65] The radiation-induced *decrease* in R(2.7eV/1.9eV) trap emission intensity at the crystalline-Si/SiO_2 interface (location C) in both structures is consistent with assignment of this peak to the E' precursor, ODCII, such that the peak intensity decreases as some of the ODCIIs trap radiation-generated holes and become positively charged E' defects.

Similarly, the increase at the Al/SiO_2 interface relative to the SiO_2 bulk may be due to O depletion at the interface with the Al overlayer and formation of O vacancies in the SiO_2. Indeed, quantitative Auger electron spectroscopy (AES) depth profile studies show that the Al-SiO_2 interface contains an interfacial layer due to reduction of the SiO_2 and formation of Al_2O_3.[66] This metal-semiconductor reaction is thermodynamically favorable, even at room temperature.[67] Such reactions are common at metal-semiconductor junctions in general, and their presence correlates with changes in interface charge transfer.[68] Bond breaking due to x-ray irradiation can promote the Al-SiO_2 reaction further and could account for the increase in O vacancy defects and hence the R(2.7eV/1.9eV) increase at location A after irradiation. While such bond breaking might also promote O diffusion from SiO_2 into Si, the thermodynamic driving force to form an Al oxide at the Al-SiO_2 interface is much higher.

The signal-to-noise ratio S/N of the spectra in Figures 3.3 and 3.4 provide an indication of the detection limit of the SEM-based CLS technique in this MOS structure. For count rates of ~ 500 cps, S/N ~25. Assuming that the CLS peaks are proportional to defect densities, the areal charge densities of ~ 4 x10^{11} cm^{-2} measured electrically correspond to a detection limit of ~ 2 x 10^{10} cm^{-2}.

This work demonstrates that cathodoluminescence spectroscopy can detect optical emission from oxide traps within thick film metal-oxide-semiconductor structures. These are the first direct microscopic measurements of radiation-induced electronic traps as a function of position within MOS gate oxides. Irradiation of oxides can produce both increases as well as decreases in relative trap densities measured within the oxide. Specifically, the effect of irradiation is to produce a gradient of change of the ratio ODCII (E' precursor) vs. NBOHC trap emission intensity ratio across the oxide between its Si substrate and a metal film or free surface. These changes are attributed both to x-ray induced free carrier migration and to chemical interactions at the SiO_2 interfaces. These results represent the first step in using CLS to map electronic traps within real device structures on a microscopic scale. In Chapters 3 through 6 and 8, cathodoluminescence is used to correlate degradation in device performance for applied to III-nitride compounds subjected to various radiation and practical surface treatment processes.

CHAPTER 4

PROTON IRRADIATION EFFECTS IN AlGaN-GaN HEMT STRUCTURES

4.1 Introduction to irradiation effects in nitride HEMTs

Much effort has been recently devoted to highly controlled growth of nitride heterostructure devices, consistent doping methods, and the fabrication of temperature- and time-stable ohmic and Schottky electrical contacts. The effects of irradiation on $Al_xGa_{1-x}N$ / GaN Heterojunction Field Effect Transistor (HFET) and Modulation Doped Field-Effect Transistor (MODFET) devices will become increasingly important as these devices are used in space radiation environments. Recent investigators[69,70,71] have studied the effects of proton irradiation on electrical transfer characteristics of the devices, including the decrease in dc saturation current and transconductance as a function of proton energy and fluence. Their results are consistent with the formation of states within the semiconductor band gaps due to the proton-induced displacement of atoms in the multilayer lattice structure creating point defects such as vacancies and interstitials. However, although decreases in free carrier density and increases in trap densities are observed for III-nitrides and other III-V compounds with proton irradiation, relatively little is known about the spatial distribution of such defects, their influence on the internal

electric fields within the AlGaN/GaN structure, and their effect on the resultant band structure.

The correlation of radiation-induced transistor performance degradation with spectroscopic characterization of the device material may yield important clues as to the origins of their radiation damage. Spectroscopic techniques such as photoluminescence (PL)[72], Raman spectroscopy[73], and deep-level transient spectroscopy (DLTS)[74,75,76,77] have been previously used to characterize AlGaN and GaN bulk structures after proton irradiation. Spectroscopy of nitride-based light-emitting diode (LED) structures has also been reported in conjunction with the measurement of electrical characteristics.[78,79] Here, as in the case of the x-ray irradiated SiO_2 layers discussed in Chapter 3, low energy cathodoluminescence spectroscopy is used to probe these structures. The low beam energies employed using cathodoluminescence make this technique additionally well suited for analyzing HFET and MODFET structures, since the total thickness of these structures is typically on the order of tens of nanometers, which is a typical excitation depth for beam energies of a few keV or less. The direct correlation of the spectroscopic data with device electrical characteristics adds physical insight into the changes in material properties that can explain degraded electrical characteristics after proton irradiation.

Additionally, the comparison of different heterostructure growth techniques may indicate a favorable method for fabricating radiation-hardened devices. In addition to studying the electrical and spectroscopic characteristics of metal-organic chemical vapor deposition (MOCVD) grown MODFET structures, spectroscopic data for bulk HFET

structures grown by molecular beam epitaxy (MBE) is included, thereby illustrating that irradiation effects can differ based on the device growth and/or fabrication technique.

4.2 Growth and experimental details

All devices and bulk material characterized in this study were irradiated at room temperature with 1.8 MeV protons at Vanderbilt University using a Van de Graaff accelerator (flux between 1 and 5 x 10^{10} protons $cm^{-2}sec^{-1}$ depending on target fluence). All device terminals were grounded during irradiation. DC electrical characteristics were obtained at room temperature using a HP4156A semiconductor parameter analyzer.

Cathodoluminescence analysis was performed at Ohio State University using the JEOL 7800F ultra-high vacuum (UHV) scanning electron microscope (SEM) described in Chapter 2. For the nitride HEMT structures, the samples were analyzed at low temperature using the Oxford liquid helium cooled sample stage. The depth of electron beam-induced excitation for different beam energies is shown in Figure 4.1, as generated by a CASINO[80] Monte Carlo simulation. For electron beam energies E_B between 0.5 and 4 keV, corresponding peak excitation depth varies between < 5nm and ~ 50 nm.

Two sets of samples were employed in this study. The first set was grown by MOCVD at the University of California—Santa Barbara and consisted of 3.5 μm of unintentionally doped GaN grown on a sapphire substrate, followed by a 2.8 nm undoped $Al_{0.36}Ga_{0.64}N$ spacer, a 16 nm $Al_{0.36}Ga_{0.64}N$ donor layer (~10^{18} cm^{-3} Si doped), and capped by an undoped $Al_{0.36}Ga_{0.64}N$ layer of thickness 3-6 nm. Mesa isolation was performed by reactive ion etching (RIE). Ohmic and Schottky contacts were patterned using photolithography to form the devices on the MODFET structure. The Ohmic

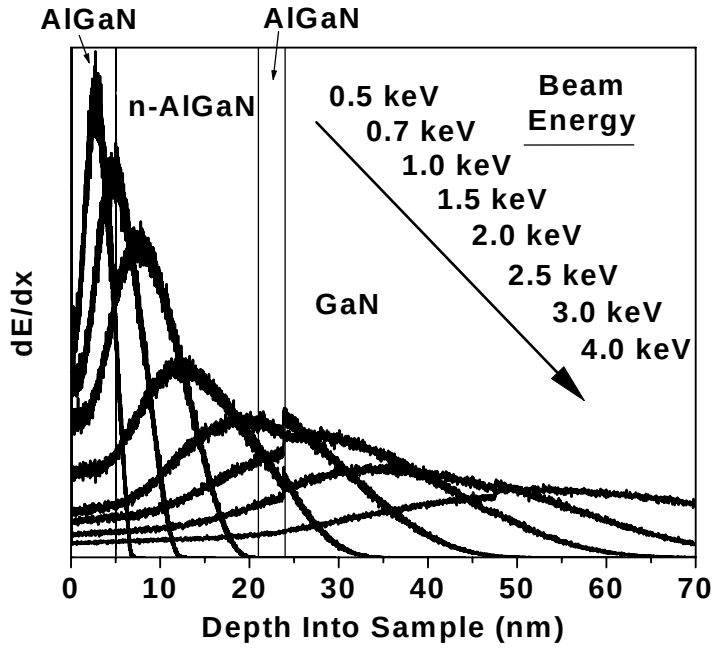

Figure 4.1. Monte-Carlo simulation of energy loss per unit length dE/dx vs. electron beam penetration depth in the MODFET structure for multiple beam energies.

metallization consisted of Ti/Al/Ni/Au (20/200/55/45 nm) and the Schottky contact was Ni/Au (20/350 nm). The gate length for the electrically characterized devices is 0.7 μm. After fabrication, the wafers were cut into individual die and packaged. For each package, two transistors were wire-bonded prior to 1.8 MeV proton irradiation. Source-drain dc I-V characteristics were measured as a function of gate bias immediately prior to irradiation, then at intervals during irradiation. This process was repeated until the devices no longer functioned. The devices were subsequently de-bonded and de-packaged for luminescence analysis, which was performed on a large un-metallized mesa region adjacent to the transistor used for electrical characterization. Multiple spectra were consecutively acquired in the same spot to monitor any possible time effects due to our electron beam. No significant effects were observed.

The second set of samples was from Cornell University and consisted of MBE grown HFET bulk material. (i.e., without mesa isolation and patterned devices). These structures consisted of a 2-3 μm thick GaN layer grown on a sapphire substrate, followed by a 23 nm undoped $Al_{0.34}Ga_{0.66}N$ layer, and terminated with a 2 nm GaN cap layer. Luminescence analysis was performed inside a large square of side ~100 μm, and was checked in several regions to monitor possible spatial luminescence variation in the material. No significant variations were observed, and time effects were also minimal. Transistors fabricated on this material were unavailable at the time of the study, and we include the spectroscopic results for the purpose of comparison to the MOCVD grown material.

4.3 HEMT dc transfer characteristics and spectral evolution vs. proton fluence

Figure 4.2 shows the MODFET source-drain dc current-voltage characteristics before irradiation and after two successive proton fluences of 10^{11} and 10^{12} cm^{-2}. Figure 4.3 shows the transconductance as a function of proton fluence for the same device, with V_{ds} = 7 V. The post-irradiation curves exhibit a reduction in saturation current with increasing proton fluence, compared with the pre-irradiation data. A ~15% reduction in saturation current and a ~10% decrease in transconductance were measured after a proton fluence of 10^{12} cm^{-2}. Cathodoluminescence analysis was performed on a reference (un-irradiated) die and a die with total fluence of 10^{13} cm^{-2}. Both die were taken from the same wafer and exhibited similar electrical characteristics prior to irradiation.

Luminescence spectra of the MODFET were acquired at room temperature in a ~30 μm square mesa region adjacent to the electrically characterized transistor. Spectra

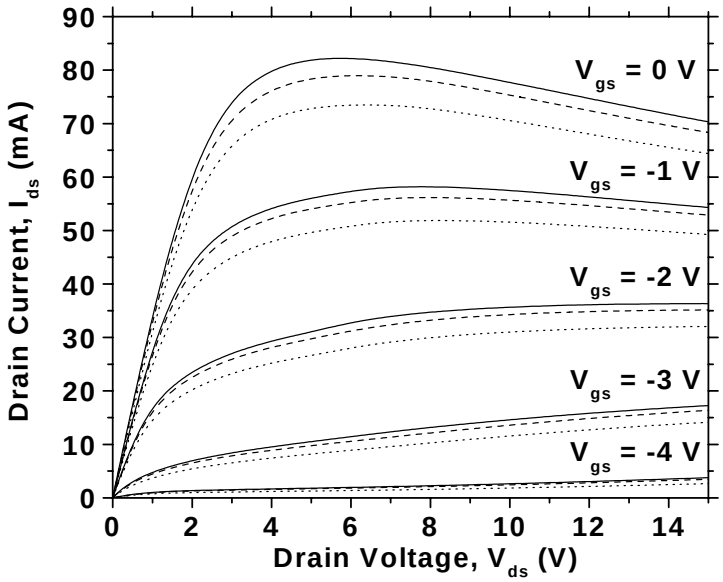

Figure 4.2. Common-source dc I-V characteristics for the same transistor pre-irradiation (solid curves), post 10^{11} cm^{-2} fluence (dashed curves), and post 10^{12} cm^{-2} fluence (dotted curves).

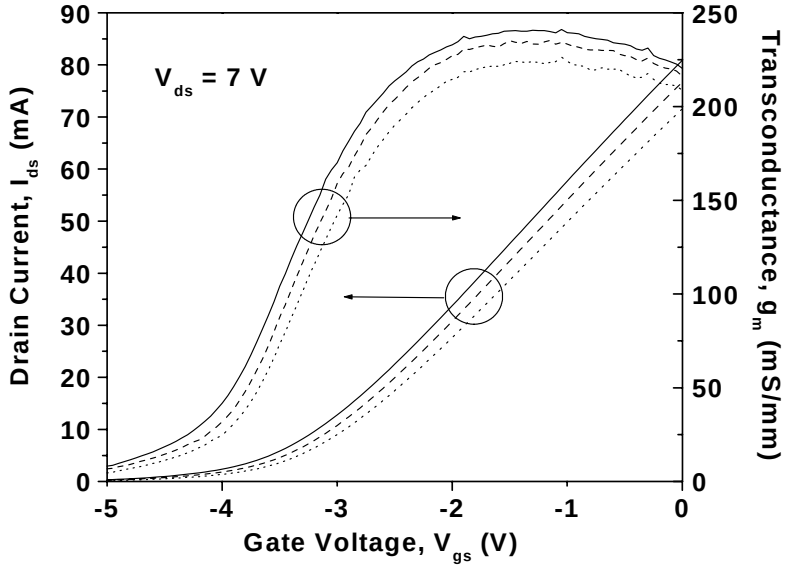

Figure 4.3. Common-source drain current as a function of gate voltage and transconductance of the same transistor pre-irradiation (solid curves), post 10^{12} cm^{-2} fluence (dashed curves), and post $5x10^{12}$ cm^{-2} fluence (dotted curves).

were acquired for beam energies between 0.5 and 4 keV, with the beam current set at 1 nA for 0.5 keV and adjusted for constant power with increasing energies. Figure 4.4 shows a semi-log intensity plot of the spectra for the reference and irradiated die. In this plot, four features are identified: a broad mid-gap "yellow" luminescence from 2.0-2.5 eV, centered at approximately 2.25 eV, the GaN near bandedge (NBE) transition at 3.41 eV, a broad emission at ~3.8 eV and a narrower emission at ~ 4.1 eV due to the AlGaN NBE. The small apparent features at ~1.7 eV and ~2.0 eV are second-order diffraction effects from our grating monochromator related to the 3.4 eV GaN and 4.1 eV AlGaN emissions, respectively. The reference and irradiated spectra for all energies have been arbitrarily normalized to the GaN NBE for relative comparisons of other spectral features. This normalization method is validated by the good agreement of the 4.1 eV emission for all energies in both samples, as well as reasonable agreement in the lower (<3.0 eV) emissions.

The presence of multiple emissions above the GaN NBE has been previously reported in cathodoluminescence studies of AlGaN/GaN HFET structures grown by MBE.[81] Here, the 4.1 eV emission is attributed to the Franz-Keldysh-shifted NBE recombination for the thin, strained AlGaN film, which for unstrained thick films with 36% Al mole fraction is observed at 4.24 eV.[82] This feature taken together with the 3.8 eV emission may represent two different Franz-Keldysh energy shifts originating from the two different types of AlGaN layers (i.e., with and without Si doping). This phenomenon is treated in detail in subsequent sections.

After normalization, the prominent difference between the reference and irradiated sample is the significant decrease in the 3.8 eV emission for all electron beam

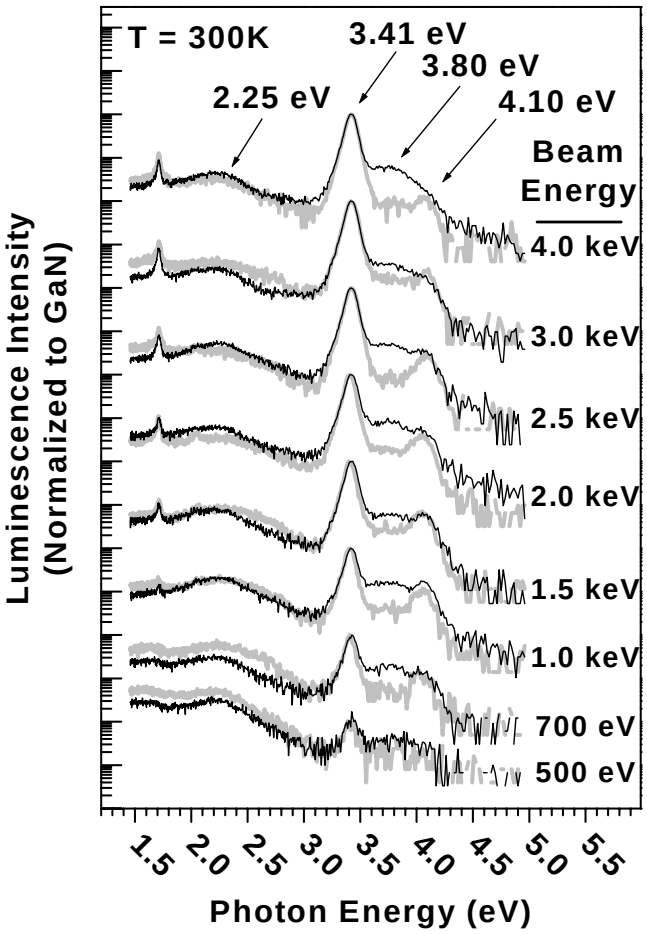

Figure 4.4. LEEN spectra for MOCVD grown MODFET die. A reference die (thin black curves) is compared with a die receiving a fluence of 10^{13} protons/cm^2 (thick gray curves). All intensities are normalized to the GaN NBE emission.

energies. By contrast, the 4.1 eV AlGaN emission is unchanged relative to the GaN NBE in all cases. As the sample temperature is decreased to ~10 K, the GaN and AlGaN NBE transitions exhibit increased intensity and narrower lineshapes, as commonly observed for excitonic luminescence features at low temperature. The 3.8 eV feature does not change in intensity on an absolute scale as temperature is decreased. The lineshape of the

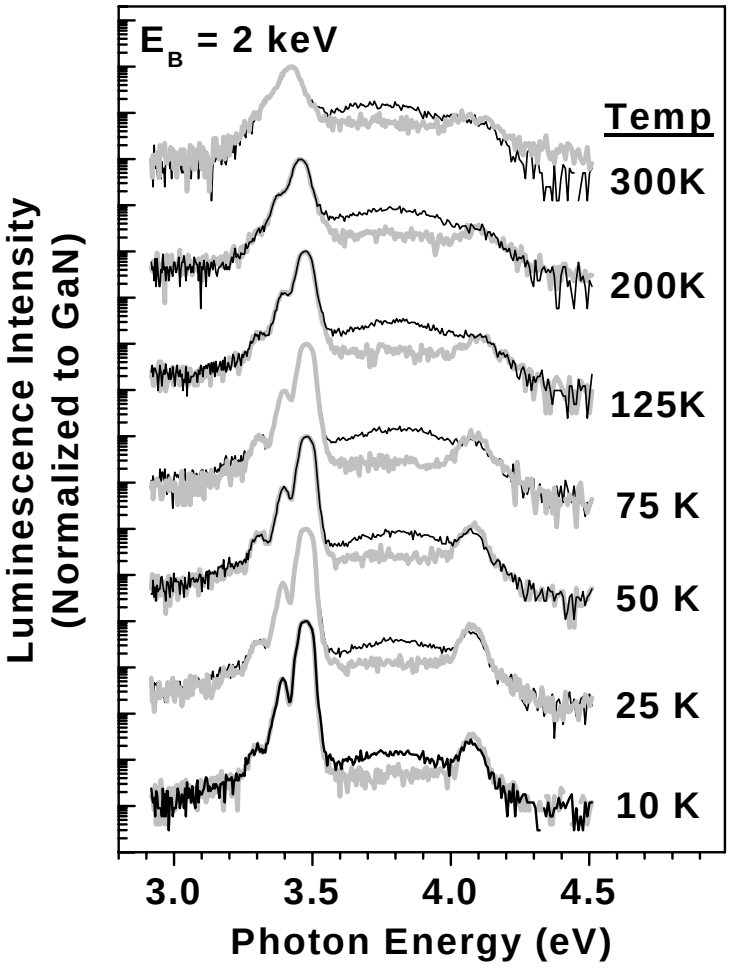

Figure 4.5. Temperature dependence of the LEEN MODFET spectra for the reference (thin black curves) and 10^{13} protons/cm^2 fluence (thick gray curves) die. All intensities are normalized to the GaN NBE emission.

3.8 eV emission is also unaffected by low temperatures, as shown in Figure 4.5. In this figure, all data were obtained with a beam voltage of 2 keV and the spectra have again been normalized to the GaN NBE emission. Sub-GaN NBE emissions are increasingly resolved as temperature is decreased, and have been previously attributed to phonon replica emissions associated with the various GaN excitons.[83] No significant temperature evolution was observed for the small yellow luminescence.

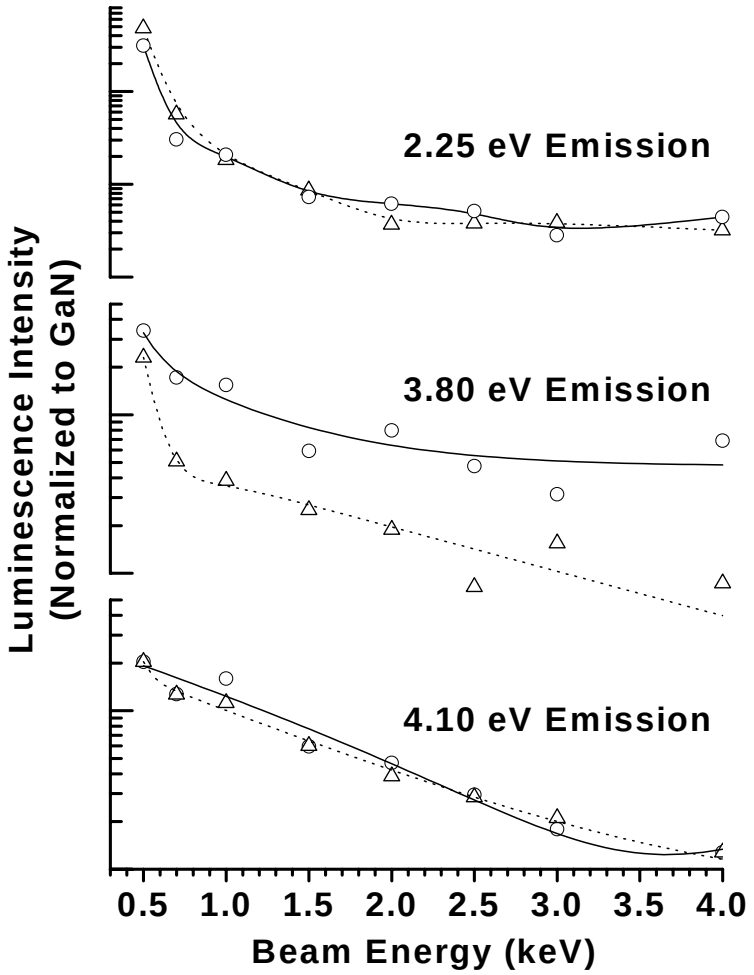

Figure 4.6. Intensities and least-squares fits of the 2.25 eV, 3.8 eV, and 4.1 eV emissions as a function of electron beam energy for the MODFET reference die (circle symbols, solid curves) and the 10^{13} protons/cm^2 irradiated die (triangle symbols, dotted curves). These intensities are extracted after normalizing to the GaN NBE.

The depth dependence of the ~2.25 eV, 3.8 eV, and 4.1 eV emissions can be extracted from the variations in spectral features with incident beam energy E_B. Figure 4.6 shows the intensities of these emissions as a function of E_B, with the intensities normalized to the GaN NBE, as in Figure 4.4. The 4.1 eV AlGaN emission exhibits an exponential decay with increasing beam energy, consistent with its near-surface location

and the increasing depth of excitation with increasing E_B. For $0.5<E_B<1.5$ keV corresponding to excitation almost entirely within the AlGaN layers (see Figure 4.1), the relative intensity decay of the 3.8 eV emission is ~50% faster than that of the 4.1 eV feature. This difference indicates that the 3.8 eV feature is associated with a layer located closer to the free surface than that of the 4.1 eV feature. For $0.5<E_B<3$ keV, corresponding to overall decay well past the AlGaN/GaN interface, the 3.8 and 4.1 eV features exhibit nearly the same decrease. The 2.2-2.4 eV emission normalized to the GaN NBE intensity also exhibits a decrease with increasing E_B, indicating that this luminescence is primarily in the AlGaN layers, rather than the GaN.

Irradiation also produces significant spectral changes in AlGaN/GaN unpatterned HFET layers grown by MBE. Figure 4.7 shows 10 K LEEN spectra for reference and irradiated bulk samples for the HFET structure. As before, all spectra have been normalized to the GaN NBE emission. The electron beam currents were chosen by the method described for the MODFET die, and the total proton fluence of the irradiated specimen was 10^{13} cm^{-2}. The reference HFET sample exhibits emission at 3.49 and 3.73 eV, corresponding to the GaN and AlGaN NBE emissions, respectively. The peak at 3.42 can be attributed to a characteristic neutral donor-acceptor (D-A) pair recombination. Additionally, the GaN NBE exhibits a broad sub-GaN shoulder from 3.2-3.4 eV combined with a narrow emission at 3.42 eV. The broad emission may represent Franz-Keldysh red-shifted NBE emission from strained GaN at the two-dimensional electron gas (2DEG) AlGaN/GaN interface or in the thin GaN cap layer at the free surface.

The irradiated specimen exhibits significant differences compared with the reference spectra. A 3.19 eV emission appears, and its intensity relative to the GaN NBE

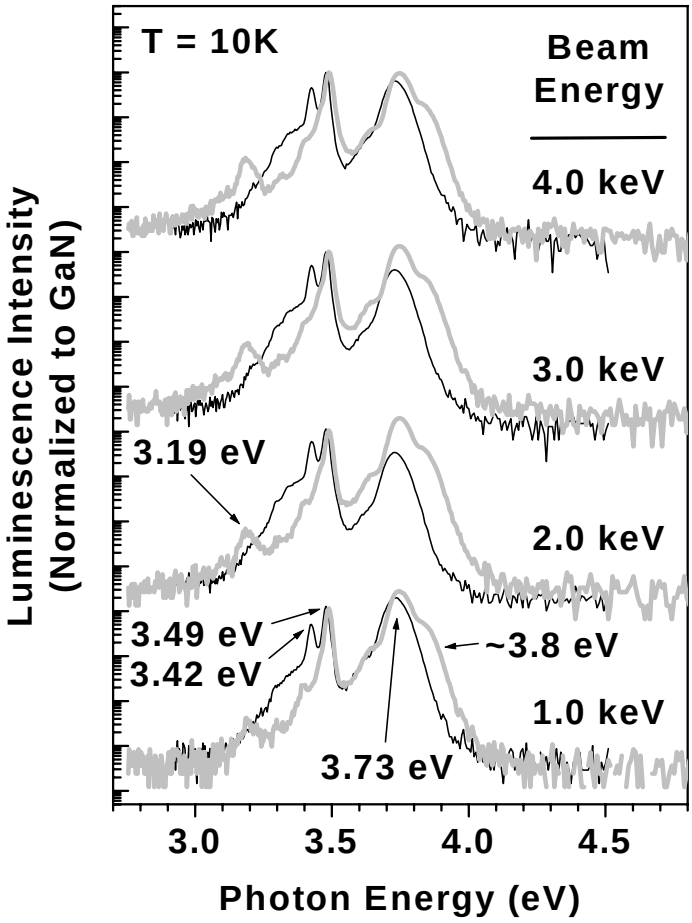

Figure 4.7. 10 K LEEN spectra as a function of electron beam energy E_B for MBE grown HFET samples before irradiation (thin black curves) and after 10^{13} protons/cm^2 fluence (thick gray curves). All intensities are normalized to the GaN NBE emission.

increases with increasing E_B and proximity to the GaN. This implies the emission originates past the AlGaN layer. Emission at ~3.2 eV has previously been reported for bulk GaN films[84] and has been attributed to a D-A pair transition. A significant decrease in the 3.2-3.4 eV shoulder emission is also observed for all beam energies. A final post-irradiation change is the appearance of a higher energy component of the AlGaN NBE emission, with an apparent peak in the vicinity of ~3.8 eV, when corrected for convolution with the 3.73 eV emission.

4.4 Analysis of optical data

From the 300 K spectra of the MOCVD-grown AlGaN/GaN MODFET structures, no significant changes are observed after irradiation in the relative emission intensities for the AlGaN NBE (4.1 eV) and "yellow" luminescence (2.2-2.4 eV), when normalized to the GaN NBE (3.41 eV). Absolute intensities of the GaN NBE (and consequently the AlGaN NBE and "yellow") were also unchanged, within the uncertainty of optical collection efficiency for slightly different sample positioning within our SEM (~10%). Similar GaN NBE intensity comparisons can be made for the MBE-grown HFET structures. These observations indicate the AlGaN and GaN films are not strongly degraded upon 10^{13} cm^{-2} proton irradiation. Similar results have been observed for photoluminescence studies of thick GaN films, for which the luminescence intensity decreased significantly (nearly three orders of magnitude) only after proton fluences in excess of 10^{13} cm^{-2}.

SRIM[85] simulations of 1.8 MeV proton irradiation indicate that ionization events dominate the proton energy loss within the AlGaN/GaN structure, with the non-ionizing energy loss (NIEL) events comprising only a small fraction (2.4 eV/ion vs. 1.24 x 10^5 eV/ion)[86] of the total. Ionizing irradiation does not produce significant degradation of the films, because the resulting electron-hole pairs recombine quickly. NIEL events consist of the generation of lattice phonons and vacancy-interstitial (V-I) pair formation. Even for the low NIEL component of the energy loss, our SRIM simulations indicate the formation of ~10^{16} vacancies/cm^3 in the thin AlGaN layers, based on a displacement damage threshold of 20 eV. Since V-I pairs can easily recombine after formation, this density can be regarded as an upper limit. However, multiple defect complexes can form

that do not readily recombine.[87] Also, GaN damage threshold energies are not well established and lower values produce significantly higher densities. Our SRIM calculations also show the implanted proton concentration resides far from the AlGaN/GaN layers, with a highly concentrated proton penetration depth of ~40 μm.

The predominant irradiation-induced change in the MODFET spectral emission is the significant decrease in 3.8 eV emission. A plausible explanation for this feature is a red shift, i.e., a shift to lower luminescence energy, of the AlGaN NBE emission induced by Franz-Keldysh band gap "narrowing", in turn due to the high piezoelectric field of the strained film.[88] Such piezoelectric fields are induced by lattice mismatch between AlGaN and GaN layers, but smaller fields are also present in ultrathin III-nitride films without strain as well.[89] These fields induce a positive sheet charge at the AlGaN/GaN interface, which in turn induces the 2DEG charge in the MODFET channel. The undoped AlGaN layer is expected to have a high piezoelectric field. A band diagram for this structure, as generated by a one-dimensional Poisson solver program,[90] is shown in Figure 4.8, with piezoelectric parameters taken from.[91] The 2DEG region is shown on the GaN side of the AlGaN/GaN interface, and in this region the conduction band is below the GaN Fermi level. With the additional 10^{18} cm^{-3} Si doped AlGaN layer, the band diagram for this structure exhibits higher electric fields with the outer AlGaN layers (~ $8x10^5$ V/cm) vs. the undoped layer (~ 4 $x10^5$ V/cm) near the AlGaN/GaN interface. Thus it is speculated that the higher energy AlGaN optical emission at 4.1 eV originates in the

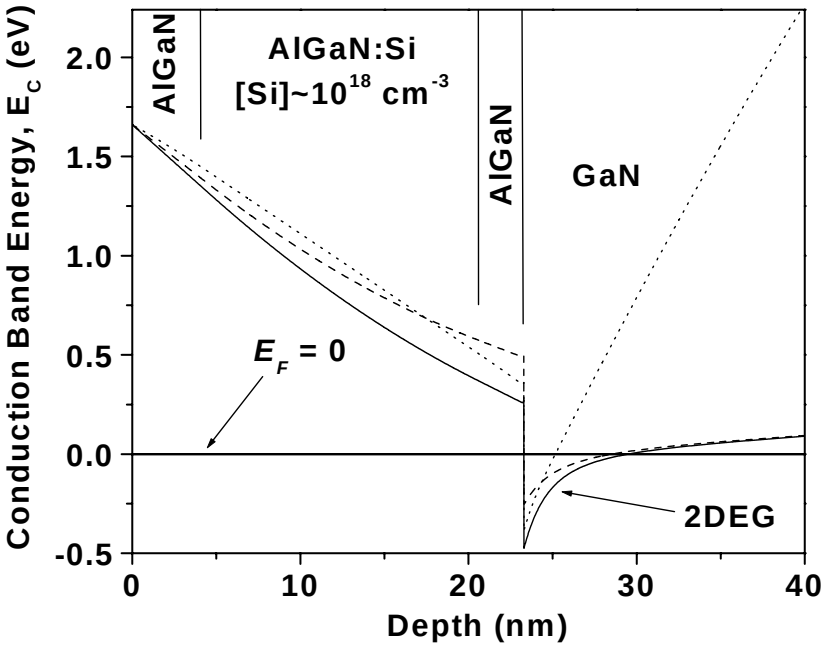

Figure 4.8. Band diagram for the MODFET conduction band, E_C. The Fermi level, E_F, is at 0 eV. The solid curve represents the as-received reference sample. The dashed curve represents the effect of changing the polarization parameters and decreasing the maximum internal electric field from ~0.8 MV/cm to ~0.6 MV/cm. The dotted curve represents the effect of adding 10^{18} cm^{-3} acceptors uniformly throughout all layers. In each case, the effect is to decrease the depth and/or effective width of the 2DEG well, thereby reducing the sheet charge in the FET channel.

undoped portion of the AlGaN film near the AlGaN/GaN interface, whereas the red-shifted 3.8 eV emission originates from the higher electric field strength regions of the outer AlGaN layers.

The cathodoluminescence intensities versus depth shown in Figure 4.6 support this hypothesis. This figure indicates that the 3.8 eV emission originates from shallower in the multilayer structure than the 4.1 eV emission, indicating preferential 3.8 eV emission from the layers nearest to the free surface. The post-irradiation decrease in the 3.8 eV emission can be interpreted as a decrease in electric field within the AlGaN layers.

This decrease could be due to internal electric field screening resulting from charged complexes formed in the AlGaN lattice. Such complexes would need to have areal densities within the AlGaN film comparable to that of the 2DEG channel, e.g., 10^{13} cm^{-2}. New defect complexes can also passivate existing donors[92], thereby reducing carrier concentrations and channel densities. Alternatively, lattice disruption due to such defects may induce sufficient reordering to reduce the as-grown strain and thereby reduce the piezoelectric fields.

The observation that irradiation decreases the electric field is useful in developing physical models for the degradation processes that affect the device electrical characteristics. Figure 4.8 illustrates each effect as calculated by the Poisson solver, by independently reducing the polarization induced sheet charge (and hence the strain in the AlGaN film) or by adding a uniform acceptor concentration of ~10^{18} cm^{-3} throughout the heterostructure. In each case, the effects are to decrease the effective AlGaN electric field and increase the energy of the 2DEG well with respect to the GaN Fermi level. These effects will produce the degradation in MODFET saturation current shown in Figure 4.2 since the sheet charge density in the 2DEG channel would decrease. The decreases in drain current and transconductance shown in Figure 4.3 are also consistent with decreases in 2DEG channel density. Similar effects have been modeled for AlGaN/GaN transistor structures.[93] Using this model, post-irradiation changes in threshold voltage extracted from Figure 4.3 can be accounted for by a 2.5% reduction in polarization sheet charge, if the n-type carrier concentration is held constant. Such polarization charge reduction could be due to strain relaxation or preferential acceptor trapping at the AlGaN interfaces. Alternatively, the threshold voltage shift can be accounted for by decreasing net n-type

carrier concentration by ~ $5x10^{17}$ cm^3. while holding the polarization charge constant. This acceptor concentration is ~10-20 times larger than the maximum post-irradiation vacancy concentration projected from SRIM. However, it is possible that each simple point defect projected by SRIM results in multiple trap complexes that could decrease the donor concentration further.[94] Carrier removal by the formation of defect complexes and/or a reduction in channel mobility will further degrade the device electrical characteristics. However, carrier removal or mobility decreases alone can not account for the spectral differences observed. Additional experiments were designed to track changes in free carrier density, mobility, electrical characteristics, and band bending to distinguish these different mechanisms (see Chapter 5).

Evidence of AlGaN/GaN electric field reduction is also present in the HFET bulk samples. The AlGaN emission observed at 3.73 eV prior to irradiation evolves a higher energy component at ~3.8 eV after irradiation, suggesting a lower electric field and a resultant shift of the AlGaN emission to higher energy. Since only one, undoped AlGaN layer is present in this structure, the AlGaN emission is expected to have only one red-shifted component before irradiation. This is indeed observed as a single 3.73 eV peak. The additional component induced with irradiation can be attributed to reduced fields due to partial screening and/or strain relaxation. The depth dependence of the ~3.8 eV emission in Figure 4.7 indicates increased intensity at intermediate depths (~20-35 nm for 2-3 keV, respectively), corresponding to the AlGaN layer. Since high fields in this layer could separate electron-beam-excited free electron-hole pairs and reduce NBE emission intensity, a reduction in field strength would increase this intensity in the AlGaN as observed.

The narrow peak at 3.19 eV after proton irradiation has been previously observed in GaN films and is commonly attributed to D-A pair transitions. Figure 4.7 shows the intensity of this feature increasing with higher values of E_B, indicating the origin of this feature is in the GaN film, below the channel region. Preliminary analysis of the temperature dependence of the peak intensity (not shown) indicates that it involves a relatively shallow state with low (<25 meV) activation energy. For a nitrogen vacancy V_N, the predominant shallow donor in GaN[95], the corresponding acceptor would then have to be deep (>200 meV), and possibilities include gallium related defects, including V_{Ga}, V_{Ga}+ associated H_n, or V_{Ga} complexed with interstitial N.[96] Gallium vacancy production by high energy protons in, e.g., GaAs, is well known.[97] Overall, the spectral results for irradiated MODFET and MBE-grown AlGaN/GaN structures suggest substantial field reductions due to the creation of charged defects within their AlGaN layers.

Although the predominant spectral changes after irradiation for both sample sets can be attributed to field reduction, it is important to emphasize that these changes are different for each set. For example, unlike the HFET structure, the MODFET structure does not exhibit the evolution of a higher energy counterpart of the primary AlGaN NBE emission. Similarly, the appearance of a D-A pair emission in the HFET specimen is not observed in the MODFET structure. These differences suggest that the effects of proton irradiation are dependent upon the growth method employed. Such growth dependence is not unexpected, given the substantial differences in H and C exposure between the MOCVD and MBE processes. Further study was performed to determine the corresponding electrical degradation of devices fabricated on the MBE material, and

thereby allowing for direct comparison with the MOCVD material. Fluence-dependence experiments for similar MOCVD and MBE samples were also performed, to more precisely correlate the evolution of optical emissions with device electrical characteristics. These results are presented in Chapter 5.

CHAPTER 5

FLUENCE DEPENDENCE OF ELECTRICAL AND LUMINESCENCE PROPERTIES OF PROTON-IRRADIATED AlGaN-GaN HEMTS, TEST STRUCTURES, AND ELECTRICAL CONTACTS

5.1 Introduction

Much variation in proton irradiation-induced AlGaN-GaN HEMT degradation has been reported by several investigators. For device structures sharing similar growth details, including AlGaN thickness and doping, varying degrees of degradation have been reported. Cai et al. originally reported decreases in dc saturation current and transconductance from 260 to 100 mA/mm and from 80 to 26 mS/mm, respectively, for a 1.8 MeV fluence of 10^{14} p^+/cm^2. For a 40 MeV fleunce of $5x10^{10}$ p^+/cm^2, Luo and coworkers reported decreases in the two previous quantities of 20% and 30%. Subsequent work with passivated devices at a 40 MeV fluence of $5x10^9$ p^+/cm^2 resulted in small changes.[98] The work summarized in the previous chapter showed 15% and 10% changes in these respective quantities after a 1.8 MeV fluence of 10^{12} p^+/cm^2.[99] The variance in these sample structures and electrical results indicates the need for continued characterization of irradiation effects on nitride devices.

Recent investigators have also monitored the changes in the transport properties of the two-dimensional electron gas (2DEG) as a function of proton fluence, using a Hall effect measurement procedure, which characterizes the changes in channel transport properties (i.e., mobility and sheet density). Changes to the electrical contacts of the device, which can affect series resistance and the Schottky barrier height of the HEMT gate, are also important for device degradation. Few reports exist addressing the degradation of the HEMT contacts for nitrides.

For this study, the electrical and spectral properties are noted as a function of fluence to identify a critical fluence for degradation of device properties. Also, channel transport properties and electrical contacts are studied in greater detail than in Chapter 4, also as a function of fluence. Additionally, secondary-ion mass spectrometry is used in conjunction with transport data to characterize changes in the AlGaN/GaN channel interface as a function of proton fluence. Lastly, changes to the electrical contact properties are noted as a function of proton energy, as well as fluence.

5.2 Growth and experimental details

A HEMT structure from Cornell University was used for this study. This structure consisted of 2-3 μm of unintentionally doped (UID) GaN grown on a sapphire substrate, followed by ~ 23 nm of $Al_{0.3}Ga_{0.7}N$, and capped by ~ 2 nm of GaN. The AlGaN film was not intentionally doped. The structures were grown by molecular beam epitaxy (MBE), and then mesa isolated by reactive ion etching (RIE). Ohmic (Ti/Al/Ti/Au; 20/120/45/55 nm) and Schottky (Ni/Au; 25/375 nm) contacts were

patterned using photolithography to form the devices on the HEMT structure. Individual die were cut from the wafer and characterized electrically. All electrical measurements were obtained at Ohio State using a manual probe station. Room temperature (RT) Hall measurements, 10 K cathodoluminescence spectra, and secondary-ion mass spectrometry (SIMS) were obtained at Ohio State from larger, unprocessed pieces of the original HEMT material.

All devices and bulk material characterized in this study were irradiated at room temperature with 1.8 MeV protons at Vanderbilt University using a Van de Graaff accelerator (flux between 10^9 and 10^{11} $p^+/cm^2/s$ depending on target fluence). All device terminals were grounded during irradiation. Samples were sent to Ohio State for analysis after irradiation, then returned to Vanderbilt for further irradiation, until the terminal proton fluence. Samples were analyzed at Ohio State within one week of each irradiation session.

5.3 HEMT dc transfer characteristics vs. proton irradiation fluence

Dc drain current vs. drain voltage as a function of gate voltage and proton fluence is shown in Figure 5.1 for a representative transistor with a 75 μm gate width. Within the small uncertainty of our manual probe station measurements, the drain current is unaffected by irradiation for fluences less than 10^{13} p^+/cm^2. Drain current and resulting transconductance vs. gate voltage are shown in Figure 5.2, as measured at a drain voltage of 8 V. Changes in the gate threshold voltage are apparent for all fluences, whereas the extracted peak transconductance is largely unaffected until the fluence exceeds 10^{14} p^+/cm^2.

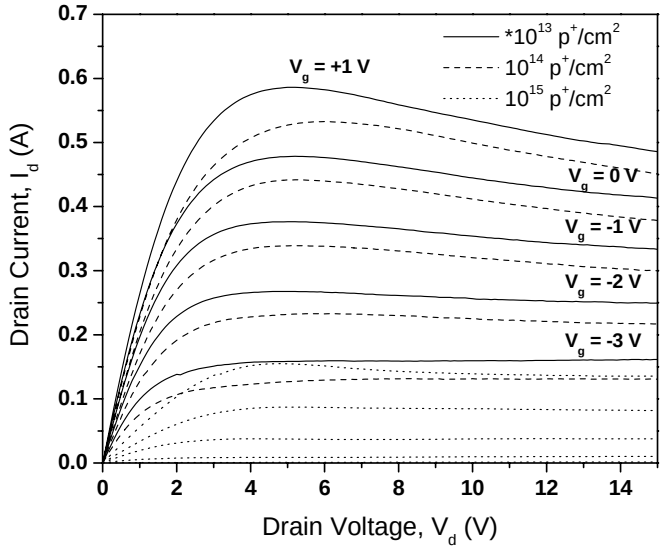

Figure 5.1. Drain current vs. drain voltage for various gate biases, as a function of proton fluence. No significant changes were observed until fluences in excess of 10^{13} p^+/cm^2.

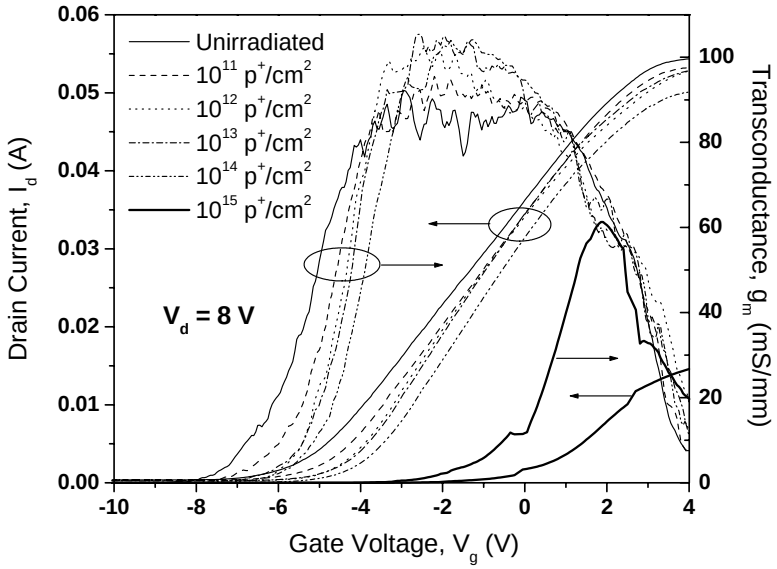

Figure 5.2. Drain current vs. gate voltage and extracted transconductance as a function of proton fluence.

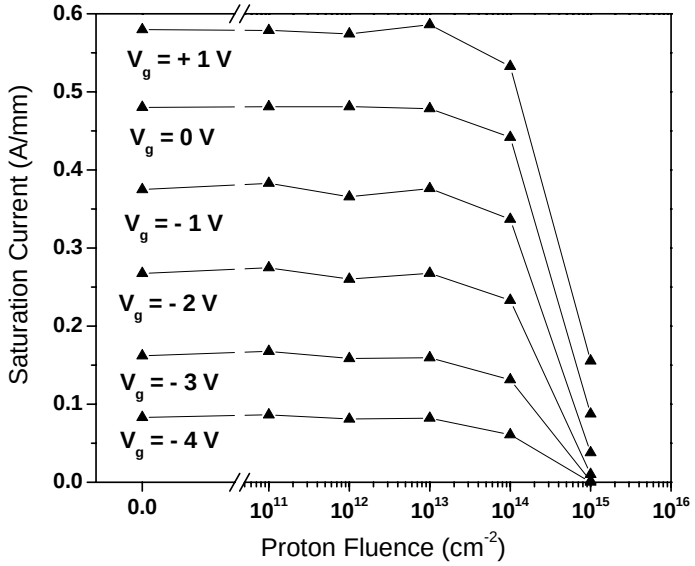

Figure 5.3. Drain saturation current for several gate biases, as a function of proton fluence.

Figure 5.3 shows the peak dc drain saturation current for several gate voltages, as a function of fluence. For gate voltages above the threshold voltage, the saturation current decrease between 10^{13} p^+/cm^2 and 10^{14} p^+/cm^2 is 6-8%. At a cumulative fluence of 10^{15} p^+/cm^2, the saturation current degradation is significant (~ 80% for 0 V gate bias). Figure 5.4 shows the peak transconductance and threshold voltages as a function of fluence. Significant degradation is observed for each quantity for a fluence of 10^{15} p^+/cm^2. For comparison, GaAs-based HEMT structures have been shown to exhibit a 20% decrease in drain current after a 2.0 MeV proton fluence of ~ $3x10^{12}$ p^+/cm^2, which is approximately two decades of fluence lower than comparable degradation extrapolated from our present data.[100]

Figure 5.5 shows the gate current as a function of gate voltage at several fluences for a transistor with 200 μm gate width, with the source and drain contacts grounded. Problems encountered during irradiation did not permit accurate determination of fluence

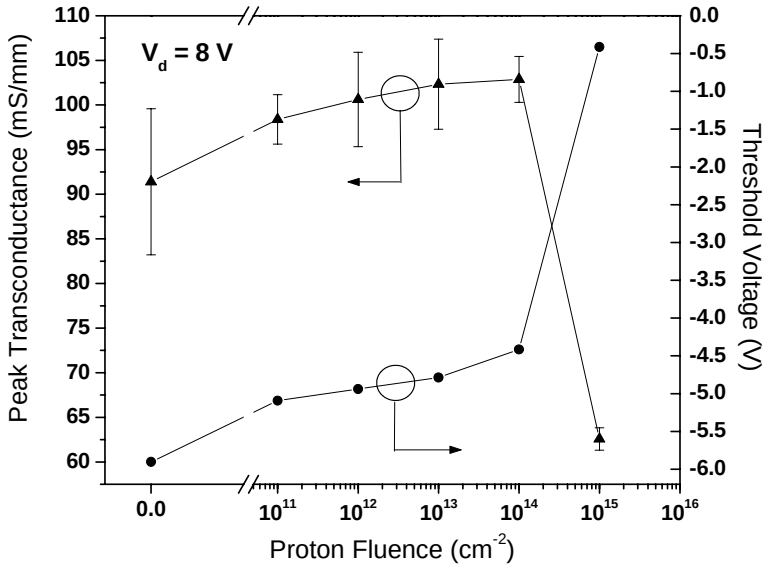

Figure 5.4. Extracted threshold voltage and peak transcondcutance as a function of proton fluence.

prior to $3x10^{12}$ p^+/cm^2, so no data are included for this regime of fluence. Three transistors were tested in this fashion, and the curves shown represent typical behavior with proton fluence. An initial decrease in forward and reverse current is observed between the unirradiated case and a proton fluence of $3x10^{12}$ p^+/cm^2. Subsequent half-decades of fluence show an increase in diode current. The Schottky barrier height of the gate contact vs. proton fluence is extracted from the forward I-V curves assuming thermionic emission for a range of gate voltages between ~ 4 and ~ 12 units of kT. Details of the barrier height extraction procedure may be found in Ref. 101. The resulting values of Schottky barrier height are shown in Figure 5. 6. The initial increase from 0.71 to 0.73 eV and subsequent decrease to 0.69 eV for 10^{14} p^+/cm^2 are reflected in the changes in the I-V curves.

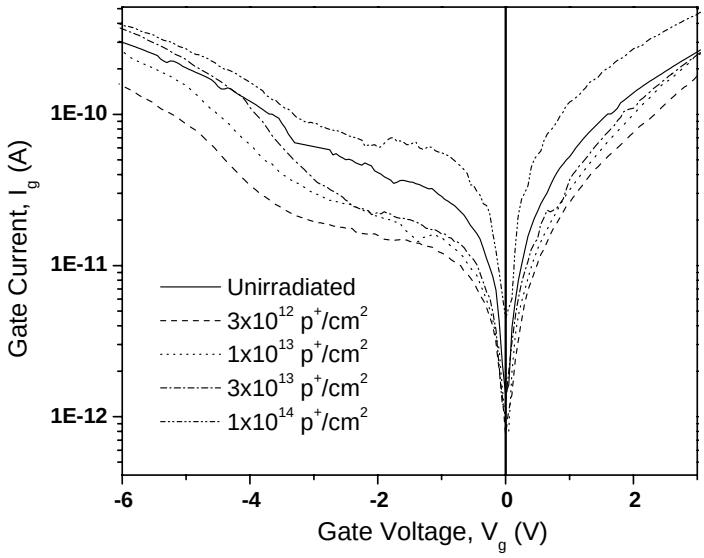

Figure 5.5. Gate current vs. gate voltage for grounded source and drain contacts, as a function of proton fluence.

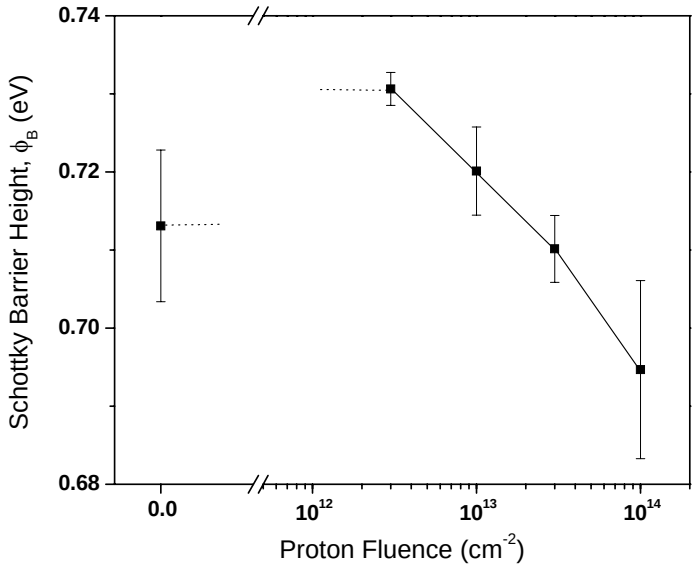

Figure 5.6. Schottky barrier height variation with proton fluence, extracted from the curves in Figure 5.5, assuming thermionic emission from ~ 4 to ~ 12 units of kT in forward bias. The error bars are calculated from the uncertainties in linear fitting parameters, as described in Ref. 101.

5.4 Changes in resistivity and transport properties vs. proton fluence

A transfer length measurement (TLM) test structure was used to extract the specific ohmic contact resistivity and 2DEG channel resistance as a function of proton fluence. The individual gap spacings ranged from 1 to 25 μm, and the TLM structure width was 100 μm. The fluence-dependent TLM results are shown in Figure 5.7. Specific contact resistivity increases slowly by decades of fluence until $>10^{15}$ p^+/cm^2, at which point this value increases significantly. Sheet resistance is unaffected until fluences in excess of 10^{14} p^+/cm^2. From 10^{14} p^+/cm^2 to 10^{15} p^+/cm^2 the sheet resistance approximately doubles, and for additional fluence ($5x10^{15}$ p^+/cm^2) this value degrades considerably. Although the channel is comparatively radiation tolerant (similar AlGaAs/GaAs structures[102] exhibit significant degradation in channel resistance for 0.5 MeV proton fluences greater than ~ $2x10^{12}$ p^+/cm^2), changes in the ohmic contacts are observed for relatively low fluences.

The sheet resistance is inversely proportional to the product of channel mobility and sheet charge density, both of which are extracted from RT Hall measurements. The Hall data shown in Figure 5.8 indicate that for fluences through $2x10^{15}$ p^+/cm^2, the sheet resistance change is due primarily to degradation in mobility, rather than sheet charge density. Similar results in transport behavior have been reported previously for AlGaN-GaN HEMT structures. For the higher fluence of $5x10^{15}$ p^+/cm^2, both mobility and sheet density decrease significantly, which accounts for the large, further degradation in sheet resistance at this fluence.

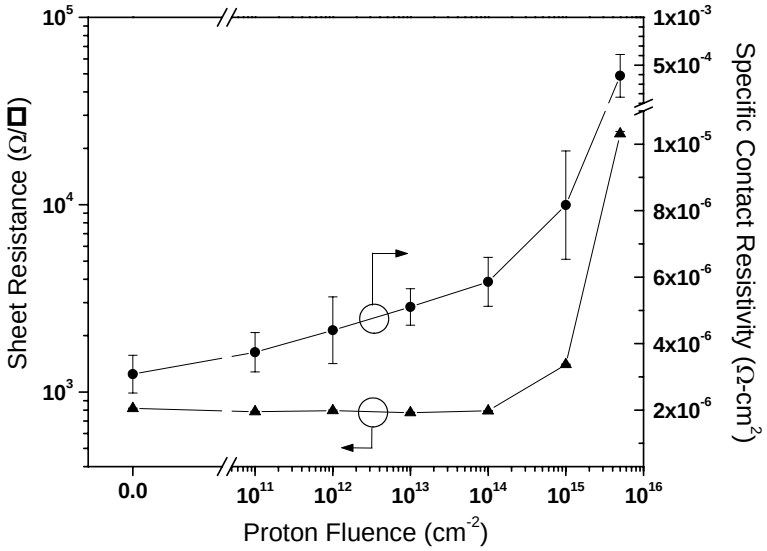

Figure 5.7. Sheet resistance and specific contact resistivity as a function of proton fluence, both extracted from a TLM structure. As in Figure 5.6, the error bars are obtained from the uncertainties in linear fitting parameters.

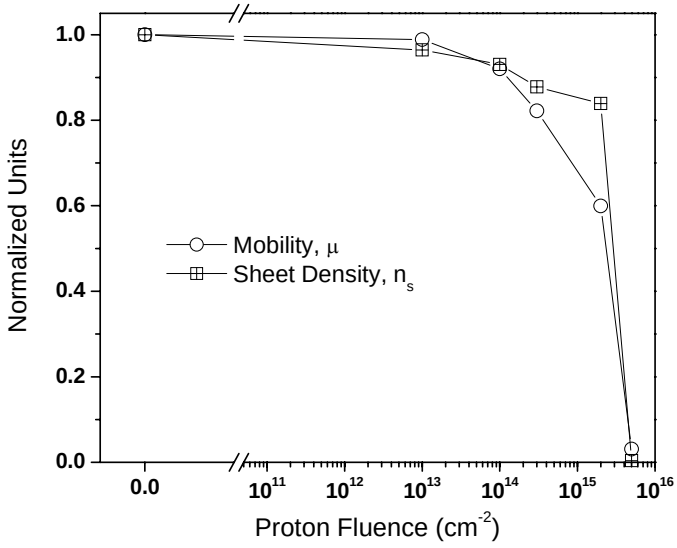

Figure 5.8. Normalized mobility and 2DEG sheet density, extracted from RT Hall effect measurements. The initial 2DEG mobility and sheet density were 987 cm^2/V-s and $1.03x10^{13}$ cm^{-2}.

5.5 Cathodoluminescence study of degradation of HEMT structures

As in the previous chapter, cathodoluminescence (CLS) analysis was performed at Ohio State University using a JEOL 7800F ultra-high vacuum (UHV) scanning electron microscope (SEM) with an Oxford liquid helium cooled sample stage. All CLS spectra were acquired at ~ 10 K. Figures 5.9 and 5.10 show 10 K CL spectra as a function of fluence for a 1 keV and 5 keV electron beam, respectively. CASINO[103] simulations indicate that 1 keV corresponds to a maximum electron beam penetration depth of ~ 20 nm, with the peak of the excitation curve at ~ 8 nm. This implies that recombination luminescence originates from the top-most GaN cap and the AlGaN film. Similarly, the 5 keV beam corresponds to a maximum depth of ~ 200 nm, with the maximum excitation at ~ 80 nm. For this beam energy, the luminescence originates from all regions of the sample, with the majority of electron-hole pairs generated beyond the 2DEG region. Both spectra were taken in decades of fluence, and then at $5x10^{15}$ p^+/cm^2. For the 1 keV beam, there was no significant spectral evolution prior to a fluence of 10^{13} p^+/cm^2, so one curve has been chosen as representative for all spectra through a fluence of 10^{13} p^+/cm^2. In the 5 keV beam case, one curve is chosen for fluences up to and including 10^{14} p^+/cm^2 for the same reason. These onset fluences for spectral changes are in agreement with the sheet resistance degradation shown in Figure 5.7.

In both figures, the two prominent emissions in all spectra are the GaN (3.48 eV) and AlGaN (3.85 eV) near-band edge (NBE) emissions. Due to slight (~ 20%) differences in optical collection efficiency between measurement sessions, we consider relative changes by normalizing all spectra to the GaN NBE. This permits comparison of the GaN NBE lineshape as a function of fluence. For both electron beam energies, the

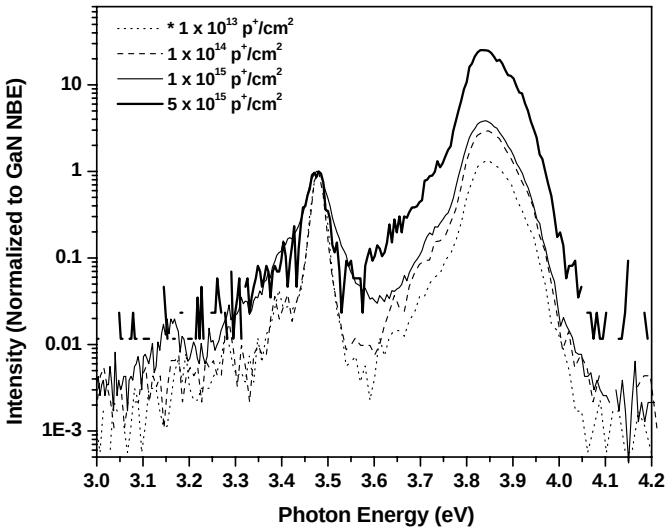

Figure 5.9. 1 keV, 10 K cathodoluminescence data as a function of proton fluence. No significant changes were observed until fluences in excess of 10^{13} p^+/cm^2. A significant effect of irradiation is the broadening of the normalized GaN NBE emission on both the low and high energy sides. This effect can be attributed to degradation mechanisms discussed in the text.

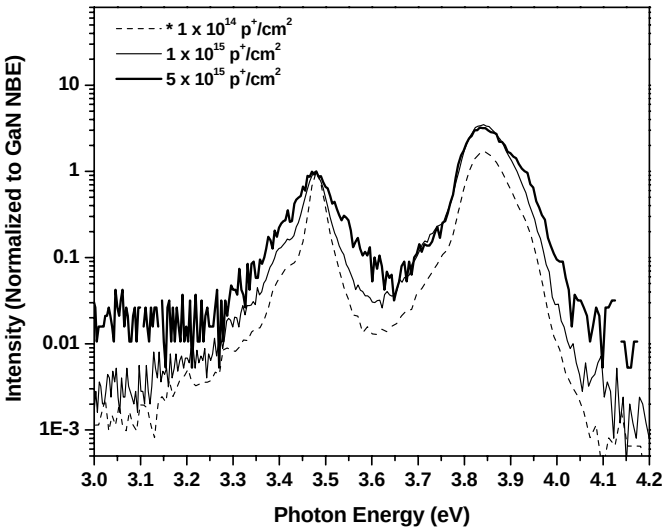

Figure 5.10. 5 keV, 10 K cathodoluminescence data as a function of proton fluence. No significant changes were observed until fluences in excess of 10^{14} p^+/cm^2. In addition to the changes noted in Figure 5.9, the 5 keV curves indicate a higher energy AlGaN component at the highest fluence, which is indicative of partial relaxation of strain in the film.

AlGaN NBE emission increases relative to the GaN NBE, with increasing fluence. This effect is more pronounced in the 1 keV beam case, where the beam is confined to the AlGaN film. Here, any GaN NBE luminescence arises due to carrier diffusion across the AlGaN-GaN interface. Changes in the ratio of GaN to AlGaN indicate the minority carrier diffusion length is decreasing as traps are generated in the AlGaN film or near the 2DEG interface. In the 5 keV case, the electron beam excites all regions of the device structure, and a slightly decreased ratio of GaN to AlGaN NBE emissions may indicate preferential radiation-induced trap formation in the GaN. Indeed, Stopping and Range of Ions in Matter (SRIM)[104] simulations reveal that for the 5 keV beam, the vacancy production density within the GaN analysis depth is ~ 40% higher than in the AlGaN film.

The low fluence spectra in both figures exhibit a small sub-GaN NBE emission centered approximately at 3.43 eV. The intensity of this emission increases with a proton fluence of 10^{15} p^+/cm^2, with respect to the GaN NBE. There is also evidence of NBE broadening in energies above the GaN NBE energy for both beam energies. Each of these broadening effects is more prominent for a fluence of $5x10^{15}$ p^+/cm^2. For the 5 keV, $5x10^{15}$ p^+/cm^2 case the AlGaN NBE exhibits a small, higher energy component to the main AlGaN emission. Additionally, the 1 keV beam case shows an emission at ~3.15 eV after a fluence of 10^{15} p^+/cm^2. Small (~10^3 less than GaN NBE) levels of the commonly reported yellow luminescence (YL) were observed at ~ 2.25 eV, but this emission did not change significantly for our analysis depths. No other emissions were observed to our low energy detection limit of 0.8 eV.

The GaN NBE spectral evolution is consistent with the formation of additional defect complexes near the 2DEG channel. The increased low energy component of the NBE emission indicates the formation of donor complexes, as there is no known shallow acceptor in GaN. Such emissions have been previously observed in luminescence studies, and have been attributed to donor-bound excitonic luminescence. The evolution of a GaN component for energies in *excess* of the NBE can indicate compositional intermixing, i.e., the incorporation of Al atoms into the GaN lattice, which forms an alloy of intermediate aluminum composition. To first order, our spectra indicate a maximum aluminum incorporation of a few percent, by interpolating between the GaN and AlGaN NBE emission energies.

Each of the mechanisms corresponding to the GaN NBE broadening contribute to the measured 2DEG mobility degradation, by impurity scattering and disordered AlGaN-GaN interface scattering. Additionally, the evolution of a higher energy component of the AlGaN NBE at $5x10^{15}$ p^{+}/cm^{2} (see Figure 5.10) suggests a degradation in the piezoelectric properties of the interface, through a decrease of the Franz-Keldysh "red shift" of the emission energy, as the internal electric field in the AlGaN decreases. Any degradation of this property of the AlGaN film will contribute to the decrease in sheet charge density. Finally, the emission at ~3.15 eV in the 1 keV case indicates a donor-acceptor pair in the GaN.[105] Since this emission is not present in the 5 keV data, we believe this emission originates from the thin GaN capping layer, to which the ohmic and Schottky contacts are formed, and possibly the GaN nearest the channel interface. The existence of acceptors near the metal contacts in the first case would lead to donor

compensation or interface trapping effects, thereby degrading the electrical contacts, as previously discussed.

5.6 Secondary Ion Mass Spectrometry of HEMT interface chemistry vs. proton fluence

To confirm the hypothesis of channel interface disorder after proton irradiation, we performed depth-profiling analysis as a function of fluence using a Physical Electronics TRIFT-III time-of-flight SIMS. Details of the SIMS technique can be found in Ref. 103. For this study a oxygen beam was used for sputtering (rate ~ 1 nm per 10 s) and an isotopically pure gallium-69 beam was used for elemental analysis. For the SIMS experiments a larger (1 cm x 0.5 cm) bulk sample was used. The sample was divided into three irradiation regions by using thick metal foil as an irradiation mask. The three regions were chosen based on the measured mobility degradation shown in Figure 5.8, and were defined as unirradiated, $1x10^{14}$ p^{+}/cm^{2}, and $1x10^{15}$ p^{+}/cm^{2}. The sample was verified to exhibit uniformity in all regions prior to irradiation by cathodoluminscence studies. Atomic force microscopy (AFM) analysis of surface roughness on the same scale as the Ga analysis beam size (~ 25 μm square) indicate a uniform root-mean-square surface roughness of ~ 6 nm.

Depth profiles of the Al and ^{71}Ga isotope are shown in Figure 5.11. Both curves have been divided by total ion yield (i.e., sum of all collected ions) to account for systematic changes in ion collection efficiency or sputter yield vs. depth. The two sets of curves have been further normalized to a middle-of-film ion yield for both GaN and AlGaN, to make comparison easier. The variation of yield near the surface (low number of sputtering cycles) is a result of commonly observed SIMS surface effects. Each

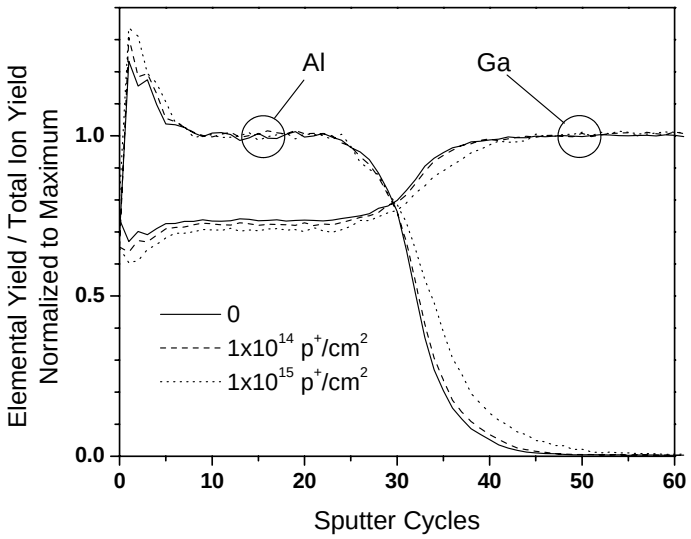

Figure 5.11. Al and Ga SIMS depth profiles as a function of proton fluence. Both elemental profiles indicate a broadened interface after irradiation.

sputter-analysis cycle corresponds to approximately 1 nm into the sample (total depth to channel ~ 25 nm). The discrepancy between the unirradiated depth profiles and the premise of an abrupt interface can arise from μm-scale variation in the "flatness" of the GaN base layer, coupled with sputter-induced interface broadening. Each of these effects will be present for each analysis region of the sample, and a maximum estimate of interface intermixing can be determined based on changes in the extracted interface widths.

The depth profiles shown in Figure 5.11 indicate a broadening in both elemental profiles with increasing proton fluence. We determine the interface width by subtracting the 90% point of the Al profile from the 10% point, then dividing this quantity by the 90% point. In doing so, we have normalized the sputter cycle axis to account for small (<5%) changes in sputtering rate between each scan. This ratio also makes the interface broadness comparable to the initial film thickness. This ratio is shown for four sets of

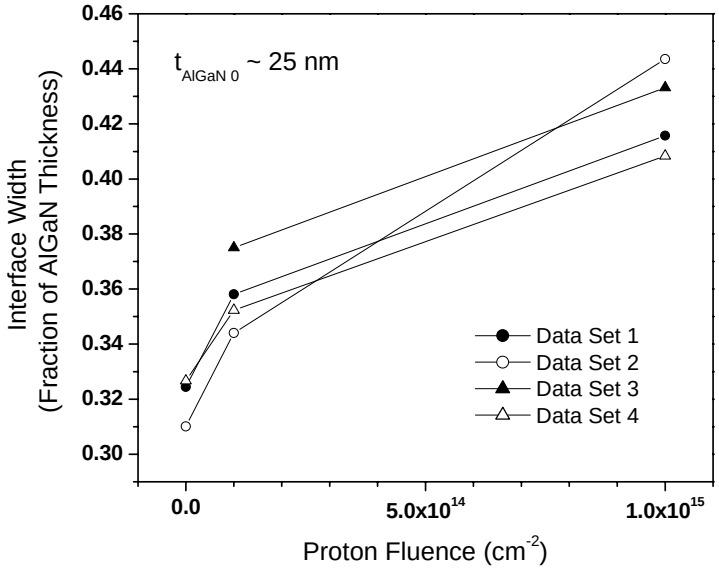

Figure 5.12. Interface widths, extracted from a (90%-10%) / 90% analysis of the Al profile, in units of initial AlGaN thickness, for four data sets as a function of proton fluence. A maximum estimate for interface broadening is 2.5 nm at 10^{15} p^+/cm^2 (see text).

SIMS depth profiles in Figure 5.12 vs. proton irradiation. Post-SIMS inspection of the sample indicated that the analysis area for the $1x10^{14}$ p^+/cm^2 region was closer to the $1x10^{15}$ p^+/cm^2 region than had been targeted. We suspect the metal film masking procedure may produce a non-abrupt transition region between adjacent irradiation regions, and this effect may explain the non-linear behavior of the of $1x10^{14}$ p^+/cm^2 data points. We include, but do not analyze, the $1x10^{14}$ p^+/cm^2 data points to show that they are bounded by the unirradiated and $1x10^{15}$ p^+/cm^2 cases. The unirradiated and $1x10^{15}$ p^+/cm^2 SIMS data points were taken far from the irradiation boundaries, and should not exhibit problems associated with a fluence transition region. Further experiments will show if the interface broadening is linear with proton fluence.

From Figure 5.12, the interface width (including effects discussed previously) in the unirradiated region is determined to be ~ 32% of the initial film thickness (25 nm

total), for an effective width of ~ 8.0 nm. For the $1x10^{15}$ p^+/cm^2 region, the relative width is ~ 42%, which corresponds to a width of ~10.5 nm. We conclude that the effect of a proton fluence of $1x10^{15}$ p^+/cm^2 is to increase the effective interface width by ~2.5 nm. This broadening includes the combined proton-induced effects of alloying Al in the GaN film and disorder at the interface over the analysis beam region of 25 μm square. Due to systematic broadening introduced by the sputtering beams, this width is regarded as a maximum value. This result suggests that the mobility degradation shown in Figure 5.8 occurs due to disorder at the interface. Also from Figure 5.8, is it apparent that this disorder does not significantly affect the sheet charge density.

5.7 Discussion of results: Lower Fluences ($\leq 10^{14}$ p^+/cm^2)

For lower proton fluences, the primary effects are changes in the electrical contacts of the device. No significant changes are observed for channel transport properties or device figures, e.g., saturation current and transconductance. Cathodoluminescence spectra also do not exhibit changes in this fluence regime.

Ohmic contacts to GaN routinely consist of a thin Ti layer at the metal-semiconductor interface. It is generally accepted that upon annealing the contact (typically ~ 850 C for ~ 60 s) the Ti layer selectively incorporates nitrogen from the GaN, leaving N vacancies in the near-interface region. Such vacancies are known to act as donor states in GaN, and consequently the region near the metal interface is heavily n-type (~ 10^{20} cm^{-3}).[106] For this high degree of doping, the transport across the contact can be treated by a tunneling mechanism. For such transport, the specific contact resistivity approximately exhibits the proportionality[107]

$$R_C \propto \exp\left[C\phi_b \sqrt{\frac{1}{N_d}} \right] \tag{5.1}$$

Here, C is a constant, N_d is the doping level at the metal-semiconductor interface, and ϕ_b is the tunneling barrier height of the interface. An extraction of N_d is not attempted here, as the barrier height is not known, and neither is the Fermi position relative to the conduction edge at the interface, which appears in the full expression for field emission. Either of these variables, especially the barrier height, may be strong functions of fluence as proton-induced chemical intermixing at this interface, similar to the effects observed for higher fluences at the channel interface, is also possible. Such intermixing effects at an initially abrupt interface have been documented for lower energy ion beams on metal/non-metal structures.[108] Assuming momentarily that the unknown variables are not affected by irradiation, the generation of compensating dopants is sub-linear with proton fluence.

Although the changes in contact resistivity (Ω-mm) are small in the present study (8% at 1x10^{11} p$^+$/cm^2 and 18% at 1x10^{12} p$^+$/cm^2, as compared with initial values), they are non-trivial. Furthermore, if the degradation mechanism is similar for exceptionally good contacts (<10^6 Ω-cm^2) it is possible for the irradiation to produce significant relative changes in resistance for comparatively low fluences. Such changes would have to be contemplated for power and frequency requirements for use in irradiation environments.

The changes in Schottky barrier height with fluence are also of importance. Although these changes are too small to significantly affect threshold voltages, the

changes in diode current are evident in Figure 5.5. The initial increase followed by a sub-linear decrease in extracted Schottky barrier height values indicates the possibility of multiple mechanisms based on fluence. The initial increase could indicate either passivation of regions of low barrier height, or a decrease in the image-force lowering effect due to dopant compensation. The decrease in barrier height for fluences in excess of $3x10^{12}$ p^+/cm^2 can indicate a change in electrical properties of the interface, including the possibility of chemical intermixing, which can change the location of Fermi energy level pinning for the Schottky contact. Similar decreases in Schottky barrier height with lower energy proton bombardment have been observed in GaAs diodes, with similar mechanisms proposed to account for these changes.[109]

5.8 Discussion of results: Higher Fluences (>10^{14} p^+/cm^2)

In addition to further degradation in the electrical contacts, the channel transport properties degrade in this fluence regime. The mobility degradation is 20% and 40% at proton fluences of $3x10^{14}$ and $2x10^{15}$ p^+/cm^2, respectively. At $5x10^{15}$ p^+/cm^2 the channel mobility is effectively zero. As discussed previously, our cathodoluminescence and SIMS data indicate a compositional intermixing effect at the AlGaN-GaN interface. For the high sheet densities observed in our samples (~ 10^{13} cm^{-2}), interface roughness is expected to contribute as a limiting factor to mobility.[110,111] As with the contact degradation at lower fluences, future work needs to be done to model the degree of intermixing expected at the AlGaN-GaN interface with MeV proton bombardment at varying fluences. Additional scattering mechanisms, such as scattering from vacancies produced in the vicinity of the channel, can contribute to the mobility degradation. The

sub-GaN NBE emissions observed in the 1 keV spectra for higher proton fluences (Figure 5.9) suggests such vacancies are present, as this beam energy probes the region of the GaN film near to the 2DEG channel.

The 2DEG sheet charge density degrades by 12% and 16% at fluences of $3x10^{14}$ and $2x10^{15}$ p^+/cm^2, respectively, and this quantity is also reduced to near zero at the final fluence. Comparison of this Hall data with our 5 keV cathodoluminescence curves (Figure 5.10) suggests the partial relaxation of strain in the AlGaN film is a contributing factor to the degradation in sheet density. Additionally, dopant compensation in both films at this fluence can depopulate the 2DEG as the Fermi level is shifted away from the conduction edge. A simplified model for the HEMT threshold voltage, which includes the effects of polarization in the GaN and AlGaN films is as follows:[112]

$$V_T = \varphi_B - \frac{qN_D t_{AlGaN}^2}{2\varepsilon} - \frac{\Delta E_C}{q} - \frac{\sigma_{pol}\, t_{AlGaN}}{\varepsilon} \tag{5.2}$$

The first three terms in this equation represent the threshold voltage of a conventional HEMT, with ϕ_B the Schottky barrier height of the gate, N_D the doping in the AlGaN film, and ΔE_C the AlGaN-GaN conduction band discontinuity. The fourth term accounts for the interface charge, σ_{pol}, introduced by the polarization discontinuity between the AlGaN and GaN films. This term includes components from both spontaneous and piezoelectric polarization discontinuities, as well as the effect of partial to full extinction of the latter via strain relaxation in the AlGaN film.

The small, measured changes in Schottky barrier height (~ 40 meV change vs. hundreds of meV change for V_T) are neglected here, and it is noted that for the higher fluence regime the changes in this quantity would indicate a decreased (i.e., more negative) threshold voltage, which is not observed. Based on previous discussion of interface chemical intermixing, there may also be changes in the conduction band discontinuity with increasing fluence, but we assume these changes are small compared with the observed changes in threshold voltage. The two remaining terms in the equation, accounting for doping and polarization charge, are likely to dominate changes in the threshold voltage.

Assuming a maximum unintentional doping level of 10^{18} cm^{-3} in the AlGaN film[113] and inserting appropriate values from Ref. 112 for calculating the polarization charge, we obtain an unirradiated threshold voltage of –6.9 V, which is within 1 V of the measured value (-5.9 V). This calculation assumes the AlGaN film is fully strained. Now, assuming the AlGaN doping is fully compensated, such that N_D=0, the shift in V_T is calculated to be +0.5 V. Such a large compensation may be possible, as carrier removal rates of 3880 cm^{-1} have been measured for GaN films with 1 MeV proton irradiation.[114] Next, holding N_D constant, the total relaxation of piezoelectric strain in the AlGaN film results in a threshold shift in excess of +3.0 V. Furthermore, the complete extinction of the spontaneous polarization discontinuity at the AlGaN-GaN interface (as a possible consequence of chemical intermixing-induced disorder) results in a further shift in threshold of +4.3 V.

The total possible threshold shift, neglecting a change to p-type AlGaN, is then +7.8 V. Our threshold shifts suggest partial changes in these quantites. For example, a

10% reduction in the total polarization charge (σ_{pol}) would shift the threshold voltage +0.73 V, which is comparable to the observed shift between proton fluences of 10^{11} and 10^{14} p^+/cm^2. Notably, the reduction in sheet charge density between these two fluences, as shown in Figure 5.8, is also approximately 10%, which is a reasonable result, as fractional changes in the two quantities should be approximately equal.[115] A similar result is obtained by comparing 10^{11} with 10^{13} p^+/cm^2, where a threshold shift of 0.31 V is observed. This can be accounted for by a 4% change in polarization charge, which is approximately the same as the measured reduction in sheet density.

The changes in threshold voltage for 10^{15} p^+/cm^2 require a reduction in polarization charge of 60%, *including* the effects of total donor compensation in the AlGaN. The measured reduction in sheet charge does not indicate such a severe change in the AlGaN, so we conclude that either there are additional mechanisms which are not taken into account in the simple model (e.g., significant changes in the 2DEG confinement profile due to intermixing), or the unterminated Hall measurement sample and the gated transistor behave differently under proton irradiation. A possibility of the latter case is the formation of charged defects at the metal-semiconductor interface, which is not present in the Hall sample. A similar threshold voltage discontinuity between zero fluence and 10^{11} p^+/cm^2 is present, as in the case of the Schottky barrier height measurement, and might be accounted by passivation effects of the protons.

In general, the degradation observed in device electrical properties is largely accounted for by the large fluence effects. Specifically, saturation current and transconductance decreases are dominated by the change in channel mobility, as sheet charge density is largely unaffected until a fluence >$2x10^{15}$ p^+/cm^2. An important, novel

result of this study is the degradation observed in the electrical contacts of the device. Few reports exist in the literature describing the degradation of these components in nitride compounds subjected to particle irradiation. Chapter 6 focuses in detail on the changes induced to Schottky contacts to gallium nitride via proton irradiation.

CHAPTER 6

DEGRADATION OF SCHOTTKY BARRIERS ON GaN VERSUS FLUENCE AND PROTON ENERGY

6.1 Introduction

As shown in Chapters 4 and 5, irradiation produces damage to the nitride crystal which degrades performance of devices. In addition to bulk crystal defects, the irradiation also causes changes to interfacial boundaries which can affect the two-dimensional transport properties in HEMTs, as well as the performance of ohmic and Schottky electrical contacts. Degradation in ohmic contacts can lead to series resistance effects, which directly affects power dissipation issues. Significantly changes to the Schottky barrier can affect rectifying characteristics. Specifically, irradiation can have significant effects on overall performance of the HEMTs, since reverse biased leakage current in these devices directly limits high frequency and high power performance. It is therefore important to quantify the changes in barrier height and leakage currents as a function of proton fluence, thereby expanding upon the initial Schottky degradation results presented in Chapter 5.

A recent study has shown that Mrad[Si] ^{60}Co γ-ray doses produce degradation in reverse current characteristics for Ni/n-GaN diodes (100 times higher reverse current after 21 Mrad[Si]). The reverse current in that study was restored to pre-irradiation

characteristics following six days at room temperature. Comparison with low energy proton irradiation, including annealing studies, can be useful for comparing degradation mechanisms. For protons, nonionizing energy loss (NIEL) is expected, in addition to the ionizing energy loss (IEL) associated with gamma and x-ray irradiation. Nonionizing degradation mechanisms include the formation of vacancies and higher order complexes. For radiation tolerant materials, such as GaN, the NIEL mechanisms are expected to cause the majority of damage, which may or may not be reversible with thermal annealing. To study such effects, thick films are desired (as compared with heterostructures, e.g., HEMTs) because doping profile techniques such as capacitance-voltage (C-V) can be realized to monitor the creation of compensating traps deep in the bandgap. Current-voltage remains the primary technique to monitor changes in the Schottky barrier height, and the C-V and internal photoemission methods also give further information about the nature of the barrier.

6.2 Schottky barrier diode

Equilibrium conditions for a metal and n-type semiconductor are independently shown in Figure 6.1 (a). It is assumed the workfunction of the metal, ϕ_M, is greater than the electron affinity of the semiconductor, χ_S. When the metal and semiconductor are brought into contact, the conduction electrons in the semiconductor move into the metal, which has a lower energy level than the conduction band. The presence of excess charge

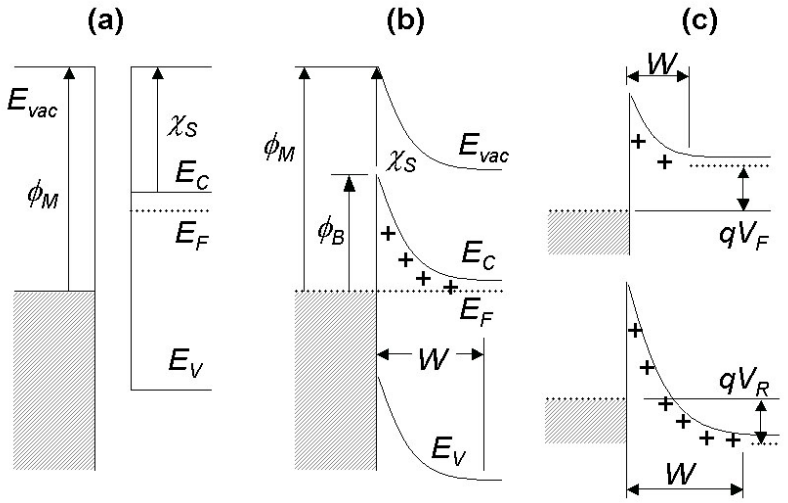

Figure 6.1. Band structure for (a) metal and semiconductor before contact, (b) metal-semiconductor Schottky barrier junction, and (c) barrier under forward and reverse bias.

on the metal, which is now constrained there, repulses additional conduction band electrons in the semiconductor and results in a region of electrically uncompensated donor atoms, which are positively charged. In this region the assumption is made that all of the donors are ionized, assuming they are shallow. In equilibrium, as pictured in Figure 6.2 (b), the Fermi positions in the metal and semiconductor are equal (otherwise charge would flow to achieve this case), and the upwards bending of the conduction and valence bands of the semiconductor is a result of the electric field induced by the uncompensated donors. This region of local band bending is called the space charge or depletion region, due to the presence of these charged atoms and absence of conduction electrons. At the interface, the continuity of the vacuum levels from the metal to semiconductor side implies that the resulting barrier, as seen from the metal side of the interface, is ϕ_M -χ_S, and referred to as the Schottky barrier height of the junction, abbreviated ϕ_B.[116,117] If ϕ_M is less than χ_S, no barrier to current flow exists and the contact

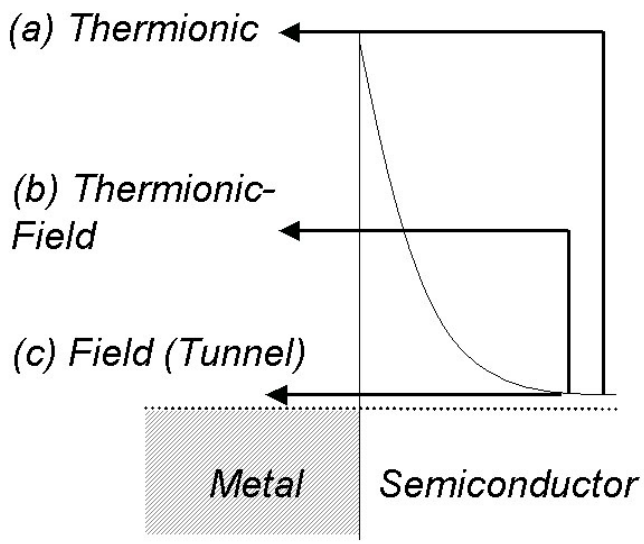

Figure 6.2. Three different cases of current transport across the barrier, shown from the semiconductor to the metal.

is not rectifying, although this case is rarely observed. The total bending of the conduction band from the equilibrium value to the peak value, at the metal-semiconductor interface, is called the built-in potential, V_i. From inspection of Figure 6.1 (b), $qV_i=\phi_B-\phi_n$, where $\phi_n=(E_C-E_F)$.

As shown in Figure 6.2, there are three cases of transport across the barrier, as initially outlined by Padovani and Stratton.[118] The case labeled (a) is called thermionic emission, and here electrons surmount the barrier directly according to the density of states function of the semiconductor conduction band. Case (b) is called thermionic-field emission, and represents the case of intermediate energy electrons in the density of states function (i.e., less than the barrier height) quantum mechanically tunneling through the barrier. In this case, the decrease in density of states with increasing energy is balanced with the increased tunneling probability through the barrier, which is thinner with increasing energy, so the maximum transport occurs at distribution near the middle of the

barrier, as pictured. Case (c) is direct tunneling from the conduction band to the metal, referred to as field emission, and is only dominant if the barrier due to band bending as very thin, as pictured. The field emission case can arise is heavily doped materials, or when a high density of donors is unintentionally created near the metal-semiconductor interface. This is because the total number of uncompensated donor atoms in the depletion region is equal to the total charge on the metal, such that the junction is electrically neutral, and therefore the depth of the depletion region is therefore smaller for more heavily doped semiconductors. This depth, called the depletion width W, is given by

$$W = \left(\frac{2\varepsilon_S}{qN_d} |V_i - V| \right)^{1/2} \tag{6.1}$$

where N_d is the donor concentration below the contact and ε_S is the dielectric constant of the semiconductor. For very small widths (~10Å or less) tunneling through the thin region of sharp band bending is likely. Also from this expression, the depletion width is a function of applied bias, and becomes larger with increasing reverse bias (V negative) and smaller for increasing forward bias.[116,117] A useful parameter for estimating dominant current transport mechanisms is the energy parameter E_{00}, which is defined as

$$E_{00} = \frac{qh}{4\pi} \left(\frac{N_d}{m^* \varepsilon_S} \right)^{1/2} \tag{6.2}$$

where h is Plank's constant and m^* is the electron effective mass. For $E_{00} << kT/q$ thermionic emission is expected to dominate, and for $E_{00} >> kT/q$ field emission should dominate. For intermediate values of E_{00}, one expects thermionic-field emission or a combination of the transport mechanisms.[119]

The junction operates by two components of current flow: current from the metal to the semiconductor, and the opposite case. Since the metal and bulk semiconductor (outside W) are both conductive, and the depletion width is resistive (due to the absence of carriers), the voltage drop induced by a bias appears mostly across the depletion width. Then, when a forward bias is applied to the metal, the Fermi levels in the on either side of the depletion width are separated by the applied bias, and the band bending in the depletion region is correspondingly reduced. This implies the conduction band density of states function is elevated relative to the top of the barrier, and current flow is increased rapidly with increasing forward bias. In reverse bias the opposite is true, as the conduction band energies are reduced relative to the barrier, and current is reduced significantly. The metal to semiconductor component, by contrast, is unaffected by bias, as electrons with sufficient energy to overcome the barrier are swept through the depletion width for all cases. This mechanism is analogous to the minority carrier reverse current in a p-n junction diode. This component is the dominant mechanism in reverse bias, but negligible for forward biases $>3k_BT/q$, due to relative magnitudes of the two components.

Based on these two components, the theoretical expression for the current, I, as a function of applied forward or reverse bias voltage, V, arising from thermionic emission across a Schottky barrier with barrier height ϕ_B is

$$I = AA^{*}T^{2}\exp\left(-\frac{q\phi_B}{k_BT}\right)\left[\exp\left(\frac{qV}{nk_BT}\right)-1\right] \tag{6.3}$$

Here A is the diode area, A^* is Richardson's constant (=26 and 32 A/cm^{2}K^2 for GaN and AlN, respectively), T is the temperature in Kelvin, k_B is the Boltzmann constant, and n is the ideality factor. For an ideal diode exhibiting pure thermionic transport, n=1. Current arising from generation-recombination current due to defects in the depletion region of the diode result in n=2, and larger idealites can be observed in practice due to competing current conduction mechanisms and defects at the interface, among other factors. The bracketed expression contains the forward and reverse conduction terms, in that order.

Electrons approaching the metal from the semiconductor side induce a virtual image charge in the metal, which satisfies the equivalent electrostatic problem to the physical distribution of charge arranged on the metal, at the interface, in response to the incoming charge. The superposition of the band diagram and the electrostatic potential from the image charge, as a function of distance from the interface, results in an effective lowering of the barrier height due to the additional attraction to the image charge. Due to this addition, the barrier lowering is a function of doping in the material and applied bias, since these factors result in different electric fields in the depletion region.[116,117] The degree of image force lowering is given by[116]

$$\Delta\phi_B = \left[\frac{q^3N_d}{8\pi^2\varepsilon_d^2\varepsilon_s}\left(V_i - V\right)\right]^{1/4} \tag{6.4}$$

Here, ε_d is the high frequency dielectric constant, often approximated by ε_S. V can be negative or positive, and the corrected barrier height is $\phi_B = \phi_B^0 - \Delta\phi_B$.

Another method for the measurement of Schottky barrier height is internal photoemission, where the barrier is illuminated with monochromatic light. For sufficient photon energies, photoexcited electrons in the metal can surmount the barrier and travel into the semiconductor, where they are swept away from the interface by the built-in junction field. Fowler originally showed that photoelectrons emitted from a clean metal surface to vacuum exhibit a photocurrent R (i.e., electrons per incident photon) approximately proportional to the square of the difference between the incident photon energy and workfunction of the metal, such that $R \sim (h\nu - \phi_M)^2$ for photon energies greater than $\sim\phi_M$+0.1 eV.[120] This formalism was later shown to be valid for Schottky barriers on semiconductors, with $R \sim (h\nu - \phi_B)^2$ in that case. For either case, a plot of the square root of the photocurrent vs. photon energy (commonly called a Fowler plot) should be a straight line for photon energies in excess of ~0.1 eV greater than the barrier. In practice, the current from the unbiased Schottky contact is measured with a current meter while the contact is illuminated with a monochromatic light source, with the ohmic contact grounded to complete the circuit. Typically, a white light source is passed through a monochromator, which is then swept through the spectral range of interest to generate a current vs. photon energy plot. A power measurement is then performed with a calibrated detector, and since power is proportional to the product of the number of photons and the photon energy, the photon density is obtained by dividing the power result by photon energy. Photocurrent is then proportional to $I/(P/(h\nu))$, where P is measured calibrated power.

For inhomogeneous diodes, regions of low barrier height tend to dominate the I-V characteristics due to the exponential nature of the thermionic emission expression. This

is true even if the low barrier regions comprise only a small fraction of the total diode area. By contrast, the photoresponse of the diode represents a spatial average of all regions of the diodes, and for this reason internal photoemission can give additional information about the true nature of the barrier height on the semiconductor. Also, for the preceding reason, $\phi_B^{IV} \leq \phi_B^{IPE}$, with the equality case accounting for homogeneous diodes. Should there be multiple discrete barrier heights in a single diode, each comprising comparable fractions of the area of the diode, it is also possible to independently fit multiple barrier heights on a single Fowler plot.

A final common method for measurement of Schottky barrier height uses capacitance-voltage profiling. When a small (~15 mV) alternating voltage is added to the dc component of a reverse biased Schottky barrier, a capacitance term arises from the small fluctuation in depletion width, and hence number of uncompensated dopants, due to the ac term. Assuming uniform doping, the inverse of capacitance squared varies with reverse voltage, V_r, as

$$\frac{1}{C^2} = \frac{2}{A^2 q N_{deff} \varepsilon_S}\left(\phi_B - \xi + V_r - \frac{kT}{q}\right) \tag{6.5}$$

with $\xi=(kT/q)\ln(N_c/N_d)$, with N_c=2.6x10^{18} cm^{-3} for GaN, and N_{deff} is the effective doping ($=N_d$-N_a). A plot of $1/C^2$ vs. V_r should then be a straight line with slope proportional to the effective doping and y-axis intercept proportional to the barrier height. In addition to an alternative measurement of a barrier height, the C-V technique has the added benefit of directly measuring the doping of the material, which can be used to evaluate image force

lowering from I-V and internal photoemission measurements. Moreover, since the capacitance term arises from the effective doping at the depletion edge, it can be shown that the derivative of the $1/C^2$ vs. V_r curve is proportional to the local effective doping at a depth of $\varepsilon_0\varepsilon_r A/C$. In this way, the C-V method provides a powerful tool for measuring the effective doping as a function of depth into the material, which can be monitored as a function of annealing to reveal changes in doping due to passivation or creation (e.g., vacancy formation). Due to the sensitivity of C-V to states at the metal-semiconductor interface, $\phi_B^{IPE} \leq \phi_B^{CV}$ is generally observed, implying C-V gives the highest values for barrier height of any of the methods discussed.

6.3 Growth and experimental details

The devices were grown at the University of California—Santa Barbara using the metal-organic chemical vapor deposition (MOCVD) technique, and consisted of a sapphire substrate followed by 2 μm of Si-doped GaN (target doping ~$3x10^{16}$ cm^{-3}). Ohmic (Ti/Al/Ni/Au: 200/1500/375/500Å, with a 30 s 850 °C rapid anneal) and Schottky (Ni/Au: 300/4000Å) contacts were patterned with standard optical lithography techniques and deposited with electron beam lithography. The Schottky contact geometry is shown in Figure 6.3, with the ohmic contact surrounding the Schottky contact. Each die consists of multiple diodes, and several were tested for each experiment. 1.8 MeV Proton irradiation was conducted at Vanderbilt University in vacuum and at room temperature, using a Van de Graaff accelerator. I-V, C-V, and internal photoemission measurements were taken before irradiation and after each fluence or annealing step.

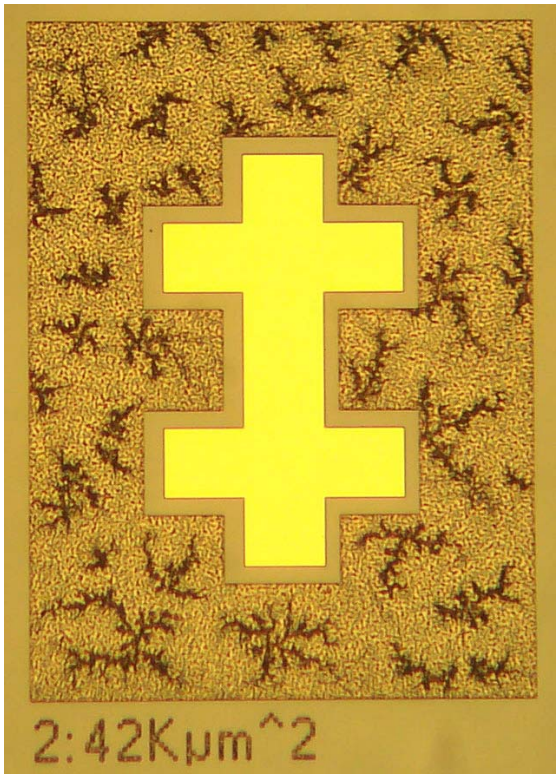

Figure 6.3. Representative Ni/Au diode on GaN (center cross), surrounded by the ohmic contact. Each die consisted of several diodes with similar geometries and a TLM structure.

6.4 Irradiation results

Diode I-V curves for successive 1.8 MeV proton fluences are shown in Figure 6.4 for a representative device. The magnitude of reverse current slowly increases with increasing fluence, starting with the lowest fluence ($3x10^{11}$ p^+/cm^2). These changes are consistent throughout the reverse bias voltage range, and result in the current doubling through a fluence of 10^{13} p^+/cm^2, as compared with the unirradiated curve. A similar trend is observed in the lower bias region (<0.15 V) of the forward current. These changes suggest changes in the Schottky barrier height (ϕ_B) of the diode. Extractions of this quantity and the ideality factor of the diode (n) are shown in Figure 6.5. These values

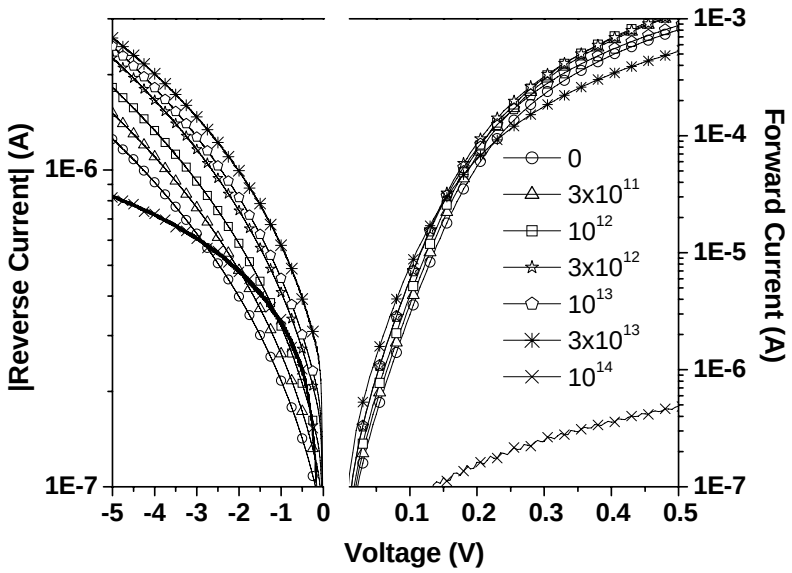

Figure 6.4. Current-voltage characteristics as a function of proton fluence for a representative device. For clarity, not all data points on each curve are shown.

were extracted using the thermionic emission method described in Section 6.2 from ~0.07 V to ~0.15 V in the forward bias region of the curves (A^*=26.4 A/cm^2/K^2 for GaN). The results in Figure 6.5 are an average of the three diodes tested. These curves show a decrease in ϕ_B, consistent with the increase in reverse current and low-bias forward current. A decrease of ~5 meV for each successive fluence is observed, and the total change is ~30 meV through 10^{13} p$^+$/cm^2. It is important to note that this trend in Schottky barrier is opposite to that reported in Ref. 77 for γ-ray irradiation, suggesting different damage mechanisms. A change in ideality factor is also observed here for fluences in excess of $3x10^{11}$ p$^+$/cm^2, with a steady increase from 1.07 to 1.14 from $3x10^{11}$ to $3x10^{13}$ p$^+$/cm^2. Changes in reverse current and ideality were not observed in room temperature 1.8 MeV irradiation of Ni/GaN diodes in Chapter 5 (in which 300K proton irradiation of the HEMT structures with a Ni Schottky gate did produce similar

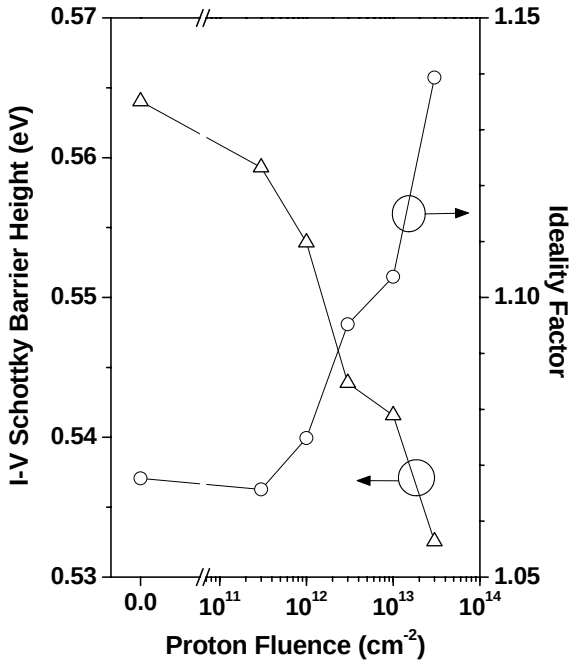

Figure 6.5. Schottky barrier height and ideality factor as a function of proton fluence, as extracted from the low-bias (<15 mV) forward voltage region of the diode curves. The values represent an average of three diodes.

changes to barrier height), which suggests a variation in irradiation effects for different material growths and processing conditions.

For the higher current forward bias region of the Figure 6.4 I-V curves, a general decrease of current is observed. This effect is also evident in the higher fluence reverse current curves, and is suggestive of increasing series resistance with proton fluence. This is the combined resistance of the external measurement probes, ohmic contacts, and material resistivity. The first source of resistance are expected to be small, so the effect is primarily due to changes in the GaN resistivity and ohmic resistivity. By performing a linear fit of $I^*(\partial I/\partial V)^{-1}$ vs. I, as described in Ref. 120, the series resistance for three diodes is extracted and shown in Figure 6.6. The onset in significant change

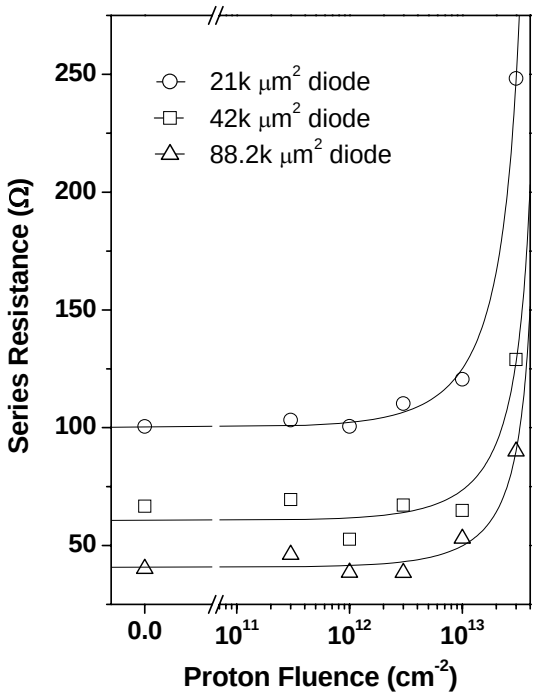

Figure 6.6. Series resistance as a function of proton fluence for three diodes with different sizes and geometries. The values were extracted from the I-V curves of the respective diodes by the procedure described in the text. At a fluence of 10^{14} p^+/cm^2, the diodes were highly insulating.

in series resistance is observed at ~10^{13} p^+/cm^2. This quantity approximately doubles for a fluence of $3x10^{13}$ p^+/cm^2, and for 10^{14} p^+/cm^2 the value was hundreds of kΩ for all diodes. Using a TLM structure similar to that presented in Chapter 5, contact resistivity and sheet resistance are extracted and shown in Figure 6.7 as a function of fluence. The onset of significant degradation for each quantity occurs for fluences >$1x10^{13}$ cm^{-2}. The common onset fluence suggests a common degradation mechanism, most likely in the form of compensating defects decreasing the effective doping in the bulk GaN and near the ohmic contacts. In the latter case, a reduction of doping in the vicinity of the contacts can reduce tunneling current achieved by the highly doped nature of the intimate contact.

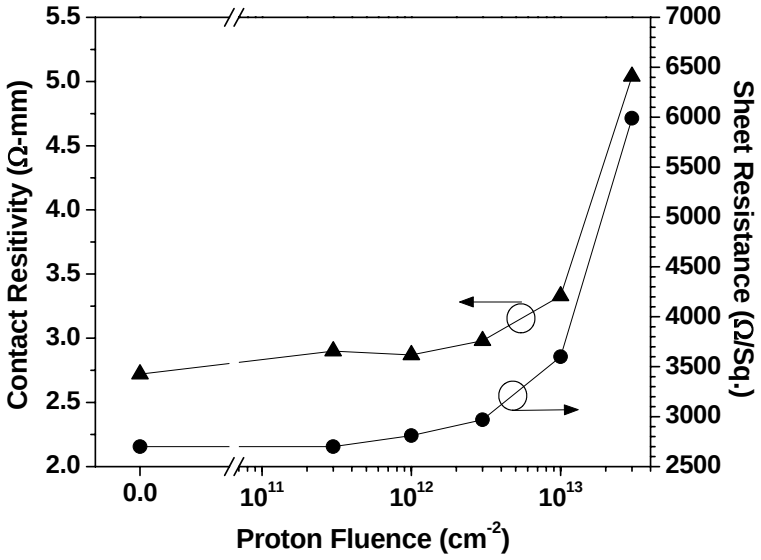

Figure 6.7. Sheet resistance and contact resistivity as a function of 1.8 MeV proton fluence, extracted from the TLM structure.

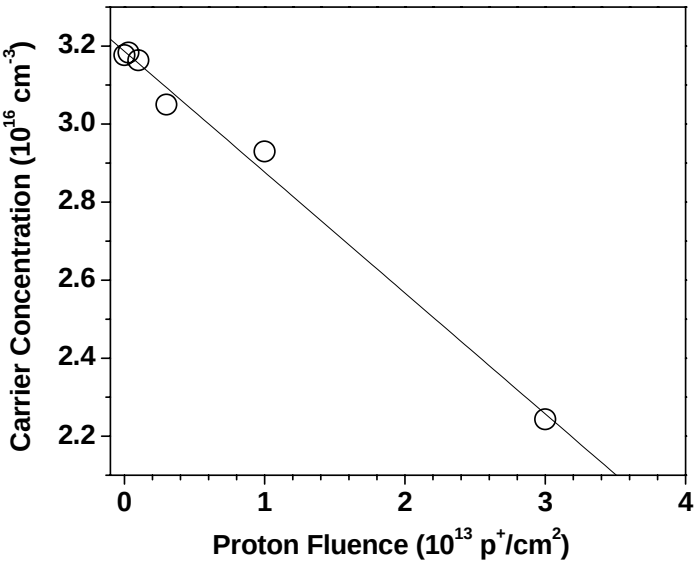

Figure 6.8. Carrier concentration as a function of proton fluence, as extracted from capacitance-voltage measurements by the procedure described in the text. The values represent an average of three diodes.

To quantify the effects of compensating defects, capacitance-voltage (C-V) data were obtained on the GaN diodes. Figure 6.8 shows the average carrier concentration as a function of proton fluence for three diodes. This plot was generated by analysis of $1/C^2$ vs. V plots, as described in Section 6.2 and Ref. 117. Figure 6.8 indicates a carrier removal rate of ~300 cm^{-1} from the unirradiated value of ~$3x10^{16}$ cm^{-3}, as extracted from a linear fit. This value is consistent with previously reported studies of proton irradiated GaN.[121] The removal of free carriers largely accounts for the increase in series resistance seen in Figure 6.6, as the conductivity of the material decreases. The onset of higher series resistance at $3x10^{13}$ p^+/cm^2 and the very large resistance at 10^{14} p^+/cm^2 is consistent with the data in Figure 6.8, as the linear fit extrapolates to an insulating transition at ~10^{14} p^+/cm^2. Thus, the decrease in large-bias diode currents for higher proton fluences shown in Figure 6.4 (particularly at 10^{14} p^+/cm^2) are attributed largely to a decrease in carrier concentration, likely due to the formation of compensating defects, which directly affects series resistance. Furthermore, this effect suggests a contributing mechanism for the increase in ideality factor (shown in Figure 6.5), as these defects are formed within the depletion width.

When corrected for series resistance, the low-forward bias region of the Figure 6.4 curves, and hence the Schottky barrier and ideality factor results in Figure 6.5, are not affected significantly. An additional effect to consider is the image force lowering correction to the Schottky barrier height, as detailed above. This effect lowers the effective Schottky barrier, as extracted from the I-V curves, and in general becomes more pronounced with higher doping levels (i.e., higher electric field in the depletion width). It is important to characterize whether the extracted irradiation-induced Schottky changes

are affected by changes in this correction factor. A procedure for calculating the image force lowering is given in Section 6.2 and Ref. 122. This calculation gives a correction of ~45 meV for the unirradiated diodes (i.e., the I-V extraction in Figure 6.5 is 45 meV low), and ~41 meV for the $3x10^{13}$ p^+/cm^2 fluence. The intermediate fluences lie close to the initial value of 45 meV. Notably, the image force lowering *change* of 4 meV, with irradiation, is small compared with the changes in ϕ_B shown in Figure 6.5. Additionally, the image force lowering produces the opposite trend in ϕ_B with fluence. We therefore neglect this effect, except in noting that the corrected unirradiated Schottky barrier is ~0.61 eV.

Capacitance-voltage (C-V) and internal photoemission measurements of the barrier height are shown in Figures 6.9 and 6.10, respectively. The initial value of barrier height extracted form the C-V data is ~0.65 eV and the data show a similar trend to the I-V results as a function of fluence. The internal photoemission gives a similar result for barrier height compared with the I-V and C-V, but the uncertainty associated with barrier heights are too large to observe the tens of meV changes in barrier from the other two methods. Importantly, the general agreement between I-V and C-V results suggest that the diodes are largely free of interface states and insulating layers that generally affect C-V data and extraction of the barrier height from the I-V method. This is also confirmed with the extracted values of barrier height from the internal photoemission method. Moreover, the linear nature of the internal photoemission and agreement between all three methods suggests strongly that the diodes are spatially uniform, and I-V values are accurately extracted.

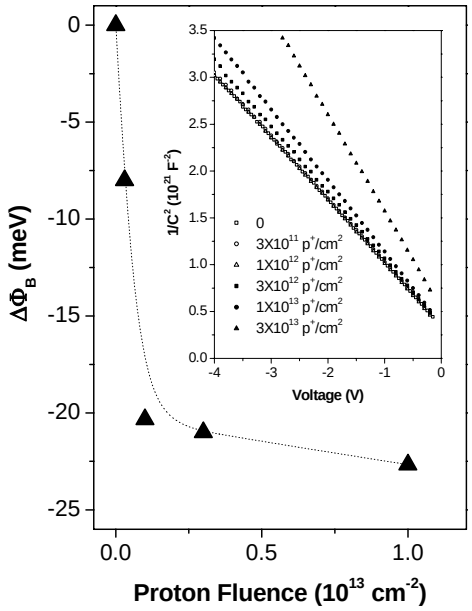

Figure 6.9. Capacitance-voltage determination of change in barrier height versus proton fluence. The zero fluence barrier height was 0.65 eV. Inset: Raw $1/C^2$ vs. V data (not all points are shown for clarity).

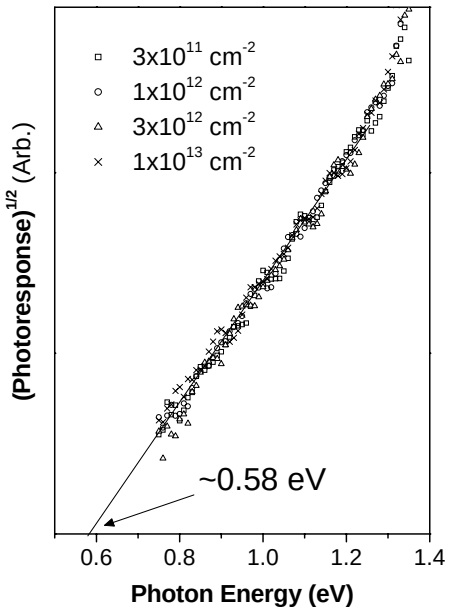

Figure 6.10. Internal photoemission data for the Schottky barrier as a function fluence. The uncertainty in extracted values does not permit extraction of a change with fluence, although the raw data suggest a spatially uniform barrier in agreement with the other methods.

6.5 Annealing of irradiation damage

Subsequent I-V and C-V monitoring of the diodes after the terminal fluence of 10^{14} p^+/cm^2 indicated no significant improvement of the devices after room temperature (RT) annealing of ~20 days. A subsequent robust anneal at 225 °C for 2 Hrs. restored the carrier concentration to ~$1x10^{16}$ cm^{-3} (one-third of the initial value). Figure 6.11 shows I-V curves for this annealing experiment. The I-V extracted ideality factor was restored completely (within measurement uncertainty), but the Schottky barrier was increased compared with the pre-irradiation value (0.6 eV vs. 0.56 eV, uncorrected for image force lowering). This change in of 40 meV accounts for the difference of approximately five times the reverse and low-bias forward currents. Furthermore, the incomplete restoration in carrier concentration leads to series resistance effects which result in a larger discrepancy for forward biasing greater than ~0.5 V. As before, calculations of image force lowering reveal a minimal (~3 meV) difference in this quantity for the two curves.

A second annealing experiment was conducted after a terminal fluence of $5x10^{13}$ p^+/cm^2, which is prior to the insulating transition. Extracted series resistance for a representative diode and an average carrier concentration from multiple diodes are shown in Figure 6.12 for various successive annealing temperatures, for 30 minutes at each temperature. The series resistance and carrier concentration follow complementary trends, as anticipated, and unirradiated control diodes indicate no changes in carrier concentration for the annealing steps. I-V curves for this annealing experiment are shown in Figure 6.13. When compared with the unirradiated I-V curves, the $5x10^{13}$ p^+/cm^2 curves exhibit increased reverse current, due to a decrease in ϕ_B, and decreased large-bias forward current, due to increase in series resistance. These results are in agreement with

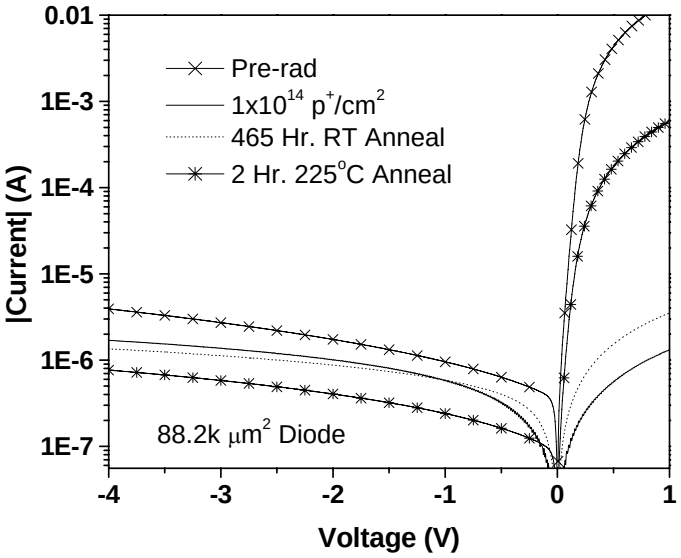

Figure 6.11. I-V data for the first annealing procedure. The degradation in the barrier is minimal for several days at room temperature.

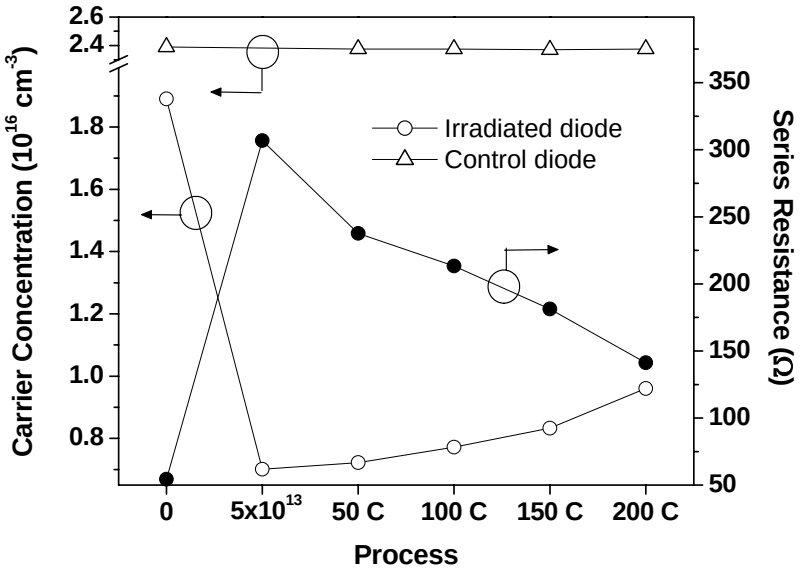

Figure 6.12. Effects of the second annealing experiment on carrier concentration and series resistance. Both quantities are partially recovered for low temperature annealing.

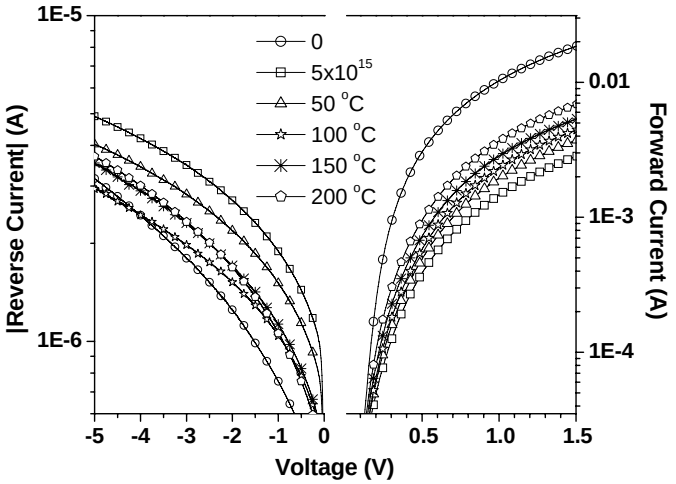

Figure 6.13. I-V data for the second annealing experiment vs. proton fluence.

the data in Figure 6.11. Subsequent annealing steps add successive restoration of the forward current towards unirradiated values, due to the decrease in series resistance from an increase in carrier concentration. Reverse current is initially improved (decreased) through the 100 °C anneal, but then degrades slightly for the final two temperature steps. The other diodes tested show generally similar behavior at the final two annealing steps, as do the unirradiated control diodes. This suggests a possible additional effect independent of the irradiation and annealing processes.

Comparison of Figures 6.11 and 6.13 reveal the different annealing effects based on irradiation fluence and precise procedure. For example, in Figure 6.11, the effect of a lengthy anneal is to decrease both the forward and reverse current. By contrast, the final two annealing steps shown in Figure 6.13 produce an increase in reverse current (in both the irradiated and control diodes), with a decreased forward current, as compared with unirradiated values. The reasons for these differences include the simultaneous changes

in several variables, e.g., series resistance, Schottky barrier, and other effects due to annealing and unrelated to irradiation. In any case, it appears unlikely that changes in reverse and forward bias characteristics of these Schottky barrier diodes can be simultaneously restored by a simple annealing procedure. This is in contrast with the 21 Mrad[Si] γ-ray study, where restoration was achieved with 1 Hr. 150°C annealing.[77]

6.6 Dependence of irradiation damage on proton energy

Previous work on GaN-based light emitting diodes (LEDs) showed the degradation caused by 2 MeV protons is significantly higher than that of 10 MeV protons.[123] Additionally, previous studies of proton-irradiated nitride HEMT structures have addressed the changes to the device as a function of proton fluence and multiple proton energies.[124] It was found that in the MeV range of proton energy, damage was increased for lower proton energies. Specifically, 1.8 MeV protons caused higher degradation in HEMT saturation currents and transconductance than 40 and 105 MeV protons. Examination of SRIM simulations of nonionizing energy loss (NIEL) values versus proton energy explain the energy dependence. For the particular HEMT structure used in the study, the NIEL values extracted from the simulation showed the following values for 1.8, 15, 40, and 105 MeV protons, respectively: 3.1, 0.27, 0.1, and 0.05 eV/proton. The NIEL values, responsible for displacement damage affecting the HEMTs, are significantly higher for lower proton energies. This can be understood in terms of interaction time of the charged protons with the lattice atoms as they lose energy

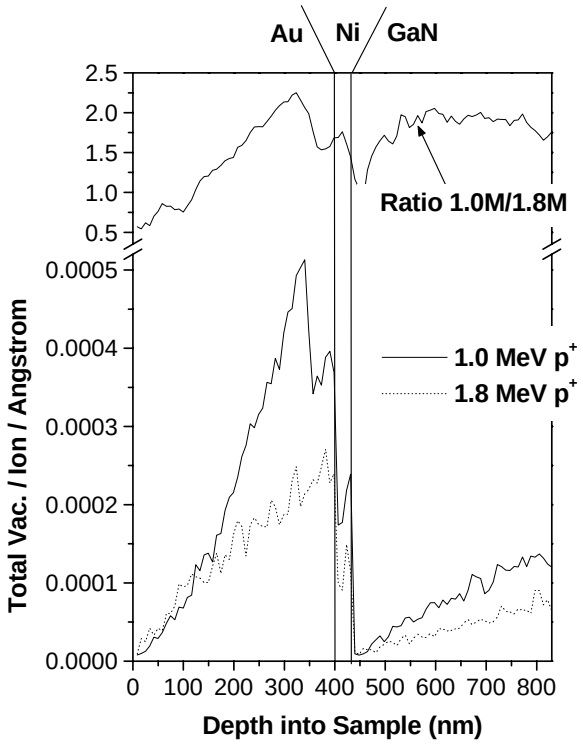

Figure 6.14. Total vacancy production vs. proton energy for 1.0 and 1.8 MeV protons, as calculated from SRIM. The 1.0 MeV protons produce 1.5-2.0x as many vacancies.

traveling deep into the lattice (as noted in Chapters 4 and 5, direct lattice collisions are rare; the range of MeV protons in GaN is several microns, with a small statistical variance in penetration depth). The lower energy protons are slower particles and reside near lattice sites for longer periods. This increase in lattice interaction results in higher NIEL values and larger vacancy concentrations.

To address the energy dependence of GaN Schottky barrier degradation, diodes were also irradiated with 1.0 MeV protons, to compare with the 1.8 MeV results previously discussed. This range of proton energies defined the practical experimental limits for the Van de Graaff accelerated used here. The calculated NIEL values for this

structure show that 1.0 MeV protons are approximately 1.7 higher than the 1.8 MeV case. NIEL results, in the form of maximum vacancies produced by the protons, are shown in Figure 6.14 for both energies. As with the NIEL figure, the ratio of vacancies (shown in the upper region of the figure) is approximately two, and would converge to this value for a sufficiently large number of simulated protons (shown: one million).

Effective doping changes for each proton energy, as extracted from C-V, are shown in Figure 6.15. As expected from the NIEL results, the change in effective doping occurs at a rate approximately 60% faster for the 1.0 MeV protons versus the 1.8 MeV case. Series resistance also degrades faster for the 1.0 MeV case. Figure 6.14 shows a comparison of changes in contact resistivity and sheet resistance for both proton energies, as extracted from TLM structure measurements. For each quantity, the onset of degradation is delayed for the 1.8 MeV case by approximately a factor of two in fluence, in accordance with the NIEL results. Finally, changes in Schottky barrier height, as extracted from thermionic fits of the I-V characteristics, are shown in Figure 6.16. Changes are considered here due to slight differences (<25 meV) in the initial values of barrier height for the two sets of diodes. The fits shown are second order exponential decay functions, which provide a reasonable guide for the eye. As before, image force lowering is calculated by using the effective doping values shown in Figure 6.15. It is shown to have minimal effect on the trends, and in particular, on the difference in degradation between 1.0 and 1.8 MeV protons. The salient feature from the figure is the enhanced degradation in Schottky barrier height for the 1.0 MeV protons, as with the other monitored quantities (e.g., doping, resistance, etc.). Again, the difference in NIEL for 1.0 versus 1.8 MeV protons accounts for these changes.

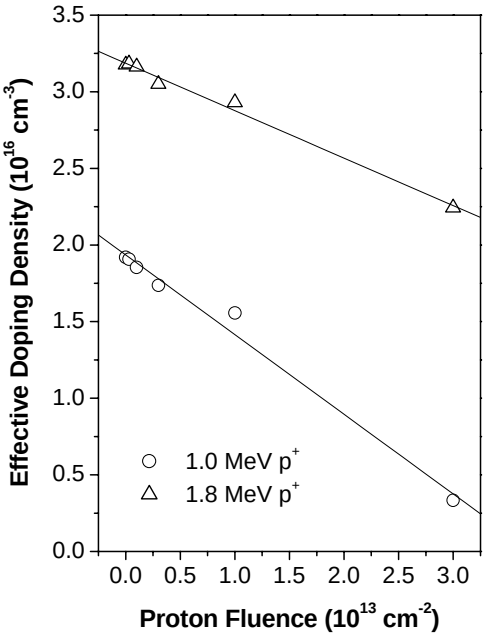

Figure 6.15. Changes in effective doping density with proton fluence. For 1.0 MeV protons, the carrier removal rate is ~520 cm^{-1}; for 1.8 MeV protons, this rate is 310 cm^{-1}. The ratio of doping compensation is consistent with the SRIM calculations.

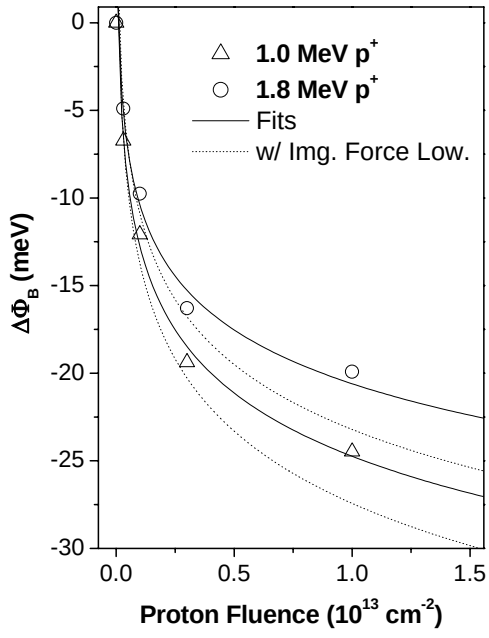

Figure 6.16. Changes in Schottky barrier height with proton fluence for 1.0 and 1.8 Mev protons. As with effective doping, the 1.0 MeV protons are more damaging.

6.7 Discussion of results

The degradation in series resistance and can be accounted for by the formation of compensating defects in the GaN, as confirmed by the C-V data. The increase in ideality factor also suggests increased competition for total diode current from generation-recombination components (which theoretically exhibit ideality factors of 2) originating from traps in the depletion width. Additionally, the increase in contact resistivity is consistent with a decrease in effective doping in the vicinity of the ohmic contact. In this case, a reduction in localized doping in the metal-semiconductor interface region can change the transport from tunneling in nature to an intermediate transport case. For these cases, the contact resistance is expected to follow the form $R_C \sim \exp(k/\sqrt{N_d})$, where k is a constant and N_d is the effective doping, which is consistent with the agreement in onset of significant degradation between the measured doping and contact resistance.

These compensating defects are created from the nonionizing component of the incident protons, and may include atomic displacements, vacancies, interstitials and associated defect clusters in the crystal. The general agreement between comparative degradation in the diode figures for the 1.0 versus 1.8 MeV cases and the corresponding NIEL results confirms the nonionizing component is the main degradation mechanism (as opposed to ionizing proton energy loss or simply a result of total fluence). Candidates for lattice defects include shallow donors, which have been previously reported in GaN-based diodes irradiated with protons. These defects have been attributed to the nitrogen vacancy (V_N) and the nitrogen antisite (N_{Ga}).[125] The nitrogen antisite is a metastable state associated with a gallium vacancy (V_{Ga}) and a doubly charged nitrogen interstitial (N_i^2).[125,126] Deep levels attributed to gallium-hydrogen complexes have also been

reported in GaN-based thin film structures irradiated with 1-MeV neutrons.[127] Additionally, a gallium interstitial (Ga_i^{2+}) formed in GaN thin films after 2.5-MeV electron irradiation at 4.2 K was observed to be stable at low temperatures.[128] This interstitial was observed to be mobile at room temperature and formed higher order defect complex.[129]

The presence of traps in the GaN removes free carriers in the devices,[121,130] leading to lower carrier concentration. This affects the effective doping, as measured from C-V, and sheet resistance, and contact resistance. As noted, the degradation of contact resistance is highly correlated with doping sheet resistance changes, further indicating the common mechanism. Due to the decrease in effective doping, gallium vacancies and related complexes are expected to be the primary irradiation induced traps. These traps act as deep acceptors and compensate the silicon doping. Indeed, SRIM simulations indicate NIEL figures for gallium are about four times higher than the figure for nitrogen, owing to the large cross section of gallium.[131] The gallium interstitials created by radiation are mobile at room temperature, and these atoms can diffuse through the lattice and form stable complexes with other defect types such as vacancies, antisites, and other lattice imperfections.[128,129] These gallium-related defect complexes involving interstitials, vacancies and antisites are stable until relatively high temperatures, unlike simple vacancy-interstitial pairs, which can annihilate for low temperatures.[130,132] The presence of these thermally stable complexes is supported by the thermal stability of the irradiation-induced damage, include incomplete restoration of carrier concentration through length anneals at elevated temperature. Previous researchers have similarly noted that the degradation in GaN thin-films irradiated with 0.6 MeV protons can be

recovered after annealing treatments above 225 °C. Notably, nitrogen vacancies, which act as shallow donors, have been shown to thermally anneal at lower temperatures,[133] further implying that the main irradiation-induced defect in the bulk is related to the gallium vacancy.

The changes to the Schottky barrier do not follow the trend observed with material resistivity and ohmic contact degradation. Degradation in the barrier height is immediate, and approximately exponential with proton fluence, which is different from the removal of carriers, which is linear with fluence. As noted previously, image force lowering cannot account for the changes in Schottky barrier, since decreased doping raises the apparent barrier height according to $\Delta\phi_B \sim N_d^{1/4}$.

Another explanation for the Schottky behavior is the formation of a large density of states at the metal-semiconductor interface. In sufficient density, such states can locate or "pin" the Fermi level to a particular energy in the bandgap, thus determining the semiconductor band bending and resulting Schottky barrier height, irrespective of the barrier predicted from the Schottky relation, $\phi_B = \phi_M - \chi_S$, where ϕ_M is the metal workfunction and χ_S is the electron affinity of the semiconductor. The application of the Schottky rule for Ni-GaN diodes predicts a barrier height of 1.05 eV ($\phi_M = 5.15$ eV for nickel and $\chi_S = 4.10$ eV for GaN). The I-V measured value is approximately 0.6 eV, however, after correcting for the image force effects. This implies the as-grown diodes have a large density of surface states before irradiation. Previous studies of reactive-ion etched GaN surfaces have shown a highly pinned surface with the Fermi level located 0.5 eV below the conduction edge, thereby resulting in a barrier height of 0.5 eV regardless

of metal.[134] In this study, surface composition after etching was found to be deficient in nitrogen atoms, thereby suggesting that the primary defect responsible for the surface Fermi pinning is nitrogen vacancy related complexes. Indeed, other investigators have accounted for anomalous current densities in as-grown metal-GaN Schottky barriers by developing a model in which the near-interface region contains a high density of donor states 0.5 eV below the conduction edge, which is correlated with nitrogen vacancies.[135] The correspondence between the results in Refs. 134 and 135 and the barrier heights reported here suggest a high denisty of nitrogen vacancies near the interface.

For this study, the downward trend in barrier height suggests that the proton irradiation increases the pinning effect by the formation of additional defects at the metal-semiconductor interface. It is apparent that the defects must be near the conduction edge, since the barrier decreases with proton fluence. A probable candidate for the new defects is additional nitrogen vacancies created by the proton irradiation, possibly very near to the interface. The C-V measurements discussed previously will not detect these near-surface effects, as the sensing depth is ~0.2 μm and deeper. Additionally, the interface intermixing effects introduced in Chapter 5 may imply enhanced stability of the nitrogen vacancy complexes as nickel and the displaced nitrogen atoms interact. Nickel-nitrogen interactions have been observed for Schottky diodes annealed at 500 °C, due to the decomposition of nitrogen from the lattice.[136] In the proton-irradiated case, the nitrogen is freed from displacements, and this could result in the formation of similar stable compounds. Moreover, if intermixing plays a role in the degraded barrier properties, thermal annealing is unlikely to recover the changes in barrier height. In point of fact, the annealing data for barrier height shown in Figure 6.12 indicates partial recovery (i.e., an

increase in barrier), although a reference die annealed at the same time exhibits a downward trend in barrier for the same temperatures. The partial recovery of the irradiated diode indicates that there may be additional mechanisms also affecting the barrier height, in addition to near-interface nitrogen vacancy complexes. Possible candidates might include gold and nickel defects and complexes in the GaN arising from intermixing, gallium vacancy related complexes, or hybrid states at the interface of the metal and semiconductor.

CHAPTER 7

ELECTRICAL CHARACTERIZATION OF SCHOTTKY BARRIERS ON AlGaN VERSUS SURFACE TREATMENT, METAL, AND LOW TEMPERAUTRE THERMAL ANNEALING

7.1 Introduction and motivation

Schottky metals have primarily been chosen for their high workfunctions, which should result in large barrier heights on n-type material (see Chapter 6). Metals used on the nitride system have included Ni, Ir, Pd, Pt, Re, Au, Cu, and WSi_x alloys, with Ni and Ir presently being the most common. An advantage of high barrier heights for Schottky transistor gates is the low leakage (i.e., reverse) current observed from the gate to the channel when the channel current is off. Gate leakage current is a main contributing factor to high frequency noise in HEMTs. Thermal stability of gate currents is of interest for these devices, as channel temperatures during continuous operation have been estimated to be in excess of 350°C for 6W/mm power density[137], and degradation of barrier properties have been reported for annealing conditions as low as 300°C for five minutes for Pd Schottky diodes.[138] By contrast, other metals have been shown to exhibit improvements in barrier heights with high temperature annealing. For example, leakage currents for Ni diodes have been reduced by three orders or magnitude after annealing at 700°C for 30 minutes.[139] In general, barrier heights and thermal stabilities of Schottky barriers are dependent upon the metal, semiconductor alloy composition, surface

preparation, and specific device structure. In principle, studies of multiple adjacent metals on the same semiconductor piece can eliminate three of these variables.

Typical surface preparation on nitrides prior to Schottky deposition includes a wet etch, typically HCl, $(NH_4)_2S$, or a buffered-oxide etch, all chosen to remove contaminants and thick oxide layers which can affect gate performance in unpredictable ways from one wafer to the next. By etching, a more "standard" surface is prepared, where contaminants are removed across the whole piece. Another preparation technique of recent interest for GaN-based transistors is plasma etching of the semiconductor. This is required in nitrides since chemical etch rates are impractically slow or zero. Reactive ion etching (RIE) and/or inductively-coupled plasma reactive ion etching (ICP-RIE) are commonly used for mesa isolation of adjacent devices, where the material is removed until an insulating layer of the device structure is exposed. Another application is etching the conductive GaN layer (MESFET) or top AlGaN layer (HEMT) to decrease the distance from the gate to the channel. This process is the primary way to affect threshold voltages of the device, and it can improve frequency performance.[140] Additionally, existing III-V technologies utilize ion etching to remove highly doped top layers, used for low ohmic contact resistivities, prior to Schottky metallization.[141] For these cases, the Schottky gate is deposited on top of the etched region, which may contain substantial crystalline damage depending on etch conditions. Typical etches are chosen to minimize such damage, but changes in Schottky properties have been observed for GaN.[138]

If barrier height is plotted versus metal workfunction for numerous Schottky metals on a semiconductor, the slope, $S = d\phi_B / d\phi_M$, should be unity, due to the Schottky relation ($\phi_B = \phi_M - \chi_S$,). In practice, values substantially less than one have been observed

in the cases of Si and GaAs (S~0.1 in each case).[142] Other semiconductors, such as ZnS, exhibit S values close to 1.0. Originally, a correlation was observed between the difference in electronegativity of the constituent atoms in binary semiconductors and the S index.[143] For low electronegativity differences low S values were observed, and for high differences S improved to near unity. Alternatively, this correlation can be made versus the heat of formation of the binary compound.[68] The interpretation of this correlation is to the degree of ionicity of the semiconductor.[143] Highly ionic compounds should have sufficiently high bond strengths as to exhibit less chemical reaction with the Schottky metals. By contrast, binary compounds with low electronegativity differences are covalent in nature, and more susceptible to interaction with the metals. This interaction results in a high degree of states throughout the bandgap at the metal-semiconductor interface, which tend to locate the Fermi position at the average energy of the states. In this way, the barrier heights of metals with high workfunctions are lower than expected due to the effect of the interface states locating the Fermi energy. For this reason, the S-indices should decrease with increasing density of interface states. For a very high density of states, S is very low, and the metal workfunctions are uncorrelated with barrier height. In this case, the Fermi level is said to be "pinned" at some value in the bandgap.

Even highly ionic compounds have been shown to exhibit imperfect interface S indexes. Notably, GaN has been shown to exhibit S values of 0.21,[144] 0.38,[145] and other values substantially less than one[146,147] for studies with various Schottky metals. For AlGaN with x=11%, a value of 0.44 was reported, though AlN is also ionic. Reasons for this include surface states formed from thin, insulating contamination layers, with the

states located at the metal-insulator interface.[148] Even for metals deposited on clean ionic semiconductor surfaces in vacuum, there can be states arising from multiple factors. These may include local changes to the metal workfunction and semiconductor affinity due to the structure of the interface and/or metal (e.g., epitaxial or polycrystalline), lack of atomic abruptness at the semiconductor interface due to vacancies, interstitials, or interdiffusion of atoms between the metal and semiconductor, and overlap of wavefunctions of electrons in the metal, which can produce a state in the bandgap of the semiconductor. These factors, combined with interface reactions, result in an effective density of states at the interface, D_S, affecting S. An estimate of D_S has been modeled from S as[149]

$$D_S = \frac{1-S}{S}\frac{\varepsilon_i}{q^2 t_i} \tag{7.1}$$

where ε_i and t_i are the permittivity and thickness of a thin (~10Å) interfacial layer. Using this estimate, $D_S \sim (1-S)/S * 10^{13}$ cm^{-2}eV^{-1}.

Most data for barrier heights versus metal workfunction in the nitride system involved GaN. Fewer reports exist for alloys. Figure 7.1(a) shows a plot of barrier height vs. metal workfunction for numerous literature reports of various metals on GaN. [146,147,150,151,152,153,154,155] Metals included Ti, Cu, Ag, Pt, Ni, Au, Pd, and W, and barrier heights were all extracted from I-V measurements. Here, an S value of 0.25 is determined from the compiled data. Figure 7.1(b) shows the same plot for alloys with mole fraction 10%[145,146,155,156,157,158] and 25%[150,155,157,158]. Similar metals were considered, and for the lower alloy concentration, another low S value was reported, although the data here exhibit higher scatter. A subset of the data shown in both figures,

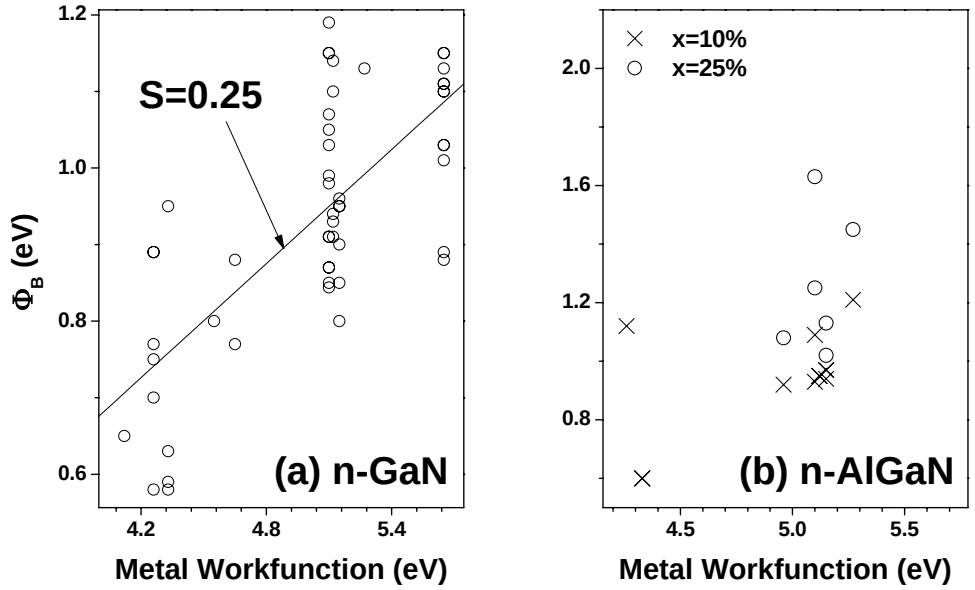

Figure 7.1. Compilation of barrier height data versus metal workfunction for chemically treated Schottky barriers on (a) GaN and (b) two Al mole fractions of AlGaN, from references given in the text. The slope of the fit line in pane (a) was determined by the author.

as published in Ref. 145, exhibits improved *S*-values of 0.38 and 0.44 for GaN and 11% AlGaN. From eqn. (5), the density of surface states, as-deposited on the chemically prepared surfaces, is calculated to be ~10^{13} $cm^{-2}eV^{-1}$ for all cases.[145]

The thermal stability of Schottky contacts is usually considered on a specific metal-semiconductor basis. For III-V compounds, trends have been observed correlating electronegativities with thermal stability. Generally, metals exhibiting small electronegativities exhibit thermally stable Schottky contacts. Metals with higher electronegativities tend to react with the semiconductor upon heating, including removing the group-III constituent into the metal and forming compounds with both the group-III and –V elements.[148] Depending on the electronic structure of the semiconductor, removal of these constituent atoms may alter doping in the vicinity of the contact and

change the current-voltage characteristics of the barrier. The salient detail is that apparent changes in barrier height upon thermal annealing may be manifestations of changes in current transport, and atomic depth profiling techniques may be used to help identify such issues. Additionally, such techniques may show compositional changes in the metal and/or semiconductor, which can additionally affect barrier heights.

The metal-specific nature of thermal stability of Schottky barriers is illustrated by considering a survey of recent literature. For example, barrier heights for Pt on GaN were shown to be stable through 400°C[159] and 500°C[160] before degradation occurred. Only after annealing for 30 minutes at 700°C were significant changes in surface morphology and evidence of intermixing observed. Similar thermal stability was noted on AlGaN, as characterized by barrier height decreases.[161] This stability arises due to the chemically inert nature of Pt, which precludes interface reactions until the highest temperature. Likewise, Au was shown to be reasonably stable from such interactions through high temperatures, and Au-GaN diodes exhibited good characteristics through 575°C.[162] More reactive metals may exhibit interface reactions at much lower temperatures, however. Pd on GaN showed evidence of such reactions, as noted from changes in barrier height, after only 300°C. Clear evidence of reactions between group-III atoms and the Schottky metal were noted for certain diodes subjected to high temperature annealing. Pd on AlGaN showed surface roughness increases and barrier height decreases around 500°C, as well as significant interface reactions for higher temperatures (>700°C).[43] Similarly, Ni on AlGaN exhibits stability through 1 hour at 500°C, but increases in surface roughness were also noted. Additionally, Ni interface reactions leading to Ga-depletion in the AlGaN were also noted for temperatures >700°C

in Ref. [163]. Other reactive metals, such as Ir, have shown minimal changes after short anneals >800°C. Further complications arise due to morphological changes of the metal on the semiconductor surface. For example, evidence of metal islanding has been observed for Ni and Pd annealed at 500 °C for 1 hour and for Pt annealed at 600 °C for 30 minutes.[164] From these results, it is apparent that the specific metal plays a large role in thermal stability even substantially below the metal melting point, due to interface reactions and morphological transformations. Moreover, the specific surface preparation may catalyze or inhibit certain reactions. The importance of characterizing multiple metals on a consistently prepared or processed surface is illustrated from these observations.

Due to wet etches being ineffective in nitrides, dry etches have been utilized. Usually, inductively-coupled plasma reactive-ion etching (ICP-RIE) is used in practice. In particular, there is interest in recessed-gate etching to affect the threshold voltages in MESFETs and HEMTs, which for the latter case is given by

$$V_T = \phi_B - \frac{qN_d}{2\varepsilon_S} t^2 - \frac{\Delta E_C}{q} \tag{7.2}$$

where t is the AlGaN layer thickness and ΔE_C is the conduction band discontinuity between the GaN and AlGaN, assumed fixed. Altering the thickness of the AlGaN layer can improve the frequency performance of the device by permitting shorter gate lengths[165] and shift the threshold voltage from typical values (-5V) to values >0V, which shows promise for enhancement mode (normally off) HEMT operation.[166] Additionally,

the recess etch allows for smaller gate lengths, while maintaining the aspect ratio of gate length to AlGaN thickness. Maintaining a small t/Lg ratio allows for high frequency HEMT performance by minimizing fringing field effects. After etching, the Schottky gate is deposited on top of the etched AlGaN.

In practice, the ICP-RIE etching process is carried out as follows. In a reactive ion etching chamber, the sample or wafer is placed on a RF-driven cathode plate (~10 MHz) with the chamber walls connected to the anode. A dc-bias connected to the sample plate forms a potential difference between the sample and the plasma. Typical etch species are Cl_2 and Cl compounds such as BCl_3. During plasma operation, the chamber is typically evacuated to ~50 mtorr, and power applied to the cathode is ~kW/m^2. The etching species are ionized in the high fields in the plasma, diffuse to the surface of the sample, undergo a chemical interaction with the semiconductor atoms which forms a volatile compound, then this compound desorbs from the surface. Etch products are continuously evacuated by vacuum pumping. Increased bias voltages between the wafer and plasma accelerate the etching species directly into the material, which enhances etching rates significantly. Typical biases are hundreds of volts, and surface damage is increased with ion energy.[167] Inductively coupled plasma (ICP) etching is an enhancement of the RIE technique. Here, high-density plasma is generated in the center of the chamber, near the wafer, by generation of a strong magnetic field using inductive RF coils on the exterior of the chamber. This field causes charged electrons to undergo circular trajectories, thus increasing their lifetime and probability of ionizing the etching gas. For this reason, high plasma densities are created near the center of the chamber and high etching rates are achieved with lower sample biases. In this way, surface damage

can be minimized while maintaining desired etching rates.[167,168] The combined technique is usually called ICP-RIE. Etch rates >1000Å/min. have been achieved on GaN[168] and alloys[169,170] without significant changes in surface stoichiometry and surface roughness.[168,170]

Etch damage can include the formation of deep levels in the bandgap, which act as trapping centers. Additionally, surface chemistry can be affected by preferential loss of constituent atoms in the lattice. In each case, the damage depths are expected to be ~100Å or more.[138] Etch damage has been shown to decrease band-edge radiative recombination through the creation of non-radiative traps in the material.[138,171] Studies of Schottky barrier formation on plasma-etched GaN and AlGaN have shown degradation in the barrier characteristics. Changes in I-V characteristics from rectifying to weakly so were shown for Pt diodes on n-GaN using hydrogen, nitrogen, argon, and chlorine/argon plasma schemes for 500W RIE-ICP plasmas. Similar changes were observed for Ni-GaN diodes, even with relatively low dc bias voltages (~50V) using chlorine/argon etching. Large reductions in the I-V barrier height were observed for Ni diodes on 20% AlGaN (from ~0.8 to ~0.5eV) with a hydrogen plasma[172] and 15% AlGaN.[173] For all cases, the increase of sample bias resulted in more degradation, due to the increased energy of the ions. Furthermore, changes in barrier height were shown to depend on etch time, indicating a cumulative effect of etch damage.[138,173] One effect of etching noted was the creation of nitrogen vacancies[174], which acted to increase thermionic-field emission and degrade the apparent barrier height. Additonally, evidence of dopant passivation has been observed for plasma etching, with hydrogen passivating Si doping.[138]

Comparative studies of thermal stabilities of plasma etched and un-etched Pt diodes on GaN were performed in Ref. 138. As before, the etched samples exhibited significant I-V degradation after nitrogen RIE-ICP plasma etching. The un-etched control diode showed thermal stability through 700°C, but the diodes with pre-deposition plasma etching showed continued degradation with anneals at lower temperatures (through 500°C). It was postulated that changes in surface roughness due to etching may affect interaction between Pt and GaN. The authors then tried anneals after plasma etching, but prior to Schottky deposition for Pt diodes. I-V characteristics could be improved towards un-etched characteristics, but not completely, and only after high annealing temperatures (750°C for 30 sec.). Moreover, the next higher temperature anneal attempted (850°C) resulted in further degradation, implying a decomposition effect in the GaN, possibly enhanced by the plasma-induced surface changes.

The salient features from these studies are: (1) RIE-ICP etching has an effect on the resulting Schottky barrier, (2) subsequent annealing does not necessarily fix etch damage, (3) the plasma etch may increase susceptibility to subsequent thermal stressing, and (4) annealing after the etch but before the contact is deposited may or may not restore expected barrier properties to the wet-etched case. There are few reports directly addressing these issues with regards to the Schottky barrier of different metals. In particular, annealing before the Schottky deposition has been performed for HEMT technologies,[138,175] but not in the context of a controlled Schottky barrier study using fundamental characterization methods. Subsequent post-deposition anneals are also expected to depend highly on the metal used, as seen from the variance of thermal stability of different metals.

7.2 Growth details

Thick (1 μm) AlGaN was provided from a commercial vendor in October 2004. The samples were from a 2" wafer grown by molecular beam epitaxy (MBE) on a sapphire (0001) substrate with an AlN nucleation layer prior to AlGaN growth, resulting in the Ga-face crystal orientation, as in the case of AlGaN-GaN HEMT structures. The AlGaN was intentionally Si doped with [Si]~$2x10^{17}$ cm^{-3}. The Al mole fraction was determined by methods discussed in Section 7.3 (target x~0.30). The sapphire substrate was metallized with tungsten prior to growth to promote uniform heat distribution during growth. The cation sources were tri-methyl aluminum and tri-methyl gallium, and the nitrogen was generated from a plasma source. The wafer was quartered with a diamond saw at the Air Force Research Laboratory Sensors Directorate at Wright-Patterson Air Force Base, OH (AFRL). Prior to deposition of diodes, cathodoluminescence was performed to ensure spatial uniformity of all pieces, in terms of mole fraction and optical emission structure. The location and maximum size of the pieces used in this study were determined from such measurements. Three ~12mm x 12mm squares were each cut from near the center of the wafer. Three surface treatments were prescribed, as outlined below.

7.3 Characterization of AlGaN uniformity and mole fraction

To determine material uniformity, cathodoluminescence spectroscopy was performed on each quarter. Uniformity is important to ensure that any differences in Schottky barrier performance for the three processing conditions are due to the process, and not the as-grown material. Initial scans were performed near the right angle of the

quarter (i.e., the center of the wafer, as-grown), and scans were taken every ~2mm from this point outward, in each direction. In this way, the maximum usable size of each quarter was determined. Here, usable size is defined as the largest size piece for which the luminescence properties such as peak shape, height, and position were similar. For all quarters, this size was determined as approximately 12x12 mm squares, with two of the square sides defined by the cut lines from quartering. A representative cathodoluminescence scan is shown in Figure 7.2. In this figure, the other three scans are from previous cathodoluminescence work performed in the author's lab, and published in Refs. 32 and 176. The AlGaN studied in those reports was also of the thick film variety (i.e., relaxed), grown by MBE, and Si doped. The aluminum mole fraction data indicated in the figure was determined by high-resolution x-ray diffraction. In Ref. 176, the multiple peak structure observed in many of the spectra (e.g., x~0.25 case) was attributed to a compositional phase separation across the surface of the alloys. Long-period (~10 monolayer) compositional ordering was also reported in the study, with that effect being predominant for higher mole fractions (x>0.5).

The dotted curves indicated in Figure 7.2 result from Gaussian curve fits on the luminescence spectra for the present work. The resulting peaks are always observed and vary little with position across the 12x12 mm squares. The determination of mole fraction from the cathodoluminescence data is shown in Figure 7.3, with the closed circles from Ref. 176 and the open circles representing the curve fits in Figure 7.2. From the data in Ref. 176, the open circles correspond to mole fractions of approximately 0.40, with a difference of approximately 0.03 between the two peaks. A more accurate characterization of mole fraction and compositional effects was determined using an

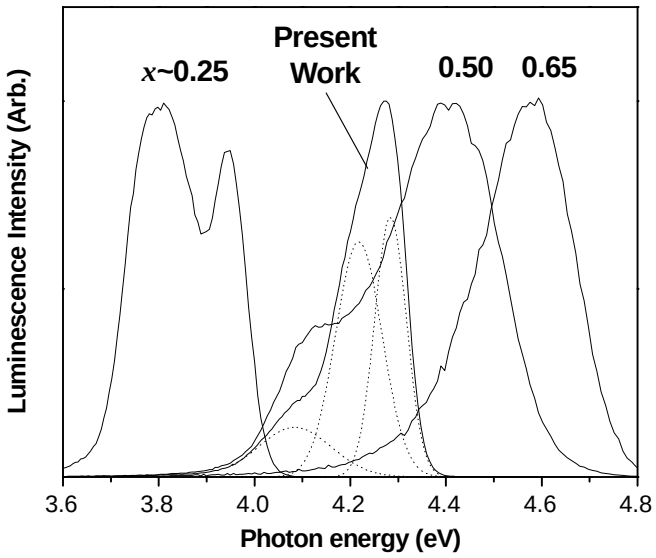

Figure 7.2. Cathodoluminescence data for the present AlGaN wafer, plotted with data from Ref. 176. The dotted curves are typical curve fits for all samples and locations across each piece.

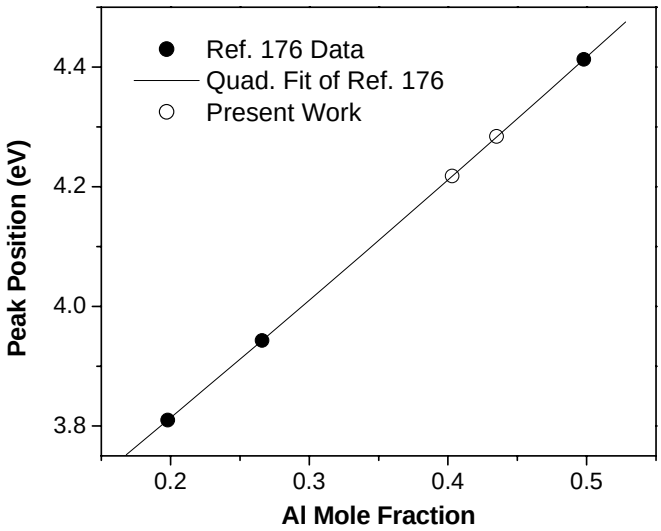

Figure 7.3. Cathodoluminescence peak position versus mole fraction for the data in Ref 176 (closed circles) and the author's work (open circles). Two AlGaN phases are inferred, with mole fraction ~0.40.

x-ray diffractometer. The scans were taken on a Bede D1 diffractometer in the Electronic Materials and Device Laboratory at Ohio State University (courtesy of Prof. S. A. Ringel). Double- and triple-axis $\omega/2\theta$ scans are shown in Figure 7.4 for the data in Ref. 176 and the present wafer. In the $\omega/2\theta$ configuration, the x-ray source and diffracted x-ray detector are moved together, such that the angle between specimen normal and each component is constant. In this way, diffraction peaks corresponding to the Bragg condition are observed as the angles are swept through a prescribed range. The triple-axis configuration adds additional resolution to the scan, and that mode is necessary here due to the small angular separation between the diffracted peaks. In Figure 7.4, the triple-axis scan for the present work (solid curve) gives clear evidence for (0002) AlGaN maxima with two phases, as with the x~0.25 and x~0.50 cases taken from Ref. 176. For the present wafer, the separation between phases is considerably smaller than the data from Ref. 176. The inset of Figure 7.4 shows the Gaussian fitting result of the triple-axis scan. The peak maximum angles noted on the inset correspond to mole fractions of 0.427 and 0.443, as estimated from the Ref. 176 data plotted in Figure 7.5. In Figure 7.5, the phases of the present study are noted on the quadratic fit (open circles). Figure 7.6 shows double-axis grazing-incidence x-ray diffraction data, with the Bragg peaks corresponding to diffraction from long period ordering effects. For the present study, such effects are noted as present, but small, when compared with the higher mole fraction samples from Ref. 176, also plotted in the figure. The weak nature of this peak combined with the strong double peak structure noted in Figure 7.4 confirms that phase separation is the dominant compositional effect observed in this wafer, which is in agreement with previous studies on lower mole fraction material.

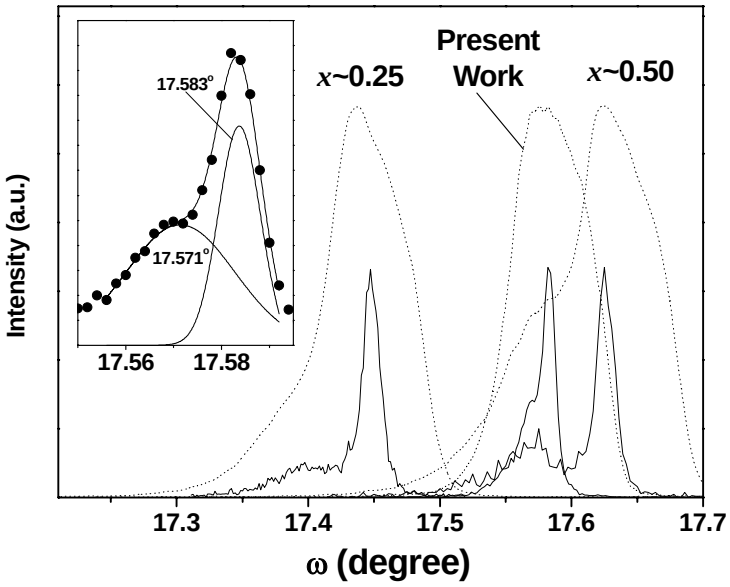

Figure 7.4. Double-axis (dotted) and triple-axis (solid) x-ray diffraction data for the samples in Ref. 176 and the present AlGaN wafer. Inset: Curve fitting results for the triple-axis of the present work.

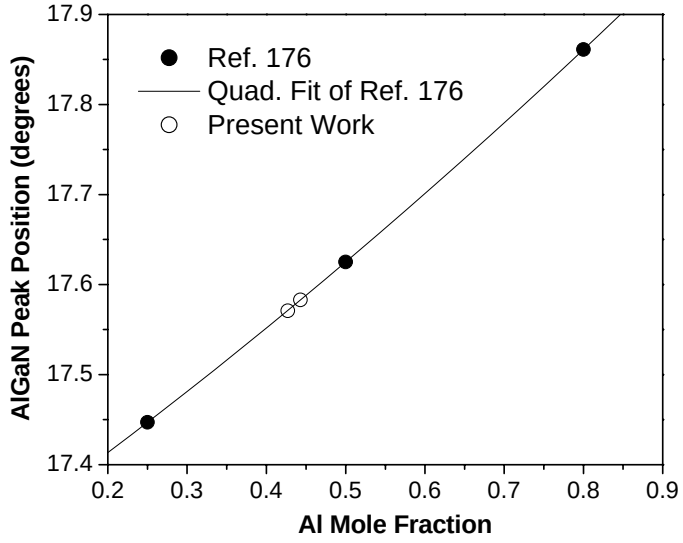

Figure 7.5. X-ray diffraction peak position from curve fitting versus mole fraction for the data in Ref. 176 (closed circles) and the present work (open circles). Mole fractions of 0.427 and 0.443 are inferred for the two main phases of the present wafer.

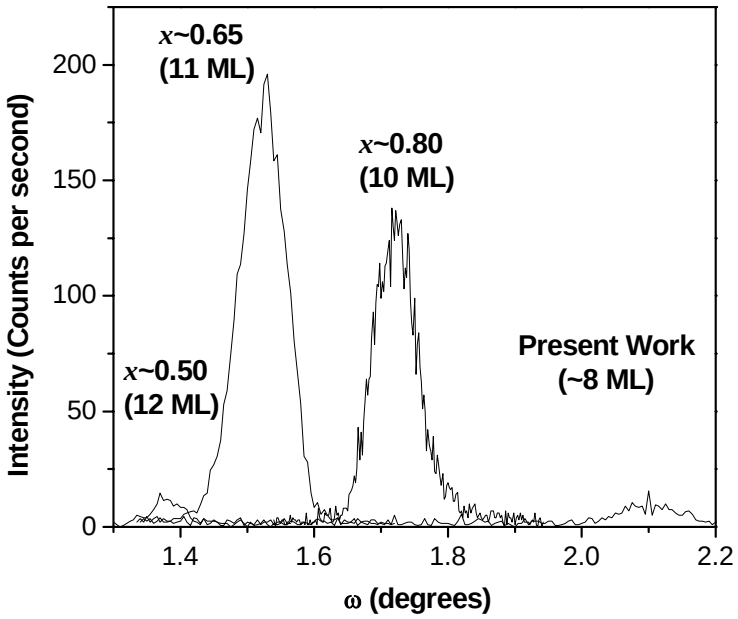

Figure 7.6. Grazing-incidence triple-axis x-ray diffraction data for three samples in Ref. 176 and the present work. From the peak strength, ordering is shown to be present, but a small effect in the present wafer.

The mole fractions are in general agreement with the cathodoluminescence data in Figure 7.2. These mole fractions are much higher than the growth target (x~0.25), and mole fractions above ~0.45 exhibit strong decreases in conductivity, due to the transition of oxygen from a shallow donor to a D-X-like state.[177] On the other hand, few Schottky barrier reports exist for such high mole fractions, so any results obtained here add to the understanding of the effects of increased aluminum content on barrier heights. Finally, although phase separation is undesirable for barrier height studies, the difference in composition between phases measured here by x-ray diffraction is sufficiently small to be safely ignored. For example, the difference in electron affinities between GaN (χ~3.2 eV) and AlN (χ~1.9 eV) is 1.3 eV.[178,179] Assuming the Schottky relation $\phi_B = \phi_M - \chi_S$ is

followed, a difference of 1.6% in mole fraction, as extracted from the x-ray data, should result in a difference in barrier height of ~20 meV, which is within the uncertainty of typical I-V scans and small compared with the absolute barrier heights expected (~1.5 eV). For subsequent analysis, the distinct phases are assumed to act as one, with the mole fraction taken as an equal-area average of the two compositions, or 43.5%.

7.4 Fabrication of diodes

For all samples, a standard clean was performed, consisting of acetone, methanol, and a de-ionized (DI) water rinse. Additionally, the backside tungsten metallization was chemically etched from the sapphire using a $HF:HNO_3:H_20$ (1:2:7) etch to facilitate subsequent optical measurements. Shipley 1818 photoresist was painted by hand onto the majority of the sample, except for two thin strips near opposing edges, which defined the ohmic regions of the sample. After a softbake (60 sec at 95°C) the resist-coated sample was etched with 1:1 HCl:DI water for 30 sec, then rinsed for 5 minutes in DI, followed by a nitrogen blow-dry. For all samples, ohmic contacts (Ti/Al/Ti/Au) were deposited by e-beam deposition.

At this stage, the processing steps were different for each sample, according to the prescribed surface treatment. For the HCl and ICP samples, a standard ohmic rapid thermal anneal (RTA) was performed at 850°C for 30 sec. Photoresist was then painted over the existing ohmic contacts for the HCL sample, and a 1:1 HCl:DI water etch was performed for 30 sec. The sample was rinsed in DI water for 5 minutes then blown dry with nitrogen. The ICP and ICP-RTA samples were loaded in the ICP-RIE etching machine, with dummy pieces of Si covering the existing ohmic contacts, as a mask. A 13

minute etch was performed, removing 300Å of AlGaN, as verified by step profilometry on a calibration piece of AlGaN run previously. The RTA procedure described previously was then performed on the ICP-RIE piece, thereby doubling as the ohmic anneal and RTA damage anneal. The process steps and ordering is summarized for all samples in Figure 7.7. The ICP-RIE parameters were: dc bias=53V, 10 standard cubic centimeters per minute (SCCM) BCl_3 + 1.2 SCCM Ar, chamber pressure=4 mTorr, 5 W RIE and 250 W ICP power.

All three samples were affixed to clean dummy Si pieces using low vapor pressure vacuum compatible tape. Shadow masks were then affixed on top of the sample using the same tape. These masks defined the Schottky diodes and consisted of an x-y grid of 400 μm diameter holes spaced 500 μm apart in each dimension. The masks were made from 18-8 stainless steel, and prior to usage they were decontaminated by a standard organic clean, DI water rinse, nitrogen blow dry, and low temperature hotplate bakeout. The samples and affixed masks were then loaded into the electron beam evaporator. In practice, both the wet etch and ICP-RIE etches were performed at approximately the same time, such that the air exposure times prior to vacuum pumpdown were similar for each piece. During any dwell time (i.e., between processing and vacuum loading) all pieces were stored in a sealed nitrogen box.

For each metal deposited, a single row of the mask holes were uncovered, with every other row covered. For subsequent metals, the procedure was repeated with the adjacent row uncovered. In this way, nine different Schottky metals were deposited in nine adjacent rows. A representative picture of the geometry of the diodes is shown in Figure 7.8. Mask-adjustment time between different metals (i.e., time out of vacuum)

was <5 minutes for each metal. The Schottky metals were (in order of deposition) gold, nickel, platinum, molybdenum, aluminum, tantalum, iridium, germanium, and palladium. These metals were chosen due to their common application in nitrides (e.g., Ni and Ir) and for the range of metal workfunctions (Mo=4.6 eV to Pt=5.65 eV). The target thickness for all metals was 300Å, which was verified for all metals to within 10% by surface profilometry scans post-deposition, using a Dektak. After all evaporations were completed, a final acetone-methanol-deionized water rinse was performed to remove any tape residue or other contaminants. For each metal and each process condition, twenty-three diodes were usable. By inspection, all metals exhibited clean, uniform metallizations except iridium on the ICP etch sample. These diodes exhibited poor adhesion and lifted off the AlGaN surface during the final organic clean. The iridium diodes on the other two pieces adhered to the surface well. All subsequent I-V data is absent the ICP etch iridium case.

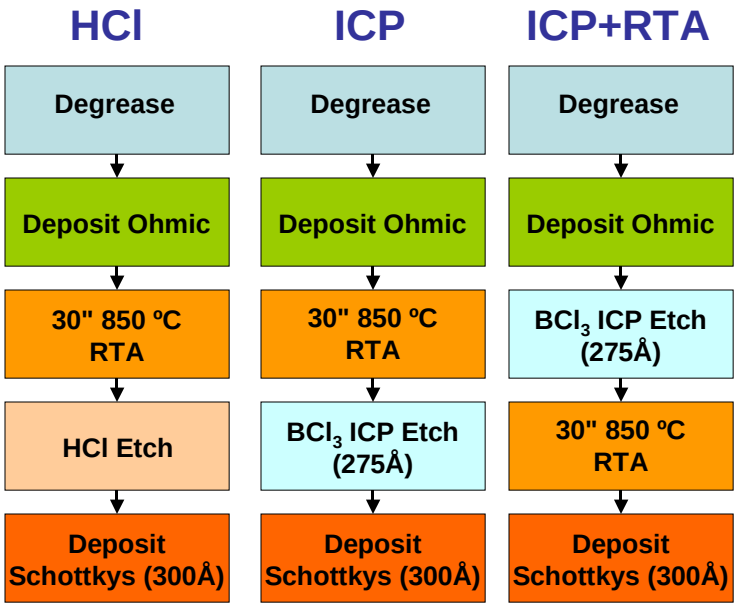

Figure 7.7. Process flowchart for the three AlGaN surface treatments.

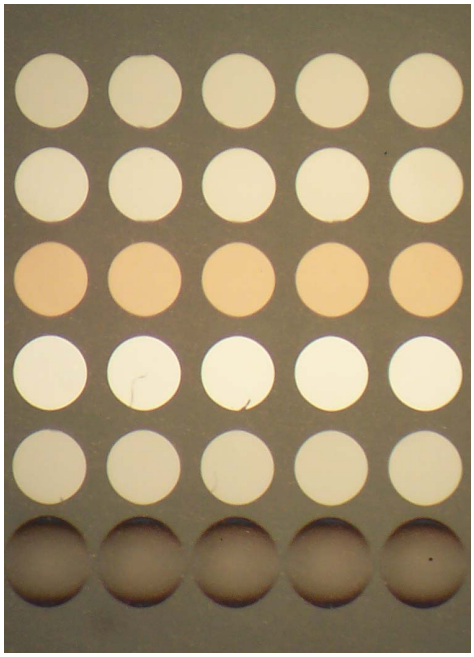

Figure 7.8. Representative photograph of the shadow mask configuration used in this study. Each row is a different Schottky metal. The diode diameter is 400mm and the distance between diode centers is 500mm in each direction.

7.5 Initial diode current-voltage characterization

Current-voltage sweeps were first taken on each piece between the two opposing ohmic contacts using a Hewlett-Packard 4145B semiconductor parameter analyzer. The sweeps exhibited highly linear behavior (correlation coefficient, r=1.0 in linear fits), with typical values of resistance of 88,000 Ω (55,000 Ω/square and 5.9×10^5 Ω-mm). Since material resistivity is the dominant contribution to resistance here, ohmic contact resistance is difficult to quantify without a special structure (e.g., a transmission line geometry). Values of annealed contacts on AlGaN are expected to be <1 Ω-mm, and the contacts are demonstrated to be sufficiently ohmic from the high linearity of the I-V sweeps.

Using the same instrument, current-voltage sweeps of the Schottky contacts were addressed next. Pt was chosen to investigate the variance in current-voltage properties across each piece, since this metal is expected to exhibit low reactivity with AlGaN and a low oxidation rate, implying that extended studies could be performed with minimal concern for time effects over weeks or longer periods. Figure 7.9 shows the Pt I-V curves for all diodes on each piece for voltages between –10 and 2V. All diodes are shown together to illustrate the qualitative differences between the three etch cases. In pane (a), the diodes for the HCl case exhibit appreciable scatter in both biases, particularly in the forward case. The turn on voltage for large forward currents varies between ~0.5 V and ~1.5 V. For the ICP etch case in pane (b), all I-V curves exhibit much more similarity in both reverse in forward bias. The tight grouping for all curves indicates the bulk and surface properties determining the Schottky barrier transport have been made much more uniform after the etching. For the ICP etch + RTA case in pane

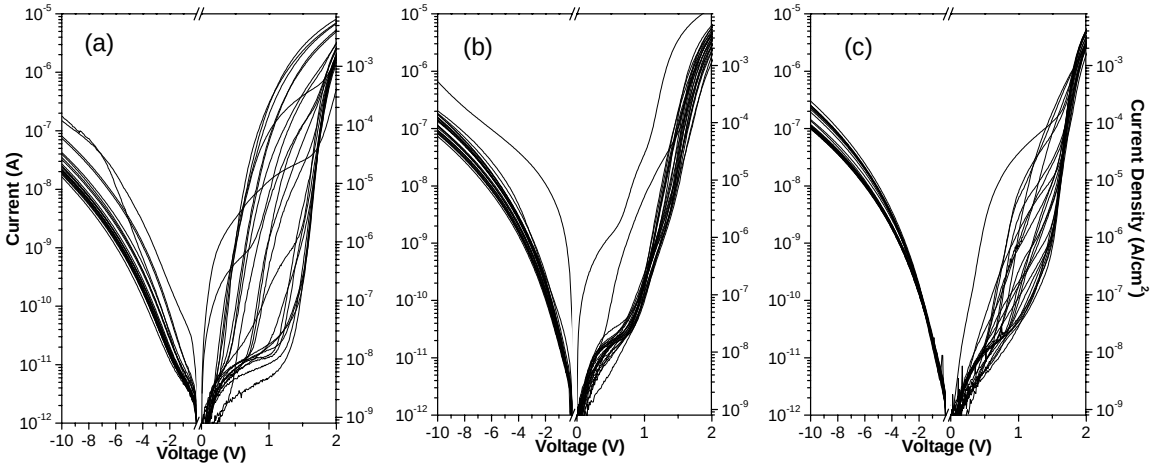

Figure 7.9. All I-V data for the 23 Pt diodes fabricated on (a) the HCl treated surface, (b) the ICP treated surface, and (c) the ICP treatment + RTA step prior to metallization.

(c), an intermediate case is noted. The reverse and forward currents are grouped more tightly than in the HCl case, but the scatter exceeds that of the ICP case. Evidently, to some extent the annealing process restores the changes to the AlGaN responsible for the I-V behavior in the ICP case. The material properties responsible for the I-V behavior will be discussed more thoroughly in Chapter 8, where micro-cathodoluminescence measurements are used to correlate diode electrical properties.

For the forward bias case, Most I-V curves exhibit similar properties in the low (<0.5 V) and high (>2 V) voltage ranges. These regions are expected to be dominated by parallel and series resistances, respectively. The former case can arise from surface conductivity from the diode to the ohmic contact, conduction through the probe wires, conduction from the probe to the station ground, or the internal resistance of the probing instrument. The currents are of the ohmic form $i = V_{app} / R_P$ and should be small due to the large value of resistance. Indeed, for the diodes tested here, extracted values of R_p are $\sim 10^{11}$ Ω. This effect is only seen for larger barrier heights, where the diode turn on

voltage is large. For the higher voltages, serial resistance effects are important. In this bias regime, currents become sufficiently high as to cause a voltage drop across the material from the diode to the ohmic contact. This results in a decrease of the voltage across the actual Schottky diode, and the effect is to decrease the currents to an artificially low value. In practice, the curves appear to "roll over" as seen in curves in Figure 7.9. As noted in Chapter 6, series resistance values can be extracted from the slope of $I^*(\partial I/\partial V)^{-1}$ vs. I, as described in Ref. 180. For the diodes tested here, typical values of R_s are ~50 kΩ, which is a reasonable value given the measured sheet resistance values.

Figure 7.10 illustrates these regions of the I-V curves for three platinum diodes on the HCl sample. The region labeled "R.O.I." represents the region of interest for extraction of barrier heights, including the discrimination multiple barriers, if present. In practice, the presence of parallel resistance has a minimal effect on barrier extraction for these diodes. The series resistance terms, however, can interfere significantly with accurate barrier extraction. As noted in subsequent discussion, series resistance effects are accounted for if necessary.

Three cases are shown in Figure 7.10: a low barrier (left-most curve), a high barrier (right-most curve), and an intermediate case exhibiting evidence of two barriers (middle curve). In the absence of multiple barrier effect, it was noted that most I-V curves were grouped near the high barrier case. This trend was noted for numerous metals and processing conditions, but the trend was strongest in the HCl etch and ICP etch + RTA cases. This can be noted by inspection of Figure 7.9 panes (a) and (c). This high barrier is subsequently called the "primary barrier", and other contributions to the

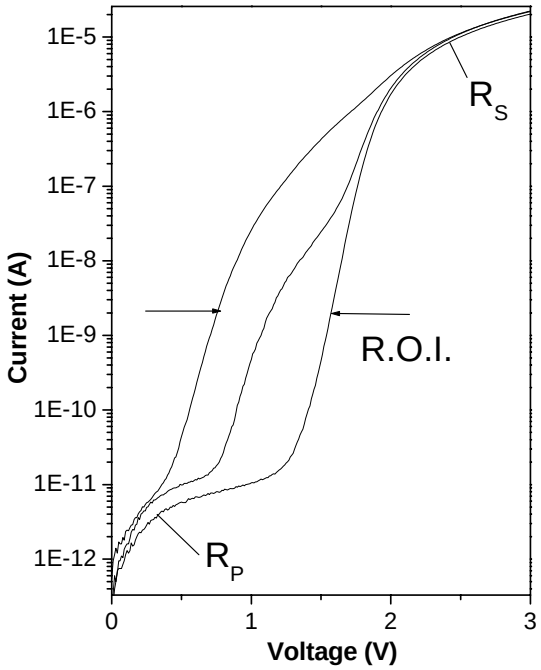

Figure 7.10. Illustration of variance in the forward I-V curves, including regions of parallel resistance, series resistance, and the region of interest (R.O.I.) for barrier analysis.

diode current are regarded as additional transport mechanisms occurring in parallel with this primary mechanism.

For each metal and processing condition, several curves prominently exhibiting the primary barrier, such as the right-most curve in Figure 7.10, were corrected for series resistance, averaged, and plotted in Figure 7.11. In all panes of Figure 7.11, the legends have been arranged in order of metal workfunction, from the lowest (Ta) to the highest (Pt). If the Schottky relation is followed for each case, the turn on voltages should increase with increasing workfunction. In other words, the curves should be offset from left to right with the lowest workfunction metal to the left. In Figure 7.11(a), the HCl curves are shown. The curves show a large variation in barrier height, ideality, and

shape. Little correlation with workfunction is noted. In Figure 7.11(b), the ICP etched diodes show similar curves for all metals, as was the case with the Pt diodes on the ICP etched surface. Al is the only prominent exception, exhibiting a poor ideality. Due to the close grouping, the relation with workfunction is not observed. In Figure 7.11(c), the ICP etch plus RTA treated surface results in better behaved diodes compared with the previous cases. All ideality factors are similar, and a general trend with workfunction is seen. That is, the lower workfunction metals (e.g., Al, Ta, and Mo) exhibit the lowest turn on voltage, and the highest workfunction metals (e.g., Ir, Pt) exhibit the highest turn on. The intermediate metals (Au, Pd, and Ni) have similar workfunctions, and these curves are located between the extreme cases. A clear dependence of barrier height on workfunction is observed.

Barrier heights were extracted from the Figure 7.11 curves using thermionic fits. The results of all fits are shown in Figure 7.12, in the form of barrier height vs. workfunction. The metal workfunction values are for the polycrystalline metal phases given in Ref. 181. Here, the HCl barrier heights exhibit a weak correlation with workfunction, whereas the two plasma-etched cases show a clearer correspondence. For the ICP-etched sample, the barrier heights are similar, as expected from pane (b) in Figure 7.11. The slope of the fit line is ~0.05, corresponding to a density of interface states of ~1.9×10^{14} $cm^{-2}eV^{-1}$, according to Eqn. (5). Similarly, the RTA treated plasma-etched sample exhibits a slope of ~0.30 on the plot, corresponding to a state density of ~2.1×10^{13} $cm^{-2}eV^{-1}$. Evidently, the density of resulting metal-semiconductor interface states is reduced by an order of magnitude by the addition of a RTA step after the plasma etch, but prior to metalization. Furthermore, the correlation of barrier height with metal

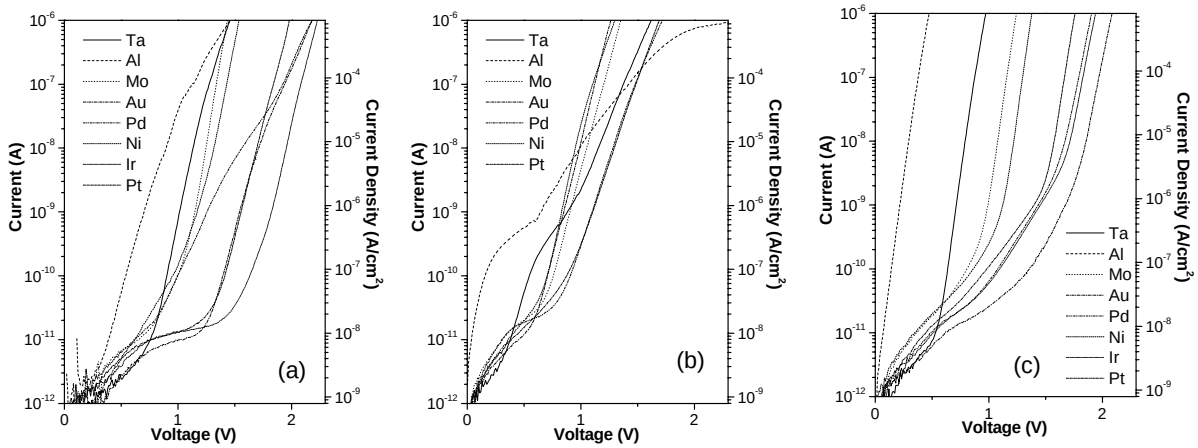

Figure 7.11. Average of I-V curves for several diodes prominently exhibiting the primary barrier for (a) the HCl etched case, (b) the ICP etched case, and (c) the ICP etch followed by an RTA process. The I-V curves have been corrected for series resistance.

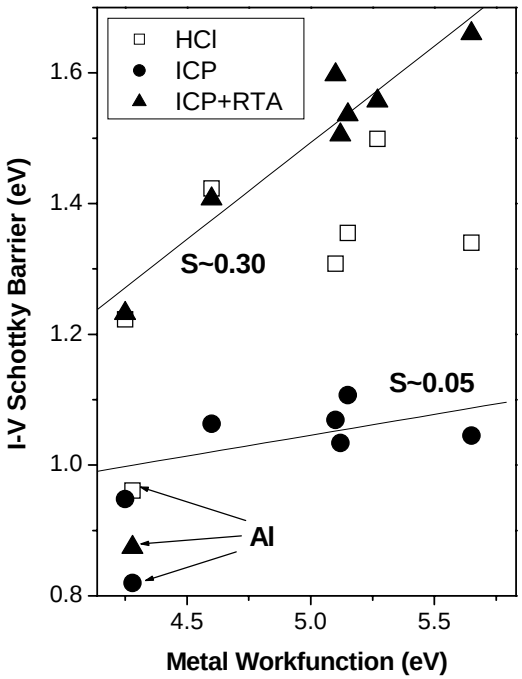

Figure 7.12. Plot of barrier heights extracted from the I-V curves in Figure 7.11 versus metal workfunction, plotted for all etch cases. Ir is absent from the ICP case due to poor adhesion after metallization.

workfunction is stronger for the RTA case than for the HCl etch, which does not exhibit a good linear fit. The slope of ~0.30 is the highest value reported to date for an aluminum mole fraction >0.4. The aluminum data points are excluded from the fits due to the barriers heights being anomalous, presumably from room temperature oxidation effects. Similar effects have been noted for aluminum contacts on ZnO without a protective overlayer (e.g., gold).[182] A summary of all thermionic fits is given in Table 7.1 for all metals and surface treatments.

Metal	ϕ_M (eV)	HCl		ICP		ICP + RTA	
		ϕ_B	n	ϕ_B	n	ϕ_B	n
Ta	4.25	1.22	2.00	0.95	3.97	1.23	1.38
Al	4.28	0.96	2.88	0.82	6.12	0.87	1.37
Mo	4.60	1.42	1.63	1.06	2.59	1.41	1.44
Au	5.10	1.31	2.61	1.07	2.40	1.60	1.98
Pd	5.12	--	--	1.03	3.42	1.51	1.98
Ni	5.15	1.36	1.89	1.11	2.12	1.54	1.39
Ir	5.27	1.50	2.32	--	--	1.56	1.91
Pt	5.65	1.34	2.49	1.05	3.34	1.66	1.57

Table 7.1. Summary of barrier heights and ideality factors of the primary barriers, for all metals and all processing conditions. The Pd fits in the HCl case were poor quality, and are excluded here. The Ir diodes lifted off the ICP prepared piece prior to testing. The workfunction values are the polycrystalline values given in Ref. 181.

7.6 Secondary barrier effects

The data are now examined in greater detail to examine the existence of barriers in addition to the primary barrier characterized in Section 7.3. Figure 7.13 shows the variance in forward I-V characteristics for molybdenum, nickel, and platinum on the HCl etched surface. For each metal, the turn on voltage for the left-most curves occurs at

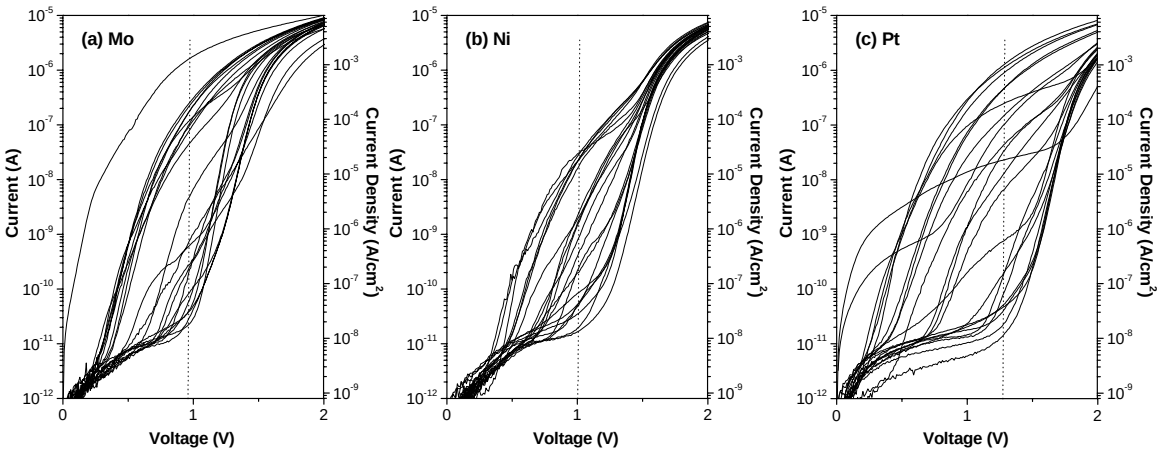

Figure 7.13. All forward I-V curves of the HCl etched sample for (a) Mo, (b), Ni, and (c) Pt.

approximately the same value of ~0.3V, whereas the right-most curves are constrained by the primary barrier discussed previously. Furthermore, the large variance previously shown in the I-V curves for platinum is also present for the other two metals. To ascertain a rough estimate of the spatial dependence of this variance for all metals, the currents for all metals are compiled at the turn-on voltage of the diodes only exhibiting the primary barrier. At this voltage, the currents for all ~23 diodes exhibit differences of orders of magnitude, so there is a high resolution of changes in current. Moreover, by choosing the turn-on on a metal-specific basis, the shifts in the curves due to changes in the primary barrier can be managed easily. Figure 7.14 shows the result of applying this method to all Mo, Ni, and Pt at 0.95, 1.00, and 1.30V, respectively. In this figure, there is a clear indication that the variation in forward current is a general trend, rather than a metal-specific one, given the high correlation between all three metals as a function of position across the HCl etched piece. This further suggests that defects in the material, rather than metal-specific interface reactions, control the forward current properties of the as-deposited diodes. This topic will be addressed in detail in Chapter 8.

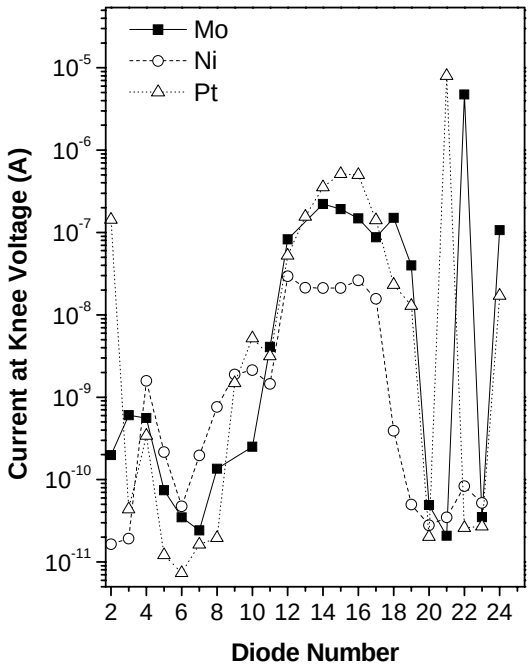

Figure 7.14. Summary of forward I-V currents at the turn on voltages of figure 8.12 for the Mo, Ni, and Pt diodes. The turn on voltages were 0.95, 1.00, and 1.30V, respectively.

Both ICP-etched pieces also exhibit transport properties that are similar regardless of metal. For example, all I-V curves of the Mo and Ni diodes are tightly distributed, as was the case in Figure 7.9(b) for Pt. Likewise, the ICP etched plus RTA annealed surface produced Ni and Mo diodes that were intermediate to the HCl and ICP cases, with the forward I-V curves exhibiting similar trends with position. Two metals in particular, Mo and Pt, were chosen for multiple barrier I-V analysis. These two metals encompass a large range in workfunction and generally exhibited I-V curves of sufficient quality to fit multiple barrier heights. The fits assumed multiple barriers in parallel according to

$$I = \sum A_i A_i^* T^2 \exp(q\phi_{Bi}/kT)\left(\exp(qV/kT) - 1\right) \tag{7.3}$$

with $A_i^* = A^*$ for all values of i. For all diodes, two components were sufficient. Typical series resistance values were ~50 kΩ and ~5MΩ for the primary barrier and secondary component, respectively. Based on this, the ratio of areas between the two regions should be approximately 100 (to first order), so that the area of primary barrier is approximated as the physical area of the diode, and the area of the second barrier is chosen as 1% of the physical area. In practice, even large uncertainties in diode area do not significantly affect barrier results from thermionic fits, so the chosen estimate is reasonable. For example, changing the area to 0.1% of the physical area only shifts barrier heights by ~50 meV.

Figures 7.15 and 7.16 show the results of the multiple barrier fitting on the Mo and Pt diodes, respectively, for all etching conditions. For some diodes, one barrier was dominant, and this is reflected in the data (e.g., HCl etch case, diodes 12-18). In other cases, two barriers were clearly resolved (e.g., ICP+RTA sample, diodes 2-20). In general, accurate fits were difficult in the "transitional" regions between one and two barriers, such as in the vicinity of diode 12 in the HCl case in each figure. In such regions, apparent changes in barrier height for the primary barrier should be taken with caution. Fitting issues aside, the trends for one versus two barriers are the same for both metals as a function of position, for all etching cases. This is similar to the result shown in Figure 7.15, suggesting that trends in barrier height are related more to material variation than the intimate nature of the contact, which is expected to be metal-specific. Moreover, the second barrier fits to the same approximate value (~1 eV), regardless of whether the diode metal was Mo or Pt, suggesting this barrier is also independent of

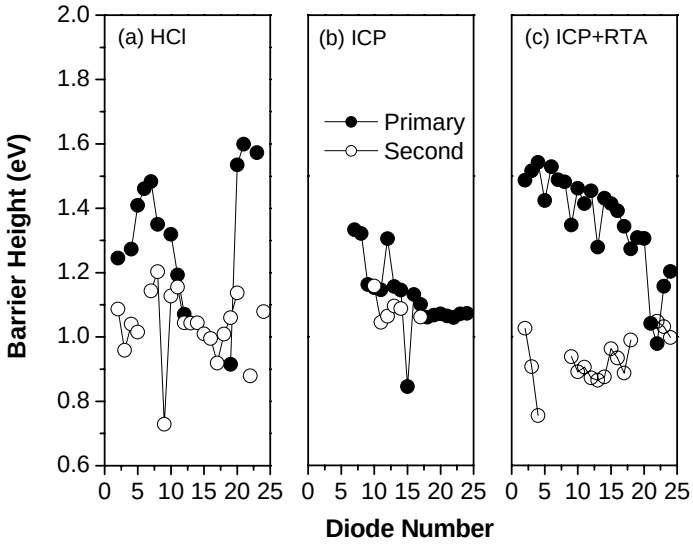

Figure 7.15. Summary of primary and secondary barrier fits for Mo diodes on (a) the HCl case, (b) the ICP case, and (c) the ICP + RTA case.

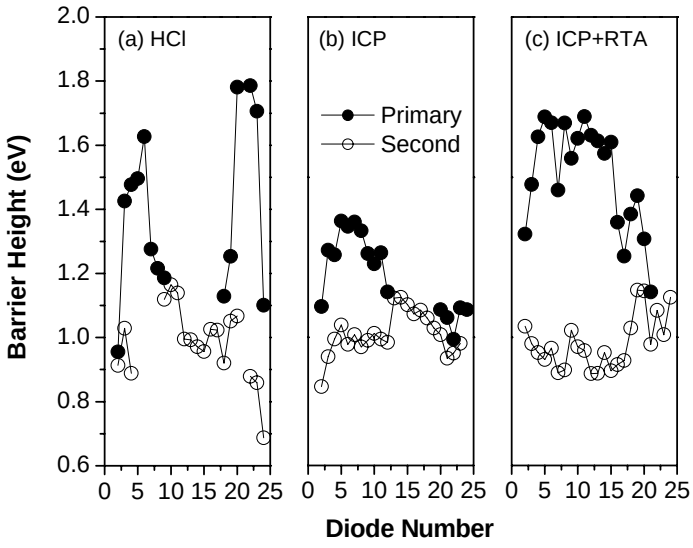

Figure 7.16. Summary of primary and secondary barrier fits for Pt diodes on (a) the HCl case, (b) the ICP case, and (c) the ICP + RTA case.

workfunction. (The primary barrier *is* dependent on workfunction, according to the previously established relation of barrier height to workfunction, shown in Figure 7.12.)

7.7 Reverse currents versus metal and processing condition

A compilation of reverse currents at –5V is shown in Figure 7.17 for all metals and processing conditions. These data were complied several weeks after the diodes had been fabricated, and by this time the Al and Ta contacts had degraded and exhibited very low currents for both reverse and forward sweeps ($<10^{-11}$ A), presumably from oxidation effects during air exposure. These metals are excluded from analysis, although Ta reverse bias curves of select diodes taken shortly after fabrication exhibited similar currents to the other metals shown in the figure. In Figure 7.17, all metals exhibit roughly similar trends in current with position, again suggesting a common mechanism in the material for controlling the reverse currents. It is also apparent from the figure that the trends in reverse current do not correlate with the forward currents (e.g., Figure 7.14), nor with the extracted barrier heights (e.g., Figures 7.15 and 7.16). This suggests the material properties controlling the reverse currents and secondary barrier effects are likely different. The important trend for all metals is the increase in reverse current for both ICP cases, as compared with the HCl etched surface. This degradation in current is approximately an order of magnitude, and the addition of the RTA step does not restore the current densities, for as-deposited diodes. The densities are still relatively low, however, as literature reports give current densities of 10^{-6} A/cm^2 for GaN and up to 1mA/cm^2 for AlGaN alloys with mole fraction ~0.25.[183,184,185,186]

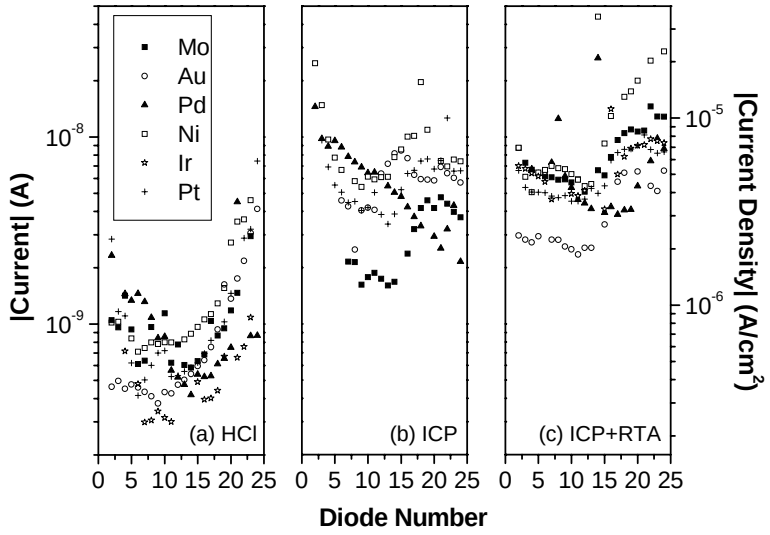

Figure 7.17. Summary of all reverse currents versus metal for (a) the HCl case, (b) the ICP case, and (c) the ICP + RTA case. Ir is absent from case (b) due to poor adhesion after metallization.

A statistical analysis of the reverse currents is given in Figure 7.18. Here, the individual datum are the average values for each metal and processing condition, and the error bars represent the standard deviation. The metals are arranged left to right in order of increasing workfunction. The lack of decrease in currents from left to right for all processing cases reinforces the premise that the reverse currents are independent of workfunction. Additionally, the average currents for the ICP etch and ICP etch+RTA cases are similar for most metals, with Mo being one exception (as noted previously, the Ir diodes did not adhere to the ICP piece, so these data are absent). In general, the annealing of pinning defects with the RTA process, which was shown to reduce interface defect density by an order of magnitude and improve the slope of the primary barrier vs. workfunction plot, does not affect the reverse currents the same way. This suggests different physical mechanisms for the reverse and forward transport processes. Such

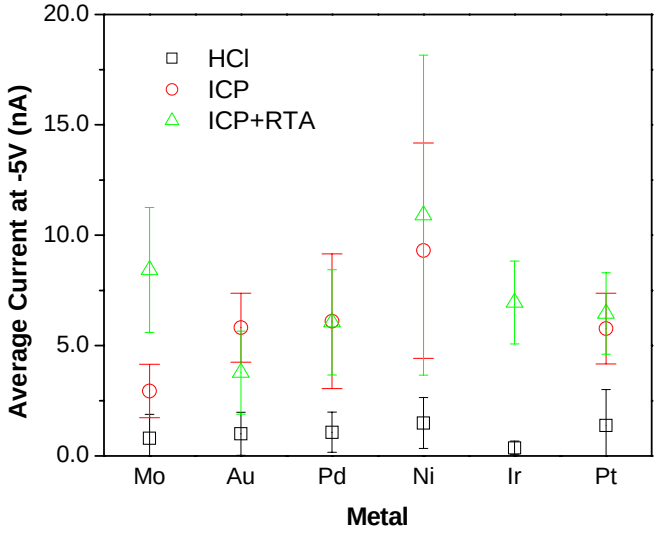

Figure 7.18. Statistical summary of reverse currents versus metal for all three process cases. There were ~23 diodes for each data point, and the error bars represent the standard deviation.

effects have been noted previously in GaN and AlGaN diodes. A theory for the discrepancy involves the presence of a thin, heavily n-doped layer near the surface which promotes tunneling under large reverse bias.[187] Alternatively, these currents have been explained by the presence of extended defects, such as screw dislocations, which act as the dominant conduction mechanism under reverse bias.[188]

Large-reverse bias sweeps were additionally performed to characterize possible changes in reverse breakdown voltage between the three surface preparation cases. The large series resistance effects noted above also affected these measurements. When corrected for the voltage drop across the resistive AlGaN for larger operating currents, the onset of series resistance effects was noted for reverse biases >20 V. The maximum voltage applied, due to instrumental limitations, was –100V, and this value corresponded to a value of –40 V across the actual diode. The results were similar for all samples for several Au, Ni, and Pt diodes, and no abrupt breakdown phenomena were noted.

Presumably, absent the current limiting effects from the high resistance, significant current breakdown would be noted for reverse biases larger than 40 V across the diodes, and differences between the three surface treatment cases could be observed.

7.8 Low temperature annealing effects: determination of annealing temperature

The thermal stability of gate metals in AlGaN-GaN HEMTs is of importance, since these high power devices are designed to operate for long periods at elevated temperatures. In particular, the comparison of thermal stability between the three cases can give clues to changes in interface state density and metal-AlGaN interactions.

Determination of a realistic annealing temperature is important to investigate the stability of all metals versus processing conditions. Additionally, changes to the slope of the S-plot can indicate changes in interface state density for all processing cases. Estimations of channel temperatures have been made by thermal calculation methods and by direct measurement of Raman spectroscopy peak shifts.[189,190] A novel measurement method is used here to establish steady state temperatures on high quality HEMT material. TLM structures from a HEMT die were mounted to a ceramic package and the two smallest TLM gaps (5 and 10 μm) were wire bonded to feedthrough pins on this package. These external pins were fastened to a special mount compatible with isolated electrical contacts on the JEOL 7800F scanning electron microscope. The sample stage contacts were electrically connected to wires, which were passed to the outside of the chamber via an ultra-high vacuum electrical feedthrough. The package, with the TLM exposed, was positioned under the collection mirror described in Chapter

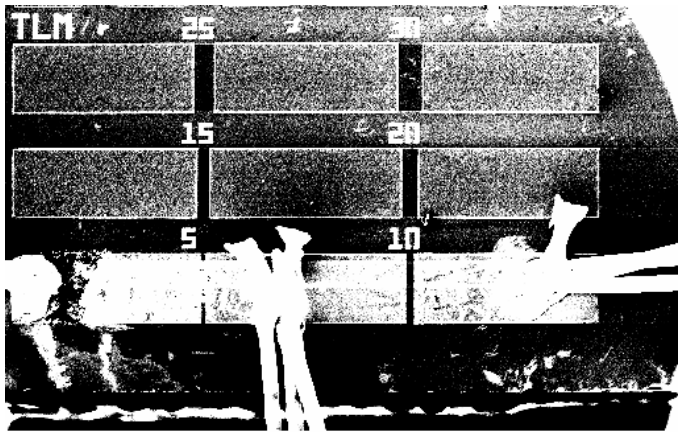

Figure 7.19. SEM micrograph of the TLM structure used to probe channel temperature using cathodoluminescence. The wire bonds connected to the TLM pads are visible in the picture.

2. While passing current through the TLM gaps, cathodoluminescence spectra were acquired. By noting the shift in GaN bandedge as a function of applied power, the temperature of the TLM gap was estimated using literature values of bandedge shift versus temperature. This temperature provides a good approximation of the thermal stress in a HEMT channel, since the dimensions and conductivity are similar. Moreover, the TLM structure is from the same die with HEMTs.

The HEMT material used for temperature measurement was grown by MBE on a silicon carbide substrate, with an AlGaN barrier of mole fraction 0.25 and thickness ~20nm. The GaN layer was 1μm thick and not intentionally doped. Measured values of contact resistance were ~0.5 Ω-mm and sheet resistance was ~500 Ω/square. A SEM micrograph of the TLM gap is shown in Figure 7.19. In this picture, the wire bonds connected to the 5 and 10 μm pads can be seen, with a common connection to the center pad. The gap width is 80μm. Representative I-V sweeps of the TLM gap are shown in

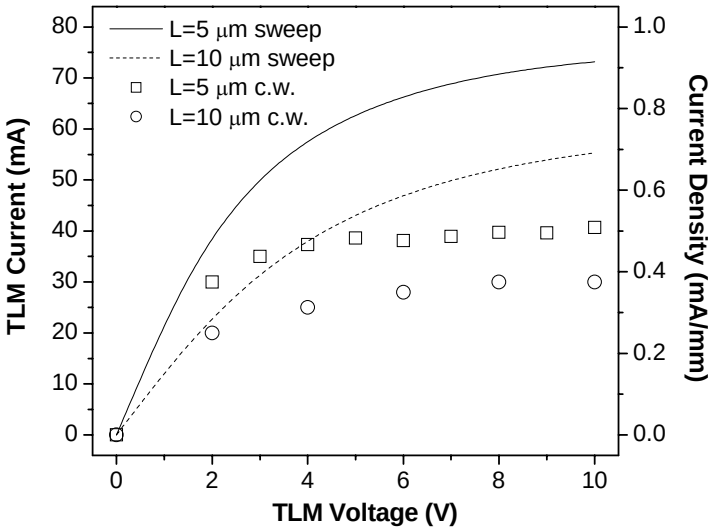

Figure 7.20. TLM current for sweeps (curves) and steady-state operation (symbols) for both TLM gaps. The symbol bias points were used for the cathodoluminescence study.

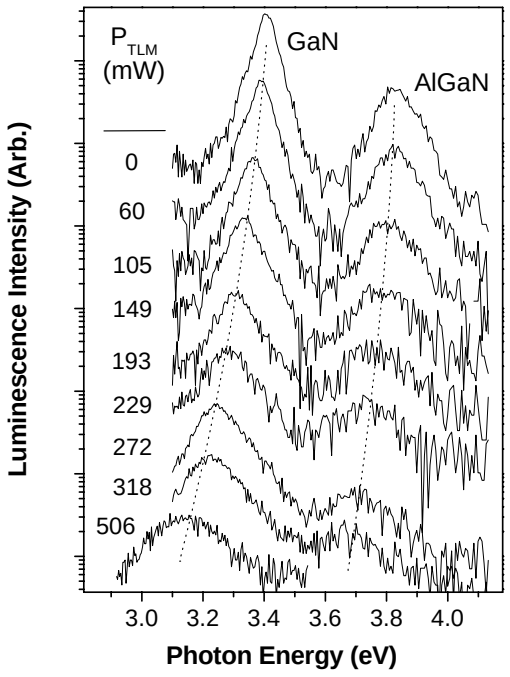

Figure 7.21. Raw cathodoluminescence data as a function of TLM power for the 5 mm gap. Both the GaN and AlGaN peaks shift to lower energies and broaden with increased temperature.

Figure 7.20 for both gaps. In this figure, the lines are fast (<1s) sweeps obtained on the HP4145A parameter analyzer, and the symbol series are the equilibrated currents after the structure has been raised to operating power. The effect of increased temperature during continuous operation clearly decreases the peak current, as channel mobility is decreased from increased scattering.[191] The equilibrated data are the points at which luminescence scans were acquired.

Figure 7.21 shows the evolution of the cathodoluminescence data with increasing power through the 5μm TLM gap. Cathodoluminescence scans were taken at a beam energy of 2 keV, which locates the electron-hole pair creation volume near the HEMT channel. For the scans corresponding to the three highest TLM power, the beam energy was adjusted to 3 keV due to the significant decrease in signal intensity with temperature. No significant differences in peak position were noted for beam energies between 2 and 20 keV, indicating that during equilibrium the GaN is uniform in temperature through almost the entire thickness of the film. The peak emssion energies of the GaN and AlGaN decrease, and the full width half-maximum of the peaks increase, as predicted from the Varshni relation.[192] The peak emission energy of the GaN, as determined from Gaussian fits of the raw GaN peaks, is plotted vs. power density in Figure 7.22. The decrease in energy is approximately linear with applied power. The peak energy is correlated with temperature from Ref. [193], which was published from the author's lab. In that paper, a GaN sample was heated resistively in vacuum, and the temperature was monitored by optical pyrometry. The GaN surface emissivity was calibrated by noting the melting points of pure elemental compounds (e.g., Al and Au) affixed to the surface of the GaN. Cathodoluminescence spectra were acquired while monitoring the GaN

temperature. Curve fits of the peak position vs. temperature resulted in a bandedge shift of ~6x10^{-4} eV/K. More involved fits of the data using the Varshni relation of $E_g = E_g^0 - \alpha T^2/(T-\beta)$ gave results similar to those using the simple linear approximation, so the latter is used here.

Finally, the TLM gap temperature is determined in Figure 7.23 vs. power density, using the band edge shift data in Ref. 193. Common power densities result in high temperatures. For example, for 5 W/mm applied power (a common figure) the gap temperature is ~400°C. It is possible these temperatures overestimate actual channel temperatures to some degree since (a) there is no gate in the TLM gap to conduct heat away, and (b) the power was applied in vacuum where air-cooling is not present. Indeed, previous simulations of channel temperature have shown that decreases in gate length increases channel temperature. With decreasing gate lengths required for high frequency operation, however, heat conduction via the gate may become less efficient. Additionally, the presence of passivation dielectric films on top of the HEMT layers (not present here) decreases the efficiency of heat transfer and air cooling, so these factors may well offset those previously discussed and imply these high temperatures are indeed attainable for common HEMTs. Moreover, record continuous operation power densities have been reported in excess of 12 W/mm[194], which lends further importance to the present measurements.

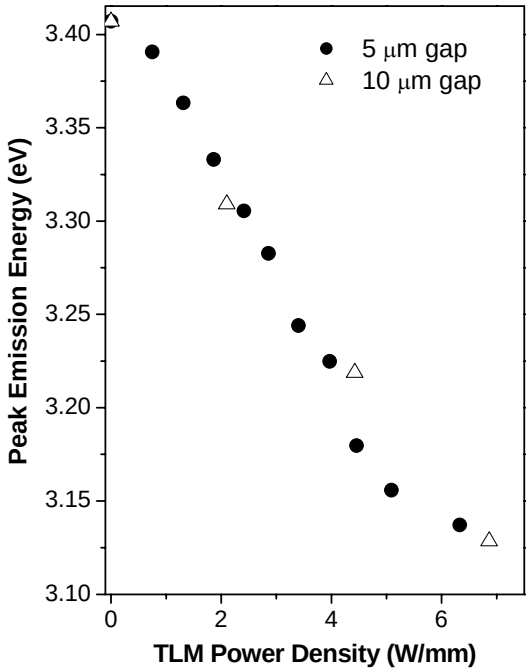

Figure 7.22. Peak emission energy, as determined from Gaussian curve fits, versus TLM power density for both TLM gaps.

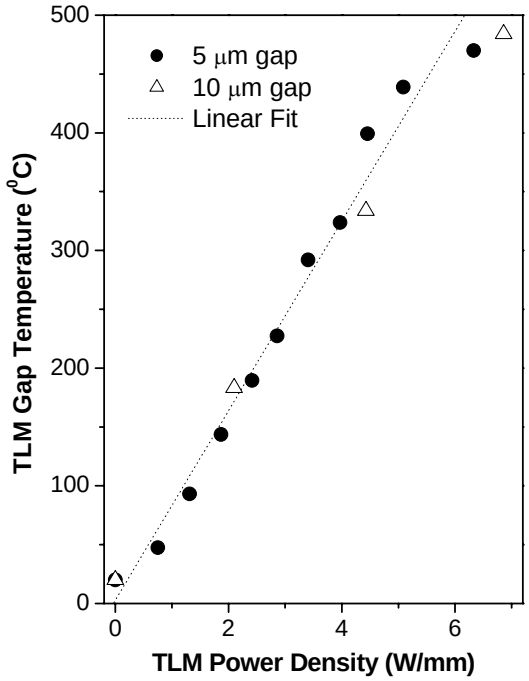

Figure 7.23. TLM gap temperature versus gap power, as calculated from the data in Figure 7.21 and $dE_G/dT = -6x10^{-4}$ eV/K from Ref. 193.

7.9 Low temperature annealing effects: effect on I-V characteristics and s-plot

Having established 400°C as an approximate channel temperature for 5 W/mm continuous operation, select AlGaN diodes were diamond sawed from the larger pieces and annealed in a furnace for 8 hours at this temperature in flowing ultra-high purity nitrogen at the Ohio State University cleanroom. I-V curves were measured with the HP4145A immediately before and one day after annealing. For most metals and surface treatment cases three or four diodes were measured in forward and reverse bias and averaged, as appropriate. All nickel diodes exhibited morphological changes after annealing, which resulted in the metal islanding on the semiconductor surface. The islands were discontinuous, and caused the currents to decrease by several orders of magnitude compared with the pre-annealed data. Previous studies of nickel diodes on AlGaN have suggested thermal stability through higher temperatures, but in those studies the Ni was capped with a thick Au layer, which may have prevented the morphological change. The post-annealing nickel diodes are excluded from the present analysis.

A summary of thermionic fits of barrier height for representative diodes from all metals is shown in Figure 7.24 for each processing case. The dotted lines in panes (b) and (c) correspond to the as-deposited values of S, which were calculated as <0.10 and >0.25 for the ICP and ICP + RTA cases, respectively. These values are in reasonable agreement with the S values presented in Figure 7.12. Slight differences in this quantity arise here due to these diodes being a subset of the original diodes and possible time effects due to the samples sitting in the atmosphere. In Figure 7.24, the notable changes for each processing case is the significant increase of barrier height for Pd and Pt (indicated by the upward pointing arrows). Increases in the Pt barrier heights could be

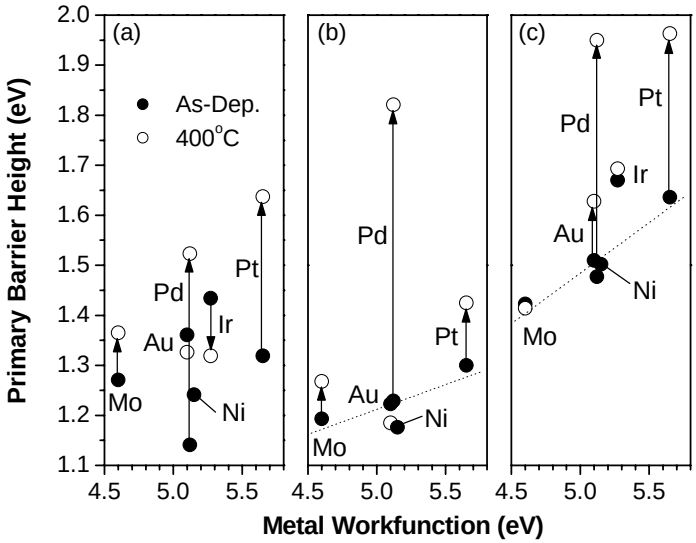

Figure 7.24. Barrier height versus metal workfunction for (a) the HCl case, (b) the ICP case, and (c) the ICP + RTA case. For all cases, the Pd barrier height increases significantly. For the latter two cases, an increase in is observed for the other metals. The dotted lines correspond to pre-annealing S values of <0.10 and >0.25 in panes (b) and (c), respectively.

accounted for by a reduction in interface state density, thereby improving the S-factor. Indeed, the general trend for Figure 7.24(b) and 7.24(c) is an improvement of the S-factor, with the ICP + RTA case improving from ~0.25 to ~0.50. This implies a reduction in interface state density from $3x10^{13}$ to $1x10^{13}$ $cm^{-2}eV^{-1}$, according to Eqn. (7.1). This difference of $2x10^{13}$ $cm^{-2}eV^{-1}$ would cause only a slight improvement in the ICP case, since the state density is initially high (~10^{14} $cm^{-2}eV^{-1}$), and this is in fact observed. A similar argument could be proposed for the HCl etch case, but as in the previous data the scatter in barrier heights is large enough that further study is needed to understand the interactions of the metals with the possibly contaminated or non-uniform surface.

The clear outlier for all three etch cases is the Pd diode. This metal exhibits a significant improvement in Schottky barrier. Previous investigators have noted the formation of a thermodynamically stable eutectic compound formed between Pd and Ga, thus producing Ga vacancies in AlGaN upon annealing. The formation of Ga vacancy complexes, expected to be ~2.5 eV below the AlGaN conduction edge[195], combined with the corresponding enrichment of the AlGaN alloy composition, may act to increase the barrier height to values much higher than predicted from the S-plot for all other metals.

Lastly, the thermal stability of the reverse currents is of key importance for characterizing the ICP + RTA process. Figure 7.25 summarizes the reverse currents at -5V for all diodes and for all three processing conditions. Each symbol on the plot is an average of two to four diodes before and after annealing. For each case except Al, the reverse currents decrease to values closer to the HCl case, which exhibits the lowest currents. For both plasma-etched cases, the effect of annealing is to restore the metal-semiconductor contact through reduction in interface states or extended defects caused by etching. The lack of these defects in the HCl case is evidenced by the absence of significant current reduction upon the same annealing process. For Al, the anneal may cause more intimate contact between the Al and AlGaN, as the Al migrates through an existing oxidation layer.

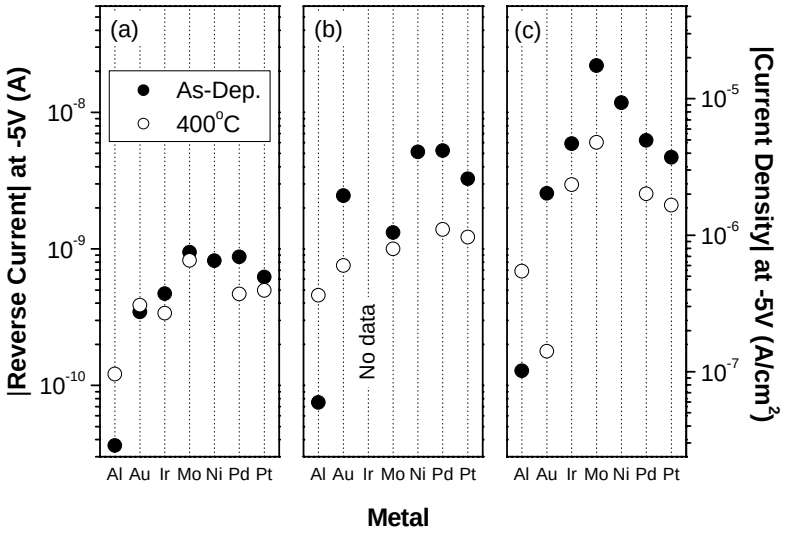

Figure 7.25. Changes in reverse current at –5V for (a) the HCl case, (b) the ICP case, and (c) the ICP + RTA case. In the latter two cases, the reverse current improves for all metals except Al.

7.10 Summary of results

The characterization and electrical results for all three processes can be summarized as follows:

- The AlGaN material as-grown exhibits at least two compositional phases, as shown from x-ray diffraction and CL. These phases are close enough in mole fraction as to not significantly affect the barrier study. The average value of the two phases is ~43.5%, which is higher than the growth target, and higher than typically used for HEMTs. Nonetheless, all samples exhibit barriers for all metals, except for Ir on the ICP case, which lifted off during the post-deposition cleaning procedure. In this sense, this work represents a systematic study of many metals for a previously uncharacterized regime of mole fraction.

- For all metals, the largest scatter in I-V characteristics is for the HCl prepared surface. The ICP surfaces give tightly distributed I-V curves, and the addition of the RTA step results in an intermediate, but more uniform than the HCl, case. This implies that etch damage results in a pinned barrier, forcing all ICP diodes to exhibit similar I-V curves. As the etch damage is annealed in the ICP+RTA case, the previous inhomogeneous nature of the AlGaN re-emerges, although to a lesser extent.
- The diodes exhibit a primary barrier that is pinned with the ICP process (S~0.05) and less pinned for the ICP + RTA sample (S~0.30). The changes in the interface index, S, imply the anneal results a reduction of surface states from ~$2x10^{14}$ to $2x10^{13}$ $cm^{-2}eV^{-1}$, by applying the model presented in Eqn. (7.1).
- Secondary barrier effects seen in the HCl etched sample are ~1 eV, largely metal-independent, and are dominated by spatial position across the piece.
- Reverse currents are uncorrelated with the primary or secondary barrier and are an order of magnitude worse for the two plasma processes.
- Low temperature, long period annealing improves the S-factor for the plasma-etched cases, and causes an anomalous interaction for Pd, possibly due to chemical interaction with Ga from the AlGaN, as suggested in Ref. 163.
- Most reverse currents are improved with this anneal, for all surface processes, although not significantly. More importantly, the ICP processes do not make the diodes more susceptible to degradation upon annealing at device operation temperatures. These temperatures were determined above with a novel method utilizing cathodoluminescence.

7.11 Discussion

The uniform barrier heights observed in the ICP etched case suggest a highly pinned surface, due to a large density of near-surface defects produced by the plasma. The partial un-pinning of this surface with the addition of the RTA step after the ICP plasma suggests the removal of ~$2x10^{14}$ $cm^{-2}eV^{-1}$ of these states, as calculated from the difference in index indices (see above). Previous investigators noted pinned barriers near 0.5 eV on plasma-treated GaN surfaces.[196] Compositional analysis in that study revealed a near-surface deficiency of nitrogen, resulting in nitrogen vacancies in the AlGaN.[197] The surface energy level of these vacancies lies approximately 0.5 eV below the conduction band edge of GaN, which is consistent with the pinning energy.[198] The nitrogen vacancy level in AlGaN is expected to be farther from the conduction edge. For example, in Ref. 199 the energy of the nitrogen vacancy at the surface was calculated to be ~1 eV from the conduction edge for aluminum mole fractions of ~40%. Such calculations are consistent with the present result, where the barrier is pinned near 1.0 eV for all metals on the ICP treated surface. Moreover, reduction in state density with the RTA process prior to metallization results in unpinned barriers larger than 1.0 eV. This is consistent with previous studies, where lower annealing temperatures (400 ºC) significantly reduced the nitrogen vacancy level on GaN.[200]

The two ICP-treated surfaces exhibit a significant improvement in diode uniformity, as compared with the HCl etched case, both in terms of forward and reverse currents. The uniformity of the ICP case can be accounted for by the pinning effects noted previously, but the uniformity of the ICP + RTA process may indicate other effects. The annealing of plasma-induced defects with the RTA step should result in diodes

exhibiting similar non-uniformities to the HCl case. This is not observed, however, which suggests the presence of near-surface defects as-grown that are physically ablated with the 300 Å etch. In general, the similarities in spatial variation for the several metals on the HCl piece, as shown in Figures 7.14 and 7.17, suggest that the diode electrical properties are likely controlled by bulk and near-interface states in the AlGaN, rather than specific metal-AlGaN interface interactions. The nature of the defects for all surface treatments will be addressed by depth- and spatially-resolved cathodoluminescence spectroscopy in Chapter 8.

In practice, the preferred surface treatment for producing uniform diodes (or HEMT gates) is an ICP variant, where practical. Highly uniform barriers can be produced by sufficiently aggressive etches, producing a highly pinned barrier. The addition of a RTA or similar thermal process significantly reduces near-interface trap densities, which is important for suppressing breakdown and trapping mechanisms, which can limit gate performance. For both ICP processes realized here, the leakage currents increased by almost an order of magnitude over the corresponding HCl diodes for a realistic gate bias. Should this be unacceptable, gate leakage currents can be reduced by the addition of an oxidation step.[201] Thermal stability of all metals was shown to be similar for all processes and metals, with improvements in reverse currents for all metals *except* Ni. This metal exhibited a significant reduction in current due to the emergence of discontinuous islands forming on the AlGaN. Reduction in trap density, as suggested by improvements in the interface index after annealing, may account for improvements in the reverse currents.

CHAPTER 8

CATHODOLUMINESCENCE CHARACTERIZATION OF AlGaN VERSUS SURFACE TREATMENT AND COMPARISON WITH DIODE ELECTRICAL PERFORMANCE

8.1 Introduction and motivation

The data in the previous chapter show significantly different diode behavior versus the three surface treatments. These differences in electrical behavior suggest large changes in the material characteristics for each processing condition. These changes may include the formation of point and extended defects, including deep traps formed near the surface and resulting metal-semiconductor interface. Moreover, the ablation of material from the surface with the plasma treatment may reveal defects that do not extend completely to the semiconductor surface. In addition to the notable differences in barrier heights and reverse currents for the three processing conditions, the degree of variance for the I-V curves for a given metal was also different for each case. For example, the forward I-V characteristics exhibited a high degree of scatter for all metals tested for the chemically prepared case, whereas the two plasma-etched surfaces yielded much more uniform electrical behavior.

To help understand these differences, the bulk AlGaN characteristics are investigated using cathodoluminescence spectroscopy. In addition to the radiation studies described in Chapters 3, 4, and 5, cathodoluminescence studies have also been

previously used to study device characteristics as-fabricated and versus various processing conditions. An example using cathodoluminescence is the conversion of Au-ZnO contacts from ohmic to Schottky behavior after oxygen plasma treatment. This dramatic change has been identified with the reduction of oxygen-related near-surface eep-level emissions.[202] Likewise, cathodoluminescence has been used to observe spectral differences in SiC due to difference phases and defects in the material that account for the presence of multiple barrier heights, as measured electrically.[203] For nitrides, the author's group has used cathodoluminescence to establish correlations of deep levels and ratios of defects with specific contact resistivity for HEMT material.[29,204] Cathodoluminescence data have also shown processing-related compositional changes in the near-surface region for Schottky barrier studies on AlGaN that correlated with measurements of the barrier height.[205,206] Using the same approaches, depth-dependent cathodoluminescence is used here to help identify material properties responsible for the variance in diode behavior across each piece and as a function of pre-metallization processing.

8.2 Overview of cathodoluminescence data

A CASINO simulation of the electron beam energy loss versus depth into the AlGaN is shown in Figure 8.1(a). Figure 8.1(b) of this figure shows the peak energy loss depth and maximum range. The latter quantity was extracted by a linear fit of the tail of the distributions shown in Figure 8.1(a). In this simulation, the mole fraction was chosen as 0.40, and the material density was interpolated as 4.98 grams/cm^3. 10^5 electrons were simulated, and the resulting curves were smoothed and normalized to the peak value. Based on these simulations, 1 and 10 keV were originally chosen as analysis energies for

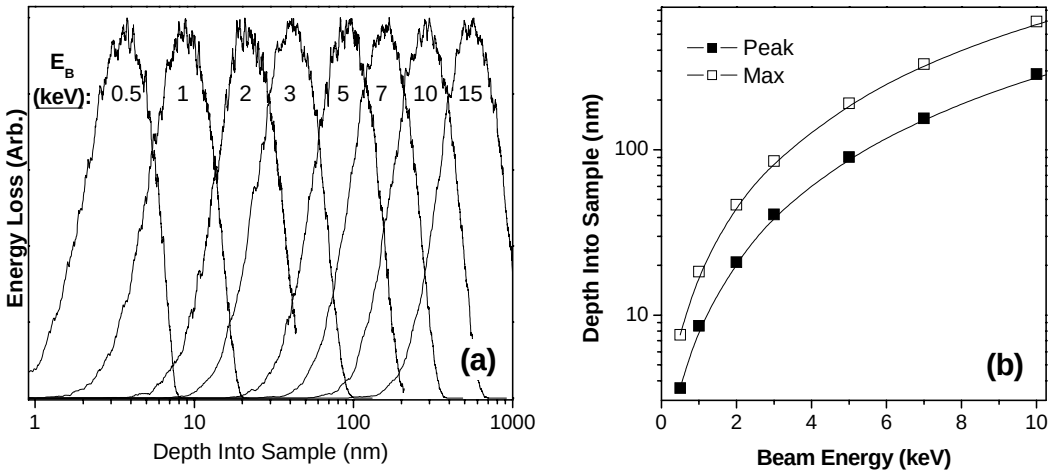

Figure 8.1. Results of CASINO simulations for the AlGaN. Dose-depth curves are shown in pane (a), and peak and maximum depths of excitation are shown in pane (b).

investigating spatial dependence of the spectra. 1 keV excitation should primarily probe near the semiconductor surface, and 10 keV should probe deep in the material, thereby discriminating surface effects from buried features outside the resulting depletion widths for the diodes (~100 nm for all metals). Additionally, the depth dependence of emissions was acquired when appropriate by taking scans from 1-15 keV in suitable energy steps. This data will be presented below. All spectra were acquired immediately adjacent to the row of Pt diodes, between the Pt and adjacent Mo diodes. The sample temperature was 12K and the scan size was a square region of ~50 μm per side. For the 400 μm diameter diodes here, this scan size samples an area equivalent to ~2% of the diode area and 10% of the distance between diodes (i.e., 50 vs. 500 μm). For most cases, the spatial variation in spectra between adjacent diodes was small enough that assigning correlations between the small scan area and larger diodes was possible (see below). Beam currents were 0.1 nA for 10 keV beam energy, and were adjusted such that constant beam power ($=V_B x I_B$) was maintained, unless otherwise noted. The monochromator slits were adjusted such

that the signal maximum was near the system maximum (~300,000 counts). For most cases, this resulted in ~0.25 mm slits or less. Resolving power experiments showed that no significant improvement in cathodoluminescence lineshape was achieved by adjusting the slits from 0.5 mm to smaller values, indicating that all emissions were broad relative to the practical spectral resolution. For a given set of experiments (e.g., depth, temperature, or spatial dependences) the slits were kept the same for all samples.

In the previous chapter, Pt was chosen for extensive analysis due to the high workfunction (i.e., large discrimination between primary and secondary barrier effects) and chemically inert properties. Focusing the data acquisition near these diodes should allow for direct comparison with the I-V data for this metal, and for correlation between spectral properties and the scatter in electrical behavior. 10 keV scans adjacent to all Pt diodes, and for all surface treatment cases, are shown in the respective panes of Figure 8.2. In this figure, all scans are plotted together to give a rough guide to the eye for spectral uniformity and lineshape. 10 keV scans are shown here to accentuate the differences between the three cases (see subsequent discussion). The spectral region shown in the figure corresponds to all the luminescence observed in the sample for emission energies down to the detection limit of ~1.3 eV. That is, no distinct optical features were observed below ~3.9 eV.

There are several features evident in the figures. First, the spectra for all three cases exhibit a common, prominent, broad emission from ~4.2 to ~4.3 eV. As discussed in Chapter 7, this emission is composed of at least two phases of AlGaN, which originate during the wafer growth. A more detailed examination of these emissions will be given below. Second, there are also prominent luminescent differences between the three

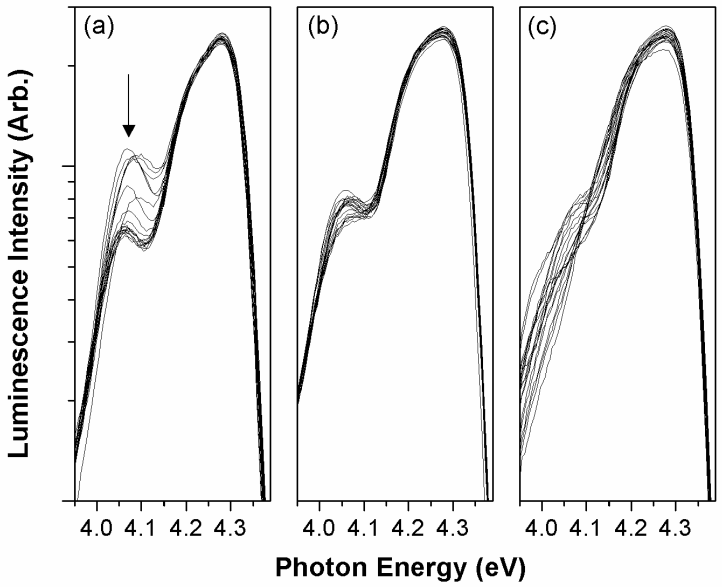

Figure 8.2. Overview of all 10 keV cathodoluminescence curves for (a) the HCl surface, (b) the ICP surface, and (c) the ICP + RTA surface. The arrow in pane (a) indicates the highly variable nature of the spectra for the HCl case, relative to the ICP treated surfaces.

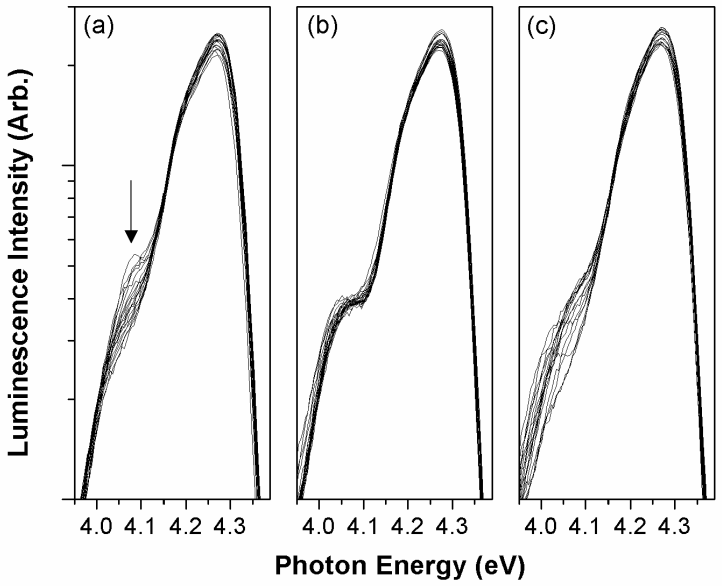

Figure 8.3. Overview of all 1 keV cathodoluminescence curves for (a) the HCl surface, (b) the ICP surface, and (c) the ICP + RTA surface. The arrow in pane (a) indicates the highly variable nature of the spectra for the HCl case, relative to the ICP treated surfaces.

cases, corresponding to the different electrical characterization features seen in the three samples in the previous chapter. Namely, the HCl case in Figure 8.2(a) shows a large variation in emission at ~4.05 eV for the different positions measured. A large variation was also evident in the forward I-V characteristics of the Pt diodes. In Figure 8.2(b) and 8.2(c), the ICP-etched cases exhibit less scatter, particularly for the ICP-only case. This also follows the trend noted for the I-V characterization, especially for the ICP-only case. The first order correlations between the electrical and spectral behavior suggest the cathodoluminescence data may reveal physical origins of the electrical characteristics. To fully examine these trends, the luminescence data was de-convolved into individual peaks via curve fitting. The process includes evaluating the depth and spatial dependence of the de-convolved peaks, and additionally analyzing temperature dependent studies of all emission to help assign physical origins.

8.3 Depth dependence of cathodoluminescence data

Figure 8.3 shows the 1 keV cathodoluminescence data, complementary to the 10 keV case shown in Figure 8.2. The trends discussed in Section 8.2 are still present, but minimized. For example, the scatter in the HCl curves in pane (a) is smaller than in the 10 keV case. Additionally, the ICP etched sample spectra in pane (b) are tightly grouped, as before. A similar argument can be made for the ICP + RTA process sample shown in pane (c). For all three etch cases, the slightly different appearance between the 1 and 10 keV spectra, which correspond to different probing depths into the sample, suggests the depth dependence of the emissions. For this part of the curve fitting, the spatial variation in luminescence, as shown prominently in Figure 8.2(a), is temporarily put aside. From

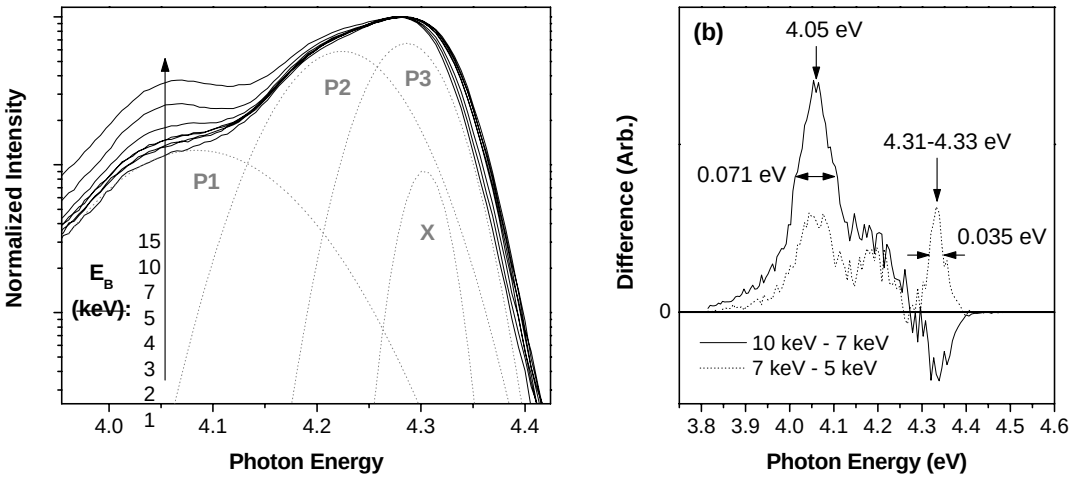

Figure 8.4. Typical depth dependence of the cathodoluminescence data. The raw data are shown in pane (a), with the common curve fits shown as dotted curves (see text). Two typical difference spectra are shown in pane (b), illustrating the growth of the 4.05 emission into the sample.

several iterations of curve fitting, the depth dependence of the emissions was shown to be independent of the spatial variation (i.e., two different peaks). The spatial variation of peaks will be addressed in Section 8.4. For the time being, the curves in Figures 8.2(a) and 8.3(a) exhibiting the lowest absolute emission near 4.05 eV are regarded as "typical", and form the basis of the present curve fitting. The curves with large ~4.05 eV emission will be shown in Section 8.4 to be atypical and due to spatial vartiaion of the material.

Figure 8.4(a) shows the depth dependence of the HCl-etched piece in a "typical" region (as previously defined). The peak intensity values were similar for all beam energies, due to the data being taken in constant power mode (peak variation ~ 30%). Here, the data have been normalized to the peak value for ease of comparison. The dotted curves labeled "P1", "P2", "P3", and "X" were common to all cases. The "P2" and "P3" peaks were attributed in Chapter 7 to different phases of AlGaN and are always present in all etch cases and depths. Likewise, the "P1" and "X" peaks are always

present. The exact energies, linewidths, and proposed physical origin of these peaks will be discussed in Section 8.6. For the HCl piece shown in Figure 8.4(a), the data are similar from 1 through 5 keV, above which the emission intensity near 4.05 eV increases significantly (i.e., by more than twice from 5 to 15 keV). An exact determination of this peak position and width is extracted from the difference spectra in Figure 8.4(b). In this figure, the 7 keV spectrum has been subtracted from the 10 keV case, and, similarly, the 5 keV has been subtracted from the 7 keV data. In both cases, difference curves reveal a prominent emission centered at 4.05 eV with a full-width half-maximum of 71 meV. This peak is labeled "D" (for depth) henceforth, due to the increase of this emission with excitation depth. Also in the difference spectrum, changes in peak "X" at ~4.3 eV are observed. In both cases, the peak width is 35 meV, and the position varies from 4.31 to 4.33 eV. This is consistent with independent curve fits of this peak.

Figure 8.5 summarizes the curve fitting for representative diodes for each of the etch cases. This figure shows the integrated peak intensities versus electron beam energy for the peaks discussed thus far. For all three etch cases, peaks "P1", "P2", "P3", and "X" exhibit similar behavior with depth and relative magnitudes for all cases. This supports the assertion that these peaks are related to the as-grown sample and are not significantly affected by processing. The depth peak "D" exhibits markedly different behavior for the three cases. As suggested by Figure 8.4(a), "D" appears only for beam energies greater than 4 keV in the HCl case (Figure 8.5(a)), whereas this peak is present for all energies in the ICP case in Figure 8.5(b). Moreover, the peak is completely absent for ICP + RTA case in Figure 8.5(c). Although the ICP process ablates the surface of the material, the ~30 nm removed by this process is insufficient to account for the shift in

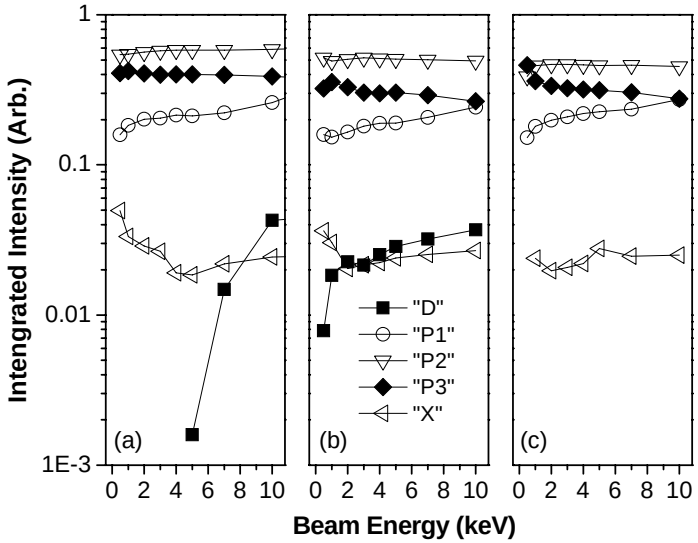

Figure 8.5. Results of all depth dependence curve fitting for all peaks in (a) the HCl case, (b) the ICP case, and (c) the ICP + RTA case. Similar behavior is noted for all peaks except the "D" peak, which is present deep in the sample for the HCl piece, at all depths for the ICP piece, and completely absent for the ICP + RTA case.

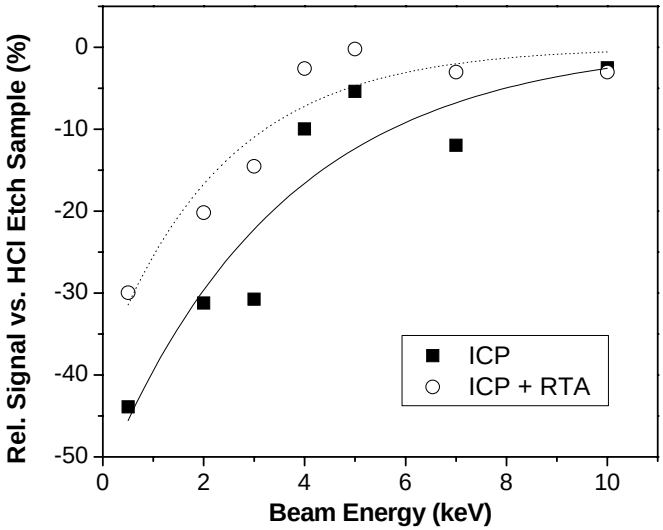

Figure 8.6. Total integrated emission intensity for the ICP etched cases, relative to the HCl case. For both ICP processes, there is a relative decrease in emission near the surface.

depth dependence of "D" from Figure 8.5(a) to 8.5(b). That is, the 5 keV onset of "D" in the HCl case implies this feature is present at depths greater than ~200 nm (from Figure 8.1b). Removing only 30 nm can not account for the onset shift to 0.5 keV. Evidently, the plasma process *creates* the defect "D" from the surface of the sample to at least a depth of ~200 nm. Deeper than 200 nm, the presence of this defect can be a combination of as-grown and process-induced contributions. Finally, the RTA step after the ICP etch removes this defect entirely. The physical origin of this peak and the implications for diode performance will be addressed in subsequent sections of this chapter.

A final depth-related consideration is the change in total luminescence intensity versus processing condition. Such an analysis can give information about the depth of damage introduced by the ICP process. For this analysis, the *absolute* emission intensities for each beam energy were compared for the plasma cases versus the chemically etched surface. Deep non-radiative traps formed in the near-surface region by the plasma process can result in a decrease in luminescence due to competitive recombination. Indeed, such results are shown in Figure 8.6 as a ratio of the total luminescence intensities for the plasma etches relative to the HCl case, for all beam energies. The fits in the curve are first-order exponential fits. From the figure, the ICP etch results in a decrease in radiative recombination of >40% in the near-surface region. The ICP intensities converge towards a value comparable to the HCl case (i.e., 0% difference) for beam energies greater than 10 keV. From inspection of the excitation depths in Figure 8.1(a), this implies the damage is confined to within 50-100 nm of the surface, since the 10 keV electron-hole pair generation volume is beyond this region. This effect is also noted for the ICP + RTA case, although the decrease in radiative

efficiency appears to be somewhat less in this case (e.g., 30% decrease versus 45% for 0.5 keV). Evidently, the RTA process partly reduces the ICP-induced damage, as well as significantly affecting the radiative characteristics as a function of depth. The implications for diode performance will be discussed in Section 8.7. Section 8.8 gives an alternate explanation of the decrease in luminescence intensity.

8.4 Variation of cathodoluminescence data across the HCl etched surface

Now that the depth dependent peak fitting has been established, the variation in emission across the HCl piece is addressed. As shown in Figures 8.2 and 8.3, the HCl-etched surface exhibits a high degree of scatter in the spectra for emission energies between ~4.0 and ~4.1 eV, with the effect being more pronounced in the 10 keV data. For this case, in particular, there is a clear difference between "typical" spectra, which are tightly grouped and of low intensity in this spectral region, and "atypical" spectra, which exhibit high intensities here. Several similar typical (e.g., adjacent to diodes 2-12) and atypical (e.g., adjacent to diodes 15-19) spectra are averaged and plotted in Figures 8.7(a) and 8.7(b) for 1.0 and 10 keV beam energies, respectively. Since the rest of the spectral regions are similar in shape and intensity, a difference is taken in each case between the typical and atypical cases. The results of this subtraction are shown on each figure. For each beam energy, the result is a single Gaussian peak at 4.08-4.09 eV with a full width half-maximum of 0.075 eV. This peak is labeled "S" (for spatial), and the results of depth dependent curve fitting of a region prominently exhibiting this new peak are shown in Figure 8.8. It is worth noting that this peak is independent of the depth dependent peak "D", in terms of lineshape and peak position, although the peaks are separated by a small

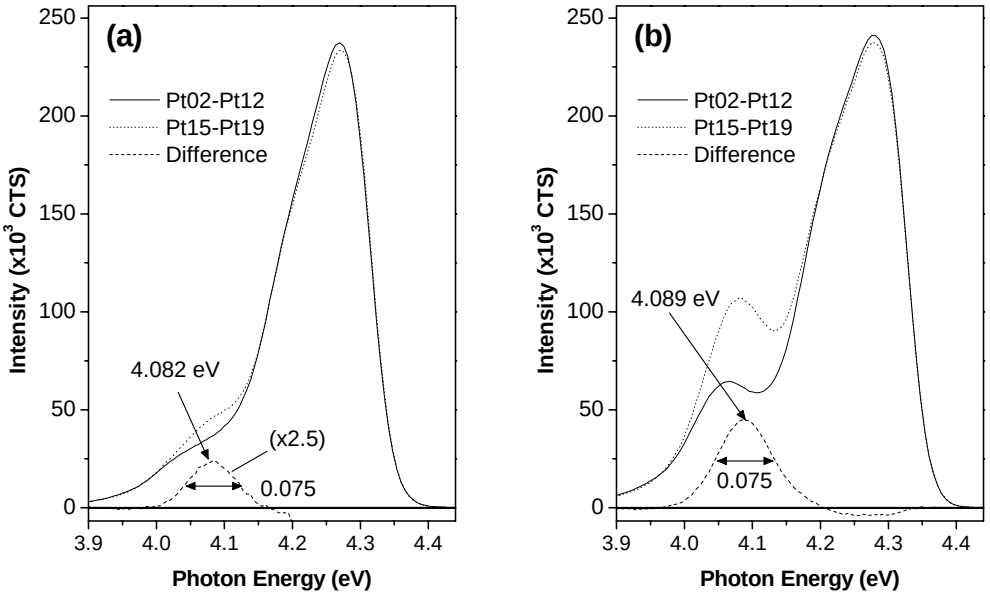

Figure 8.7. Typical difference spectra for (a) 1 keV and (b) 10 keV beam energies. The result of subtracting "typical" spectra from "atypical" ones is the narrow peak at ~4.08 eV.

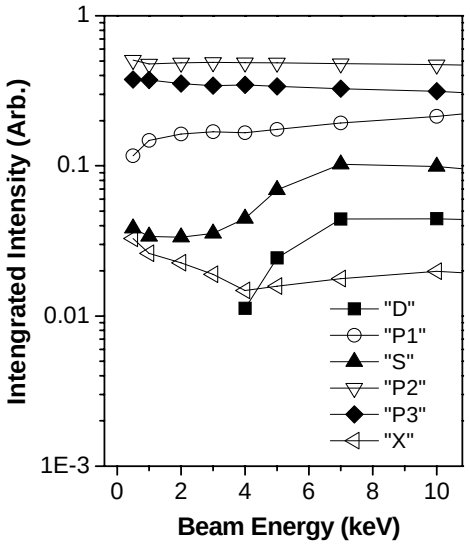

Figure 8.8. Results of depth dependence peak fitting for a region on the HCl sample exhibiting the "atypical" "S" peak.

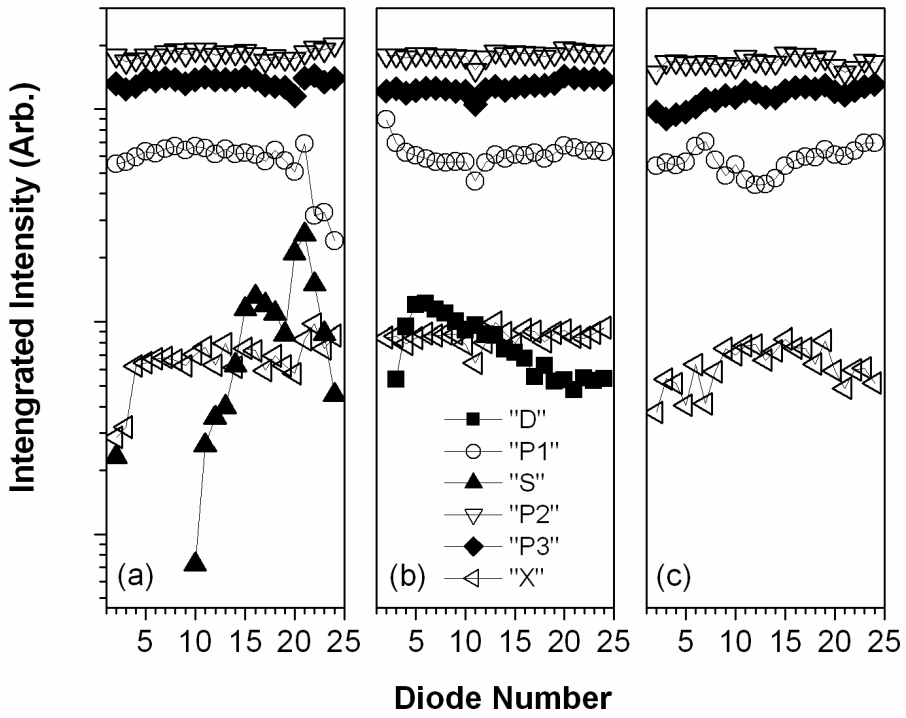

Figure 8.9. Summary of all spatially-dependent curve fits at 1 keV for all peaks in (a) the HCl case, (b) the ICP case, and (c) the ICP + RTA case. The "S" peak is highly dependent on spatial position for the HCl sample. The two ICP samples are generally uniform, with the prominent difference being the absence of the "D" peak in the ICP + RTA case.

amount of energy (~30 meV). This implies these two peaks may correspond to different defects and may affect electrical properties of the diodes in different ways.

8.5 Spatial dependence of all peaks

With all six peaks established, curve fits were performed on the spectra adjacent to every diode on all three samples. For these fits, the "D", "S", and "P1" peaks were constrained in energy position and peak width. Without these constraints, the fitting routine would arbitrarily arrange the three peaks with significantly different energies and

linewidths, to add a minimal improvement to the quality of the fits (e.g., r=0.995 vs. r=0.9995). With the previous depth- and spatial-dependence studies, the peak positions and lineshapes are well established, so the constraint is justified. The peak widths of "P2", "P3", and "X" were also constrained, but not the peak energy. This freedom was permitted to allow for slight changes in mole fraction(s) across the pieces. Minimal effects of this nature were observed (e.g., ~10 meV shifts in peak position for all three). The integrated intensities of all six peaks versus adjacent Pt diode number are shown in Figure 8.9 for a 1 keV electron beam. As expected from the depth dependence data presented previously, the "D" (depth) peak is absent from all positions on the HCl etched sample, since this peak only appears at higher beam energies. Also as expected, the peak is always present in the ICP case, and always absent in the ICP + RTA case. All other peaks, e.g., “P1”, “P2”, “P3”, and “X”, behave generally the same across each piece and when comparing the different pieces to one another. As with the depth dependence, this suggests these peaks have little effect on the diode properties, since the similarity of the emissions are not in agreement with the variation in diode properties. If any emissions are to correlate with the electrical behavior, it must be either the "D" or "S" peak, or both.

Indeed, the data suggest there are four major correlations between the spectral and electrical data:

(1) The variation of the spatially varying peak at ~4.085 eV, “S”, across the HCl prepared surface correlates with the variation in current at the primary barrier turn-on in Figure 7.14 and the corresponding regions of second barrier height dominance in Figures 7.15 (for Mo) and 7.16 (for Pt). The data from Figure 7.14 are plotted along side the integrated values of “S” in Figure 8.10. The regions of large current in this figure,

correlating with regions of large integrated "S" intensities, predominantly exhibit barrier heights of ~1.0 eV, as extracted from the thermionic fits. The "S" defect therefore lowers barriers from the typical values (~1.4 eV for Mo and ~1.5 eV for Pt) to a value substantially less. Moreover, the resulting barrier heights in this region appear to be independent of the metal.

(2) Similarly, the emergence of the "D" (i.e., depth) peak at ~4.05 eV near the surface of the AlGaN after ICP etching corresponds with the barrier heights for all metals being pinned at ~1.0 eV for every position across the piece. The similar position of "D" and "S" in energy suggests a similar position in the AlGaN band gap and may result in a similar transport mechanism. See Section 8.7.

(3) The *absence* of both "S" and "D" for all depths and spatial positions in the ICP + RTA processed piece correlates with the a reduced presence of the ~1.0 eV barrier for all metals tested, as compared with the other two surface preparations, the highest S-factor for the primary barriers, and the best ideality factors for these all metals. In particular, the simultaneous reduction (although not complete elimination) of the ~1.0 eV barrier effects and observation of the elimination of the "S" and "D" peaks suggests the significant reduction of a transport mechanism assisted by these two defects.

(4) The reduction of near-surface total radiative intensity suggests the presence of traps, which are not eliminated for the RTA process. Consistent with this, each of the two ICP treated surfaces exhibit an order of magnitude increase in reverse currents for all metals, as compared with the HCl-prepared sample.

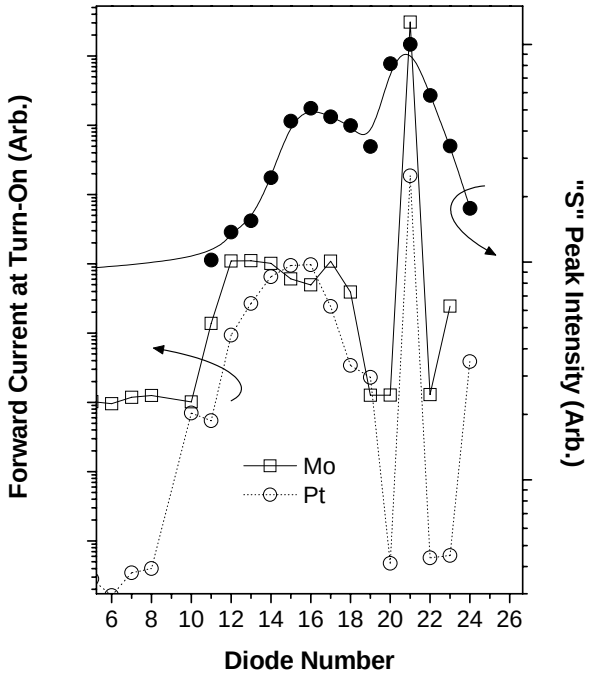

Figure 8.10. Comparison of the Mo and Pt currents at the turn on voltage and the integrated "S" peak, versus position on the HCl piece.

8.6 Summary of energies and temperature dependences of all emissions

In order to validate the observations in Section 8.5, the physical origins of all peaks must be addressed. In addition to the peak position in the bandgap, which can be inferred from the absolute emission energy, the temperature quenching of the peaks adds additional credence to peak assignments by allowing comparison with literature values. The radiative intensity of emission decrease with temperature due to thermal de-population of states and radiative competition.[83,207] The peaks are fit according to the standard relation:

$$I(T) = I_0 \times \left(1 + \sum_i \alpha_i \exp\left(E_{Ai} \Big/ kT\right)\right)^{-1} \tag{8.1}$$

where I_0 is the limiting low temperature intensity, α is related to radiative efficiency of the recombination channel, and E_A is the activation energy of this channel. The sum accounts for multiple channels of recombination affecting the temperature quenching. These channels include depopulation of band gap states with temperature (e.g., shallow dopants thermally activated into the valence or conduction band) and thermal activation of nonradiative processes.

First, the total intensity versus inverse temperature for the 3 keV electron beam energy is shown in Figure 8.11. This gives a qualitative indication of large-scale changes to the thermal quenching properties of the bulk material. The HCl and ICP + RTA cases exhibit similar behavior, but the ICP only process is significantly different, indicating the presence of a large number of defects compared with the other surface preparation cases. The individual defect activation plots are shown in Figure 8.12. A summary of all activation parameters is given in Table 8.1. All thermal activation fits were satisfied with at most a two-channel recombination model, as shown in the table.

Feature	12K Peak Pos. (eV)	12K FWHM (meV)	α_1	E_{A1} (meV)	α_2	E_{A2} (meV)
Total Intensity HCl	--	--	0.78	9.6	39	44
Total Int. ICP	--	--	5.1	20	1148	94
Total Int. ICP + RTA	--	--	2.0	6.8	71	46
"D"	4.049	71	8.9	16	4.9×10^7	152
"P1"	4.084	152	2.8	6.9	8.0	28
"S"	4.085	75	79	41	4.1×10^6	150
"P2"	~4.215[1]	97	0.36	10	84	59
"P3"	~4.282[1]	66	1.1	11	297	55
"X"	~4.310[1]	36	25	13	--	--

[1]Unconstrained during fitting routine; variance across piece and depth ±0.005 eV.

Table 8.1. Summary of peak positions and full width half-maxima at 12K and temperature quenching data for all peaks and total luminescence intensity.

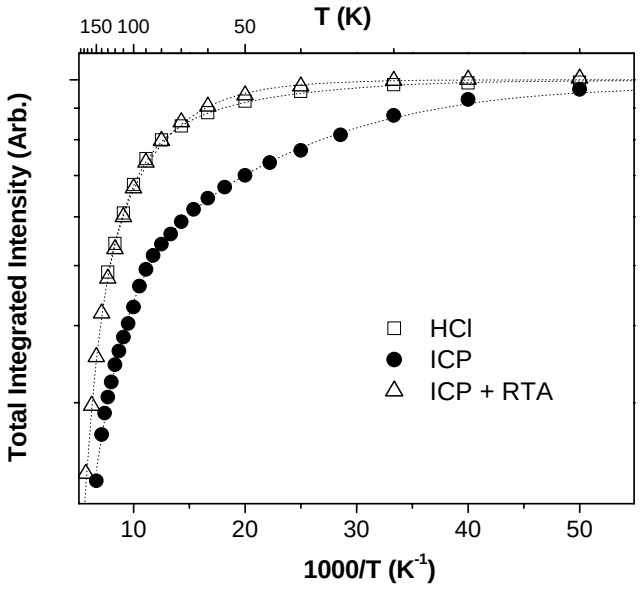

Figure 8.11. Temperature dependence of the total luminescence intensity for all three etch cases.

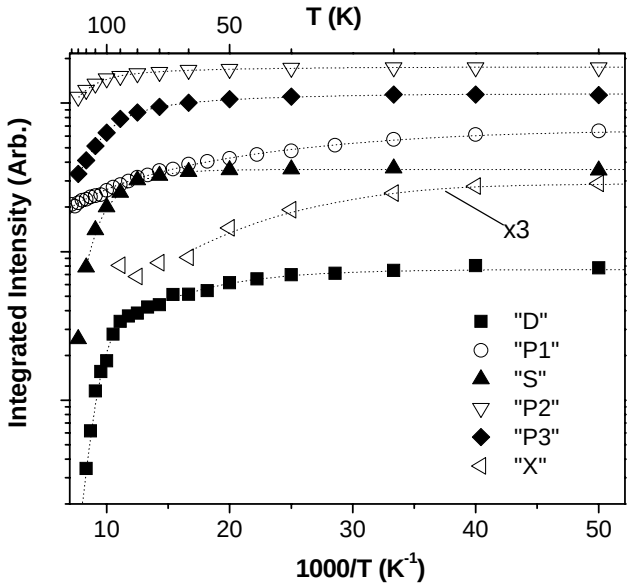

Figure 8.12. Temperature dependence of the integrated intensity of all emissions derived from curve fitting.

Many literature reports have been devoted to luminescence bands in GaN, with a large number of peaks documented.[208] Despite the large volume of data, there is yet much confusion on the origin of many of these features, due to the advances in the nitride material system being relatively recent and the simultaneous pursuit of several growth and processing techniques. The situation is similar, if not worse, in AlGaN, where fewer reports exist due to the inaccessibility of photoluminescence for mole fractions above ~30%. This is because the bandedge exceeds the energy of most common excitation sources. Very few reports exist for the mole fraction used in the present study (>40%), but to varying extents, common dopants (e.g., Si), impurities (e.g., C and O), and defects (e.g., vacancies) have been studied for a reasonable range of mole fractions. The role of extended defects are generally not well documented with respect to luminescence studies. Despite this, reasonable estimations can be made regarding the nature of the peaks in Table 8.1.

In Chapter 7, peaks "P2" and "P3" were attributed to Si doping-related excitonic luminescence from two different phases of the AlGaN, with mole fraction separation of ~2%. The activation energies of ~10 and ~60 meV given in Table 8.1 for the two phases are in very good agreement with literature reports of thick Si-doped AlGaN films with comparable doping densities to the present study (~$3x10^{17}$ cm^{-3}).[209] In Ref. 209, the Si donor-bound exciton peak, D^0X, gave activation energies (E_{A1}, E_{A2})=(5, 31 meV) and (16, 95 meV) for Al mole fractions of 23 and 50%, respectively. Interpolating these values to the present study (42%) gives 10 and 67 meV for the two activation energies, in good agreement with ~10 and ~60 meV. Another study reported comparable photoluminescence results for similar mole fractions (E_A<70 meV for ~45%), although

only one activation energy was reported there.[210] Notably, the lack of significant spatial variation of these two peaks implies changes in intentional doping can not account for the observed spatial variation in diode electrical properties, e.g., secondary barrier and reverse current effects.

The "P1" peak is sufficiently broad that it likely could be resolved into multiple components. Furthermore, the higher temperature regime activation energy of 28 meV is difficult to assign to a specific peak, according to published reports. In this energy range, for low sample temperatures, higher order optical phonon replicas related to the Si D^0X states may comprise part or all of "P1". Additionally, the x-ray diffraction data presented in the previous chapter exhibited some evidence of a weak diffraction peak at a slightly lower angle than the two AlGaN phases, so a small-area third phase with slightly lower mole fraction may be present here. Fortunately, the curve fitting is good, despite treating the "P1" peak structure as a single peak. Although there was a tendency of this peak to decrease slightly towards the free surface, relative to the phases "P2" and "P3" (see Figure 8.5), the intensity was largely unchanged with position across each piece. Since this peak appears to be relatively constant in energy and intensity with spatial location, we can defer discussing its precise origin since it does not correlate with the electrical properties of the diodes.

The "X" peak at 4.31 eV may be related to the free exciton transition in the higher mole fraction phase of AlGaN. In this AlGaN phase, the Si D^0X transition is observed at approximately 4.28 eV. According to one report, an energy separation of 30 meV between the Si level and conduction edge was observed for high mole fraction AlGaN, which is consistent with the observed energy difference.[211] As with the "P1" transition,

this peak does not correlate with the diode electrical properties, so we use it only to estimate the band gap of the higher phase (~4.31 eV). The increase in "X" for beam energies less than 4 keV (see Figures 8.5 and 8.8) is consistent with the decrease in defect emission (e.g., "D", "P1", and "S") for these beam energies, which implies the increase is attributable to a decrease in competitive recombination from these defects. Also, the band gap of the lower phase can be estimated at 30 meV above the "P2" Si D^0X transition at 4.22 eV, implying a band gap of 4.25 eV. This peak is not attainable through curve fitting due to the much larger signal from the D^0X transition, which obscures the much smaller peak.

The common high temperature activation energy (~150 meV) for both "D" and "S" suggests a similar origin for both peaks, although the depth and spatial dependences are different. Since the plasma process creates additional "D" defects in the near-surface region, an obvious candidate is a vacancy in the AlGaN. Ga vacancies are deep acceptors in GaN, at ~1 eV above the valence edge, and this separation increases upon alloying with Al.[212] Al also acts as a deep acceptor in AlGaN.[213] No evidence of luminescence transitions to such states is observed in the present study. Previous investigations on GaN have shown a preferential decrease in nitrogen surface composition relative to gallium, after treatment with Cl_2 and BCl_3 dry etching chemistries. Moreover, gallium vacancy-interstitial pairs have been shown to recombine at room temperature, resulting in an excess of nitrogen vancancies.[214] Again, the lack of deep level emission in the luminescence data suggests the absence of significant quantities of group-III vacancies here.

The nitrogen vacancy is a relatively shallow donor in AlGaN alloys. Nepal et al. have found the V_N level to vary from 30 to 260 meV from GaN to AlN.[215] Interpolation of these endpoints to the present alloy give the level of V_N to be ~130 meV below the conduction edge. Here, it is speculated that both the "D" and "S" peaks are *most likely* associated the lower mole fraction AlGaN phase, with an inferred band gap of 4.25 eV (see above). There may be analogous transitions associated with higher mole fraction phase, but these energies should overlap more with the large "P2" peak and make de-convolution difficult. It is unlikely that "D" and "S" are associated with the higher mole fraction phase, since analogous transitions for the lower mole fraction phase at energies *lower* than "D" and "S" would likely also be observed. Such transitions are absent from the data.

The assignment of the "D" peak at 4.05 eV to V_N is attractive because the ICP surface treatment results in an increase in this peak, which makes sense in the context of the point defects created by the plasma. That is, alternative explanations for the emission, such as donor-acceptor pair recombination and oxygen incorporation can not be accounted for as easily as the production of a vacancy, particularly when the peak position and E_A values are in fair agreement with measured values for V_N in AlGaN seen in the literature. Indeed, the main plasma-induced defect reported in GaN and AlGaN is the nitrogen vacancy. As noted above, evidence of the Ga vacancy, which has previously been reported at ~2.8 eV in comparable mole fraction AlGaN photoluminescence studies, is absent in the present data.

An additional implication of the nitrogen vacancy assignment is that this defect was present in the as-grown material. This is inferred from the "D" peak as-grown

possessing the same energy as the plasma-created peak in the near-surface region. This suggests that the V_N defect is present as-grown and is stable thermally, at least for higher mole fractions. The data in Ref. 214 suggest V_N is thermally stable, although the opposite viewpoint has been suggested in recent reports for low Al mole fraction AlGaN.[216] The removal of "D" with the flowing N_2 RTA process after the ICP step is consistent with restoration of surface nitrogen concentration under similar BCl_3 etching conditions studied in Ref. 197 for GaN. In that study, the surface nitrogen composition, as measured with x-ray photoelectron spectroscopy, was 17.2% pre-etch, 11.1% after plasma etch, and 16.3% post-N_2 RTA. The behavior of the near-surface "D" concentration here, i.e., absent with the HCl sample, present in the ICP case, and absent with the RTA process, is highly consistent with Ref. 197 and gives additional evidence for the V_N assignment.

The "S" peak at ~4.09 eV may also be related to V_N, given the similarity of the high temperature activation energies. The difference in energy between the "D" and "S" emissions, despite a common origin, may be related to different complexing configurations in the material. The removal of this peak after ICP may be a result of disorder favoring a single complex, thereby converting the defects to the new energy. Alternatively, the peak energy of V_N may be shifted in the vicinity of the boundary between the two principal phases. In particular, small strain effects may result in the different V_N energies for the center of the phase and near this boundary.

An alternate explanation for the 4.09 eV peak may be a near-surface defect, which is ablated away with the 300Å ICP etch. This view is supported by the lack of the "S" emission in both of the ICP treated samples. In addition to the nitrogen vacancy

assignment, unintentional incorporation of oxygen, a common impurity in III-N alloys, is possible. Oxygen is a shallow donor in the form O_N through Al mole fractions of 30%, after which the energy level becomes deep in the AlGaN band gap due to a transition similar to Si DX-centers commonly observed in GaAs.[217] The present mole fraction is in the transitional region, and from Ref. 217 the oxygen level can be estimated as 150 meV for x~42%. This is close to the observed value of 4.08 eV, which is 170 meV away from the band gap of 4.25 eV. O_N is not likely for the "D" peak, since it is not clear how the plasma would create significant increases in this impurity. Moreover, this emission is completely absent in the ICP + RTA case, which is difficult to explain since oxygen is not removed from AlGaN even for anneals at 1300 °C (versus 850 °C for the RTA process used here).[218] Note the V_N assignment is consistent for "D", since this defect can be removed at 400 ºC. [219]

The implication for the assignments of "D" and "S" for the observed electrical behavior will be discussion in Section 8.7. Other candidates for the 4.05 and 4.08 eV emissions are briefly discussed here. Si donors, which may be incorporated unintentionally in III-N alloys[220], are accounted for in the assignment of "P2" and "P3" to Si-related excitonic luminescence. Moreover, the spatial and depth dependences of "S" and "D", respectively, are independent of the relatively constant "P2" and "P3" peaks across the AlGaN pieces. Silicon and related complexes can therefore be discounted. The assignment of the "S" and "D" peaks could be attributable to acceptor-bound excitonic or donor-acceptor pair transitions. Possible intentional acceptors that may be present in the MBE chamber are Mg and Be, and a common unintentional acceptor is C. It is difficult to explain why Mg and Be would increase with plasma, so these impurities

can be discounted. Carbon is also unlikely to account for "D", since this emission completely disappears with the RTA process. On the other hand, carbon could be non-uniformly distributed across the HCl-etched surface, and account for "S". This assignment is difficult to reconcile with the electrical characteristics, however, as discussed below.

Figure 8.13 shows an energy level diagram which summarizes the assignment of all peaks discussed above. Based on these assignments, the correlation with diode behavior is now discussed.

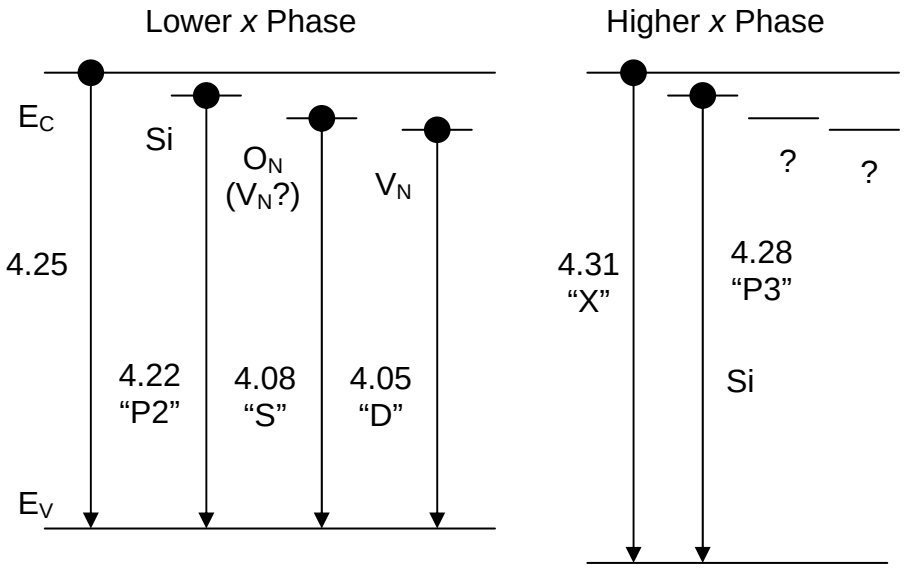

Figure 8.13. Diagram of energy states of all peaks discussed in Section 8.6. The energy units are electron volts. The 4.25 eV band gap for the lower phase and the two lowest energy states for the higher phase are speculative and not observed due to curve fitting limitations (see text). Not shown: "P1".

8.7 Discussion of peak origins and correlation with diode behavior

In the spatially-dependent curve fitting, the "P1", "P2", "P3", and "X" peaks exhibit similar integrated intensities for all positions and for all surface treatments. This implies that the large changes in barrier behavior both across a given piece (e.g., the HCl case) and between the three cases are not due to these emissions. Furthermore, the absence of significant changes in the "P2" and "P3" peaks, in particular, implies that there is no significant variation in Si doping level spatially, which would affect the diodes through image force lowering and competing transport phenomena. Most likely, the variance in the "S" and "D" peaks dominates the diode behavior.

Assuming the "D" peak is nitrogen vacancy-related and the "S" peak is related to the nitrogen vacancy or oxygen impurity, a straightforward model is proposed for the diode electrical behavior. Schottky barriers on GaN have been shown to pin at 0.5-0.6 eV after Cl_2 plasma and other surface treatments.[196,198] In Ref. 196, x-ray photoelectron studies of surface stoichiometry revealed a deficiency of nitrogen post-plasma processing, suggesting that the pinning defect is V_N. Evidently, the surface energy of V_N in the bandgap is ~0.5-0.6 eV below the conduction edge. Hashizume and Hasegawa calculated that for x=30% AlGaN, the Fermi level could be pinned 1.0 eV below the conduction edge for V_N and continuum bandgap states densities of $>10^{12}$ $cm^{-2}eV^{-1}$. The data shown in Chapter 7 for the ICP-prepared surface indicate pinning for all metals near 1 eV with interface state densities as high as 10^{14} $cm^{-2}eV^{-1}$ (as derived from the S-factor value of 0.05). The tightly grouped I-V characteristic for all diodes is in good agreement with the uniform cathodoluminescence spectra. In particular, the spatial variation of the "D" peak, now attributed to V_N, is small. The electrical and luminescence data are

therefore in good agreement, and suggest that Fermi level pinning due to high densities of plasma-created nitrogen vacancies result in consistent barrier heights of ~1.0 eV across the piece.

Similarly, the presence of the "S" peak in the HCl treated surface correlates with adjacent diodes exhibiting a single, dominant barrier height near 1.0 eV, as suggested in Figures 7.15, 7.16, and 8-10. This is further evidence that "S" and "D" behave similarly in all respects and are likely very similar structurally. Again, the nitrogen vacancy related defect resulting in the "S" peak also causes pinning at the AlGaN surface near 1.0 eV and results in the dominant barrier at that energy. Alternatively, if the "S" peak is due to unintentional incorporation of oxygen, which acts as a donor, the decrease in barrier height could be due to an enhancement of n-type doping near the metal-semiconductor interface. This doping enhancement can result in a transition from thermionic transport to thermionic-field emission, as shown in Figure 6.2. The latter transport mechanism results from the increased near-surface band bending, resulting in a thinned potential barrier through which carriers can tunnel, for energies less than the barrier height. In either case, the presence of "S" correlates with the presence of a lowered diode barrier height relative to diodes in regions without "S". The nitrogen vacancy assignment suggests this is due to pinning, as in the ICP-etched case, and the oxygen assignment suggests enhanced surface doping. The assignment of "S" to an unintentional acceptor (e.g., carbon) is also possible from the peak energy. This assignment is unattractive, however, since the presence of a deep acceptor in the near-surface region would result in upward band-bending at the metal interface from pinning effects. This would result in increased barrier heights, rather than the observed decrease. Moreover, the compensating

effects from acceptors would result in a widened depletion region, which would not be favorable for tunneling-assisted transport through the barrier. The acceptor assignment is therefore inconsistent with the observed electrical data.

The ICP + RTA surface treatment sample does not exhibit either of the two peaks observed in the other samples. Notably, this sample exhibits the best barriers, in terms of ideality factors, slope of the S-plot of the primary barrier height, and the least frequent occurrence of the ~1.0 eV barrier (although this barrier is still present with a reduced effect on the I-V characteristics). The near-surface "S" peak is absent (or below the detection limit) since the top 300Å was ablated away during the ICP etch. As for the removal of the "D" emission, fifteen minute annealing at comparatively low temperatures (<400 ºC) has been shown to significantly reduce the nitrogen vacancy (i.e., "D" peak) concentration intentionally introduced via ~10 keV proton irradiation in 60% Al content material.[219] Presumably, the RTA procedure employed in the present study has the same effect on the V_N related states. Alternatively, the N_2 ambient used during the RTA process restores the nitrogen that was permanently lost from the near-surface during the ICP procedure. Such compositional restoration of surface nitrogen has been reported in Ref. 197. Providing the former explanation is true, it is unclear why the post-ohmic RTA in the HCl prepared sample does not quench the defects in a similar fashion prior to Schottky barrier deposition. Lattice disorder introduced by the plasma process may provide a sufficient catalyst for efficient re-ordering of the defect complexes during annealing. In any event, the small, remaining presence of the ~1 eV barrier in the ICP +RTA may be indicative of continued surface pinning effects from residual near-surface vacancies, whereas the vacancies deep in the bulk recombine efficiently. Presumably,

near-surface nitrogen vacancies can not be replenished due to the permanent loss of nitrogen noted in elemental composition studies.[174,197,199] These remaining near-surface defects may be below the detectable limit of our instrumentation for the beam currents and spectral resolution employed.

8.8 Cathodoluminescence and reverse currents

Much attention has been focused on the anomalous leakage currents commonly seen in GaN and AlGaN. These currents exceed expected values, based on forward I-V barrier heights, often by a large amount.[221] Moreover, there is generally no correlation observed between forward barrier height and reverse currents.[222] This trend is noted in the present study with regards to variation in forward and reverse currents across the surface of the HCl prepared sample. The clear trend noted here is the increase of leakage currents for all metal by up to an order of magnitude for the ICP treated cases, versus the HCl treated case. There is direct experimental evidence that the leakage pathways are related to spatially small (diameter <100 nm) screw dislocations and other extended defects. Additionally, these defects are expected to be non-radiative and suppressible by surface oxidation, which forms a blocking layer between the conductive dislocation and the metal.[222,223] Furthermore, there is direct evidence in published reports that plasma processes significantly reduce surface oxygen content, as one might expect.[224]

Some evidence of these leakage pathways *is* suggested from the cathodoluminescence data. Specifically, the reduction of near-surface total luminescence intensity in Figure 8.6 may result from the presence of such non-radiative extended defects. The analysis used to generate Figure 8.6 involved taking the ratio of the ICP

intensites to that of the HCl piece. It may be the case that the apparent reduction shown in the figure arises from comparison of different volumes of the sample. That is, the ICP removal of the top 300Å may reveal the ends of the dislocations, which were previously buried. Once exposed, they act as recombination centers and cause a decrease in the radative efficiency. For large beam energies, approximately the same as-grown depth comprises the excitation volume, so the ratio approached unity. The presence of a top layer with different properties compared to the bulk sample has already been suggested by the depth dependence and spatial uniformity experiments discussed previously. It is not unreasonable to speculate this top layer may be oxygen-terminated from cumulative air exposure, and therefore suppresses the leakage currents. Removal of this layer via the plasma etch results in degraded leakage currents for both ICP cases. Not suprisingly, the addition of the RTA following the ICP has no appreciable effect in reducing the density of such screw dislocations. These defects have been previously shown to be resistant to similar thermal processes, for GaN.[225] This explanation helps explain why the thermal quenching of total luminescence is restored for the ICP + RTA case (compared with the HCl case), but the depth dependence of intensity falloff is not. In other words, the different thermal activation behavior for the ICP-only case is governed by point defects, which are annihilated with the RTA, whereas the extended dislocations are always present.

A diagram of the spatial- and depth-distributions of “D”, “S”, and the proposed screw dislocations is shown in Figure 8.14 for all three surface treatments.

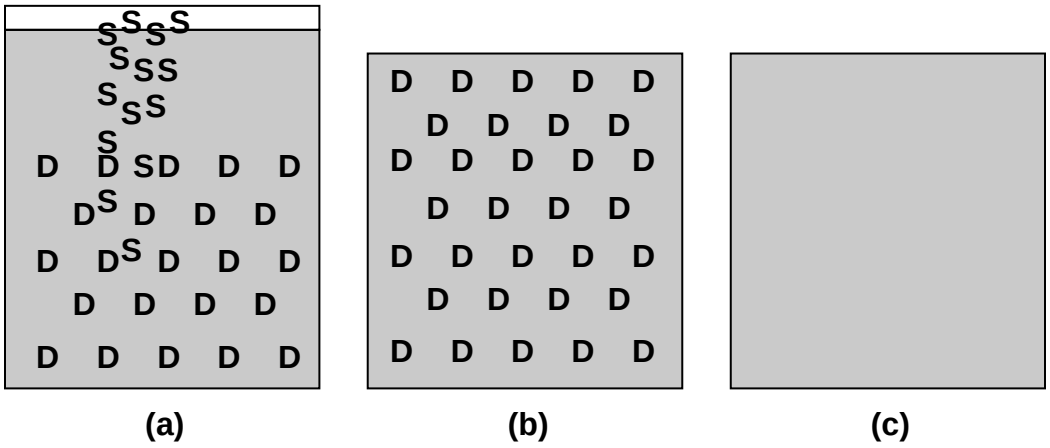

Figure 8.14. Schematic of defect distributions for (a) the HCl etched surface, (b) the ICP etched surface, and (c) the ICP+RTA treatment, with the latter two cases reflecting the ablation of 300Å from the ICP process. The distributions of "D" and "S" are consistent with the depth and spatial dependence of the CLS data. "D" is most likely V_N related. "S" is most likely V_N or O_N related. Regions with "D" or "S" near the surface always exhibit diodes with a dominant secondary barrier near 1.0 eV. The shaded regions correspond to regions that may contain screw dislocations, resulting in high leakage currents. (Not drawn to scale.)

8.9 Summary

Cathodoluminescence spectroscopy has been used as a function of depth and position for all three surface treatment cases presented in Chapter 7. It was shown that two separate, possibly related, peaks correlate with the electrical properties of the diodes. Specifically, the intensity of either of these two defects, which share similar peak positions and thermal activation properties, correlates with the appearance of the second barrier in the Schottky diodes near 1.0 eV. This result is metal-independent and likely results from surface Fermi-level pinning and/or doping variations. The most probable candidate for the "D" peak is the nitrogen vacancy and its complexes. This is considered more likely than acceptor-related emission or unintentional oxygen incorporation due to

the formation of this point defect with plasma treatment and the complete removal of this peak for the ICP + RTA process. The "S" peak correlates with the onset of a prominent second barrier, also near 1.0 eV, for the HCl-etched sample. Probable candidates for this peak include nitrogen vacancies and an oxygen impurity. In the former case, the pinning mechanism outlined above would result in the variation in barrier properties. For the latter scenario, increased n-type doping near the surface of the AlGaN results in an effective lowering of barrier height due to thermionic-field emission. The addition of the RTA anneal post-ICP etching completely eliminates both radiative signatures, and this correlates with the best diode behavior in terms of ideally factors, s-plot slope, and minimized presence of the secondary barrier effects. The elimination of these peaks was attributed to (1) the ICP ablation of material nearest the original surface, which contains "S", and (2) the thermal annealing of the nitrogen vacancy, which has been assigned to "D".

Lastly, the relative decrease in radiative efficiency for the two ICP processes may indicate that non-radiative screw dislocations are revealed after the concealing top layer is physically ablated by the plasma process. These dislocations directly control leakage current, which has been shown in the literature to be independent of metal and forward Schottky barrier heights.

CHAPTER 9

SUMMARY AND FUTURE WORK

9.1 Summary of all results

The goal of this study has been to characterize changes in material and device parameters versus processing and irradiation conditions. Changes in material parameters such as effective doping, interface trap density, the presence of point and extended defects, and impurities were shown to affect devices subjected to ionizing and particle irradiation, as well as precise fabrication procedure. Notable device changes included degradation or enhancement of ohmic contact resistance, total resistance, channel transport properties, transistor saturation currents and transconductance figures, and Schottky barrier heights. Cathodoluminescence spectroscopy was used to directly identify the physical mechanisms responsible for the changes in performance of devices and test structures.

In Chapter 3, the spatial resolution of cathodoluminescence was used to identify localized defects at MOS interfaces. The relative changes of these defects were identified after ionizing irradiation. The changes could be identified at both the metal and semiconductor interfaces by localized the electron beam there. Comparison of the emission energies with literature reports of the physical origin of the defects allowed for mechanisms to be proposed, that accounted for the spectral changes.

In Chapters 4 and 5, radiation effects were continued. In these cases, the III-nitride system was studied. In addition to this material system being extensively studied presently, GaN and alloys are highly compatible with cathodoluminescence. Such materials are highly luminescent and resistant to degradation with cumulative electron beam exposure. More importantly, compared with Si devices, much less is known about irradiation effects on nitrides. Although generally assumed radiation tolerant compared to other materials, changes in device performance are clearly noted, particularly with the electrical contacts of the device. Using the depth-dependence of cathodoluminescence to probe through the HEMT layers, mechanisms were suggested for the electrical degradation. The presence of new defects and degraded band edge luminescence was accompanied by SIMS scans indicating the emergence of an intermixed interface.

Chapter 6 demonstrated the sensitivity of the electrical contacts of a device to irradiation effects. Indeed, GaN had typically been assumed to be radiation tolerant to proton fluence ~100 times greater than where the Schottky contact was shown to degrade. The decrease in barrier height observed has important implications for the high frequency behavior of HEMTs, which relies on Schottky gates with low leakage current. Moreover, the changes in Schottky barrier noted suggested the work in the final two chapters, where processing, rather than irradiation, was first considered.

In Chapter 7, the effects of pre-metallization surface processing on Schottky barrier performance was noted for numerous metals. The ICP processing treatments were highly relevant for gate-recess technology. For comparing several metals with a spread of workfunctions, interface state densities can be inferred. It was found that this density decreased by a factor of about ten with the addition of the RTA step immediately

following the ICP etch (but prior to the metallization). This reduction manifested the change of forward I-V performance from a highly pinned surface, with each metal exhibiting the same barrier height of ~1.0 eV, to an unpinned surface with the interface index S=0.3. Each of the ICP etch cases showed more uniform barrier performance than the HCl case, which exhibited large scatter in the I-V curves, largely independent of metal.

The cathodoluminescence studies described in Chapter 8 were complementary with the I-V diode behavior shown in Chapter 7. Several luminescent emissions were noted for each processing case. Most of the peaks were unaffected by processing and showed similar depth dependence. In particular, the two main peaks were attributed to two different AlGaN phases, which were similar in mole fraction and safely ignored for the barrier height study. The two peaks that did show depth and spatial dependence exhibited similar temperature dependence, and were tentatively assigned to the same physical origin. The most probable defect associated with these peaks is the nitrogen vacancy, which is present as-grown and created by ICP. The resulting barrier heights for all diodes deposited near regions containing either peak give barrier heights consistent with the surface energy of this defect in the AlGaN bandgap (~1.0 eV). Regions in all samples without these peaks show the best-behaved barriers, exhibiting a minimal contribution from the 1.0 eV barrier (from thermionic fits of the I-V data). In particular, the ICP + RTA sample consistently gave well-behaved barriers, while both peaks were always absent for all spatial positions. Conversely, the ICP (only) case always showed the "D" peak in the spectra, and all diodes fabricated on that piece showed a large contribution form the lower barrier diode. Additionally, the presence of decreased

luminescence in the near-surface region of both ICP-etched samples gave evidence for the presence of a non-radiative state near the metal-semiconductor interface. Both of the ICP-etched samples also exhibit increased leakage currents for all metals. These two factors, taken together, suggest the presence of extended defects, such as screw dislocations, which are known to affect leakage currents and radiative efficiency in AlGaN.[222]

9.2 Future work

Based on the current direction of the project, a list of future projects is proposed below for AlGaN. As noted in Chapter 7, the has been a great deal of scatter reported in the literature for Schottky contacts on GaN, and the situation becomes worse for AlGaN, where oxygen incorporation and phase separation are additionally present. The process-induced changes to barrier heights and subsequent thermal stability are open questions. All projects involve future studies of Schottky barriers, so a suitable photolithography procedure would be advantageous. For example, a "guard ring" geometry would be helpful for minimizing series resistance, which was a large problem in the present study, precluding accurate C-V and complementary DLTS measurements. Also, suitably small diodes would allow for high frequency measurements, which should be highly sensitive to interface and bulk traps.[226] Diodes with varying ratios of perimeter to surface area would allow for discrimination of peripheral conduction from the rest of the diode area. Lastly, SIMS, which due to downtime was not available for this study, could help clarify the roles of impurity defects and interface oxide effects, if present. Additionally, this

technique would be very useful in identifying intermixing effects, such as shown in Chapter 5, between the metal and AlGaN with low temperature annealing.

The main studies proposed are as follows:

(1) SIMS studies to clarify the role of oxygen in the diode behavior. In particular, such studies could confirm the assignment of "S" to oxygen by comparing several diodes or regions across the HCl piece. Preliminary SIMS scans showed small signals of both oxygen and the primary dopant (Si). Equipment scheduling and downtime precluded subsequent scans up to the point of this report.

(2) Repeat study in Chapters 7 and 8 for a selective Si_3N_4 (or other passivation) etch. In addition to gate recess etches, there is much interest in this process for electron beam lithography of HEMT gates. Since the AlGaN is not etched in this case, a comparison could be made with the present study in terms of interface state density and the occurrence of point defects.

(3) Investigation of barrier heights versus BCl_3 etch power conditions. This is the etch used in this study, and the AlGaN is ablated. A comparison of the resulting interface index (i.e., slope, S, on the barrier height versus workfunction plot) may indicate a preferred power threshold for the creation of a large density of interface states and surface pinning. Specifically, the creation of large amounts of nitrogen vacancies may be suppressed.

(4) Determination of maximum annealing temperatures for all metals versus processing condition. The 400 ºC figure used in Chapter 7 was suggested by the determination of channel temperature for 5 a W/mm power density. Record

continuous power densities are >12 W/mm, suggesting the channel temperatures may be much higher. Failure of Schottky contacts (versus the general *improvement* noted here) could be accounted for using SIMS to clarify intermixing effects.

(5) Proton irradiation effects of Schottky barrier on n-AlGaN. Very little has been reported here, and some metals may be more susceptible to irradiation damage than others, due to intermixing and interface states. Moreover, for suitably prepared surfaces exhibiting reasonable interface indices, the change in this value with irradiation would give a direct measure of the density of interface states. High frequency measurements would also be useful here to establish how this quantity degrades.

(6) Schottky barriers on p-type AlGaN are poorly understood with a large spread in reported values. For suitably high material quality, different surface preparations may help give reliable barriers. Most likely, a suitably low power plasma treatment would be required to avoid the formation of excessive compensating nitrogen vacancies.

LIST OF REFERENCES

[1] S. Nakamura, M. Senoh, and T. Mukai, Jap. Jour. Appl. Phys. 30, L1708 (1991).

[2] J. M. Hayes, M. Kuball, A. Bell, I. Harrison, D. Korakakis, and C. T. Foxon, Appl. Phys. Lett. 75, 2097 (1999).

[3] C. Li and S. Subramamian, IEEE Trans. Nucl. Sci. 50, 1998 (2003).

[4] B. D. White, M. Bataiev, S. H. Goss, X. Hu, A. Karmarkar, D. M. Fleetwood, R. D. Schrimpf, W. J. Schaff, and L. J. Brillson, IEEE Trans. Nucl. Sci. 50, 1934 (2003).

[5] J. K. Sheu and G. C. Chi, Jour. Phys.: Cond. Matt. 14, R657 (2002).

[6] J. Hwang, W. J. Schaff, L .F. Eastman, S. T. Bradley, L. J. Brillson, D. C. Look, J. Wu, W. Walukiewitz, M. Furis, and A. N. Cartwright, Appl. Phys. Lett. 81, 5192 (2002).

[7] S. J. Pearton, F. Ren, A. P. Zhang, and K. P. Lee, Mat. Sci. and Eng. R30, 55-212 (2000).

[8] W. Liu, Fundamentals of III-V Devices, (Wiley, New York, 1999).

[9] C. Lee, W. Lu, E. Piner, and I. Adesida, Sol.-State Elec. 46, 743 (2002).

[10] K. F. Brennan and A. S. Brown, Theory of Modern Electronic Semiconductor Devices, (Wiley, New York, 2002).

[11] L. F. Eastman, V. Tilak, J. Smart, B. M. Green, E. M. Chumbes, R. Dimitrov, H. Kim, O. S. Ambacher, N. Weimann, T. Prunty, M. Murphy, W. J. Schaff, and J. R. Shealy, IEEE Trans. Elec. Dev. 48, 479 (2001).

[12] D.F. Storm, D.S. Katzer, S.C. Binari, B.V. Shanabrook, X. Xu, D.S. McVey, R.P. Vaudo and G.R. Brandes, Elec. Lett. 40, 1226 (2004).

[13] J. Hilsenbeck, E. Nebauer, J. Wurfl, G. Trankle and H. Obloh, Elec. Lett. 36, 980 (2000).

[14] T. Hashizume, J. Kotani, and H. Hasegawa, Appl. Phys. Lett. 84, 4884 (2004).

[15] C. Sanabria, A. Chakraborty, H. Xu, M.J. Rodwell, U.K. Mishra, and R.A. York, IEEE. Elec. Dev. Lett. 27, 19 (2006).

[16] D.M. Fleetwood, P.S. Winokur, and P.E. Dodd, Microelectron. Rel. 40, 17 (2000).

[17] A.L. Vampola, IEEE Trans. Nucl. Sci. 28, 1831 (2000).

[18] H. Boudinov, S. O. Kucheyev, J. S. Williams, C. Jagadish, and G. Li, Appl. Phys. Lett. 78, 943 (2001).

[19] F. Gaudreau, P. Fournier, C. Carlone, S.M. Khanna, H. Tang, J. Webb, and A. Houdayer, IEEE Trans. Nucl. Sci. 49, 2702 (2002).

[20] S. Arulkumaran, T. Egawa, H. Ishikawa, and T. Jimbo, Appl. Phys. Lett. 81, 3073 (2002).

[21] A. Curutchet, N. Malbert, N. Labat, A. Touboul, C. Gaquiere, A. Minko, and M. Uren, Microelectron. Rel. 43, 1713 (2003).

[22] J.M. Tirado, J.L. Sanchez-Rojas, and J.I. Izpura, Semicond. Sci. Tech. 20, 864 (2005).

[23] D. Crowe and A. Feinberg, eds., Design for Reliability, (CRC, New York, 2001).

[24] L.J. Brillson, Jour. Vac. Sci. and Tech. B 19, 1762 (2001).

[25] T. Everhart and P. Hoff, Jour. Appl. Phys. 42, 5837 (1971).

[26] C. Klein, Jour. Appl. Phys. 39, 2029 (1968).

[27] S. Davidson and C. Dimitriadis, Jour. Micros. 118, 275 (1980).

[28] S.T. Bradley, S.H. Goss, J. Hwang, W.J. Schaff, L.J. Brillson, Appl. Phys. Lett. 85, 1368 (2004).

[29] G.H. Jessen, B.D. White, S.T. Bradley, P.E. Smith, L.J. Brillson, J.E. Van Nostrand, R. Fitch, G.D. Via, J.K. Gillespie, R.W. Dettmer, J.S. Sewell, Sol.-State Elec. 46, 1427 (2002).

[30] L.J. Brillson, Jour. Vac. Sci. Technol. B 19, 1762 (2001).

[31] http://www.gel.usherb.ca/casino/

[32] S.T. Bradley, S.H. Goss, L.J. Brillson, J. Hwang, and W.J. Schaff, Jour. Vac. Sci. Technol. B 21, 2558 (2003).

[33] J. Schäfer, A.P. Young, L.J. Brillson, H. Niimi, and G. Lucovsky, Appl. Phys. Lett. 73, 791 (1998).

[34] S.H.Goss, X.L. Sun, A.P. Young, L.J. Brillson, D.C. Look, and R.J. Molnar, Appl. Phys. Lett. 78, 3630 (2001).

[35] M.A. Stevens Kalceff and M.R. Phillips, Phys. Rev. 52, 3122 (1995).

[36] D.L. Griscom, J. Ceram. Soc. Jpn. 99, 923 (1991).

[37] D.L. Griscom, J. Crystal. Solids 40, 211 (1980).

[38] P.M. Lenahan and J.F. Conley, Jr., J. Vac. Sci. Technol. B 16, 2134 (1998).

[39] P.M. Lenahan and P.V. Dressendorfer, J. Appl. Phys. 55, 3495 (1984).

[40] T.D. Mishima and P. M. Lenahan, IEEE Trans. Nucl. Sci. 47, 2249 (2000).

[41] L. Canham, Mater. Res. Bull., 18, 22 (1993).

[42] D.R. Lee, C.G. Parker, J. Hauser, and G. Lucovsky, J. Vac. Sci. Technol. B, 1788 (1995).

[43] B.D.White, L.J. Brillson, S.C. Lee, S.C. D.M. Fleetwood, R.D. Schrimpf, S.T. Pantelides, Y.-M. Lee, and G. Lucovsky, IEEE Trans. Nucl. Sci. 47, 2276 (2000).

[44] S.T.Pantelides, S.N. Rashkeev, R. Buczko, D.M.Fleetwood, and R.D. Schrimpf, IEEE Trans. Nucl. Sci. 47, 2262 (2000).

[45] M.A. Stevens Kalceff, G.J. Thorogood, and K.T. Short, J. Appl. Phys., 86, 1 (1999).

[46] J.P. Mitchell and D.G. Denure, Solid-State Electron. 16, 825 (1973).

[47] M.A. Stevens Kalceff, Phys. Rev. 57, 5674 (1998).

[48] D. M. Fleetwood, P. S. Winokur, L. J. Lorence, Jr., W. Beezhold, P. V.Dressendorfer, and J. R. Schwank, IEEE Trans. Nucl. Sci. 33, 1245 (1986).

[49] D. Drouin, A. R. Couture, R. Gauvin, Micr. & Microanal. 7, 684 (2001).

[50] T.E. Everhart and P.H. Hoff, J. Appl. Phys. 42, 5837 (1971).

[51] S.W. McKnight and E.D. Palik, J. Non-Cryst. Sol. 40, 595 (1980).

[52] L.N.Skuja, A.R.Silin, and A.G.Boganov, J. Non-Cryst. Solids, 63, 431 (1984).

[53] R.A. Weeks, J. Appl. Phys. 27, 1376 (1956).

[54] F.J. Feigl, W. B. Fowler, and K.L. Yip, Sol. State Commun. 14, 225 (1974).

[55] L. Skuja, J. Non-Crystall. Solids 239, 16 (1998).

[56] S.W. McKnight and E.D. Palik, J. Non-Crystall. Solids 40, 595 (1980).

[57] L.N. Skuja and W. Entzian, Phys. Stat. Sol. (a) 96, 191 (1986).

[58] D.L. Griscom and E.J. Friebele, Phys. Rev. B 24, 2896 (1982).

[59] H. Koyama, J. Appl. Phys. 51, 2228 (1080).

[60] C. Itoh, T. Suzuki, and N. Itoh, Phys. Rev. B 41, 3794 (1990).

[61] G.H. Sigel Jr. and M.J. Marrone, J. Non-Cryst. Sol. 45, 235(1981).

[62] G.H. Sigel, Jr., E.J. Friebele, R.J. Ginther, and D.L. Griscom, IEEE Trans. Nucl. Sci. 21, 56 (1974).

[63] D.L. Griscom, J. Appl. Phys. 80, 2142 (1996).

[64] R. A. B. Devine, D. Mathiot, W. L. Warren, D. M. Fleetwood, and B. Aspar, Appl. Phys. Lett. 63, 2926 (1993).

[65] D. M. Fleetwood, R. A. Reber, Jr., and P. S. Winokur, IEEE Trans. Nucl. Sci. 38, 1066 (1991).

[66] T. Jung and W. Titel, Phys. Stat. Sol. (a) 74, 85 (1982).

[67] Y.E. Strausser and K.S. Majumder, J. Vac. Sci. Technol. 15, 238 (1978).

[68] L.J. Brillson, Phys. Rev. Lett. 40, 260 (1978).

[69]S. J. Cai, Y. S. Tang, R. Li, Y. Wei, L. Wong, Y. L. Chen, K. L. Wang, Mary Chen, Y. F. Zhao, R. D. Schrimpf, J. C. Keay, and K. F. Galloway, IEEE Trans. Elec. Dev. 47, 304 (2000).

[70] B. Luo, J. W. Johnson, F. Ren, K. K. Allums, C. R. Abernathy, S. J. Pearton, R. Dwivedi, T. N. Fogarty, R. Wilkins, A. M. Dabiran, A. M. Wowchack, C. J. Polley, P. P. Chow, and A. G. Baca, Appl. Phys. Lett. 79, 2196 (2001).

[71] B. Luo, J. W. Johnson, F. Ren, K. K. Allums, C. R. Abernathy, S. J. Pearton, R. Dwivedi, T. N. Fogarty, R. Wilkins, A. M. Dabiran, A. M. Wowchack, C. J. Polley, P. P. Chow, and A. G. Baca, Jour. Elec. Mater. 31, 437 (2002).

[72] S. M. Khanna, J. Webb, H. Tang, A. J. Houdayer, and C. Carlone, IEEE Trans. Nucl. Sci. 47, 2322 (2000).

[73] V. V. Emtsev, V. Y. Davydov, E. E. Haller, A. A. Klochikhin, V. V. Kozlovskii, G. A. Oganesyan, D. S. Poloskin, N. M. Shmidt, V. A. Vekshin, and A. S. Usikov, Physica B 308-310, 58 (2001).

[74] S. A. Goodman, F. D. Auret, F. K. Koschnick, J.-M. Spaeth, B. Beaumont, and P. Gibart, Mat. Sci & Eng. B 71, 100 (2000).

[75] F. D. Auret, S. A. Goodman, M. Hayes, M. J. Legodi, S. S. Hullavarad, E. Friedland, B. Beaumont, and P. Gibart, Nucl. Inst. & Meth. Phys. Res. B 175-177, 292 (2001).

[76] M. J. Legodi, S. S. Hullavarad, S. A. Goodman, M. Hayes and F. D. Auret, Physica B 308-310, 1189 (2001).

[77] G. A. Umana-Membreno, J. M. Dell, T. P. Hessler, B. D. Nener, G. Parish, L. Faraone, and U. K. Mishra, Appl. Phys. Lett. 80, 4354 (2002).

[78] F. Gaudreau, C. Carlone, A. Houdayer, and S. M. Khanna, IEEE Trans. on Nucl. Sci. 48, 1778 (2001).

[79] M. Osinski, P. Perlin, H. Schone, A. H. Paxton, and E.W. Taylor, Elec. Lett. 33, 1252 (1997).

[80] D. Drouin, A. R. Couture, R. Gauvin, Micr. & Microanal. 7, 684 (2001).

[81] A. P. Young, J. Bae, L. J. Brillson, M. J. Murphy, and W. J. Schaff, J. Vac. Sci. Technol. B 18, 2309 (2000).

[82] B. K. Meyer, G. Steude, A. Goldner, A. Hoffmann, H. Amano, I. Akasaki, Phys. Stat. Sol. B 216, 187 (1999).

[83] M. Leroux, N. Grandjean, B. Beaumont, G. Nataf, F. Semond, J. Massies, and P. Gibart, J. Appl. Phys. 86, 3721 (1999).

[84] A. Y. Polyakov, A. S. Usikov, B. Theys, N. B. Smirnov, A. V. Govorkov, F. Jomard, N. M.Shmidt, W. V. Lundin, Solid-State Electron. 44, 1971 (2000).

[85] J. F. Ziegler, J. P. Biersack, U. Littmark, The Stopping and Range of Ions in Solids, 2nd ed., Pergamon Press, New York, 1996.

[86] X. Hu, B. K. Choi, H. J. Barnaby, D. M. Fleetwood, R. D. Schrimpf, S. C. Lee, S. Shojah-Ardalan, R. Wilkins, U. K. Mishra, and R. Dettmer, unpublished.

[87] G. P. Summers, E. A. Burke, M. A. Xapsos, C. J. Dale, P. W. Marshall, and E. L. Petersen, IEEE Trans. on Nucl. Sci. 35, 1221 (1988).

[88] C. Wetzel, T. Takeuchi, H. Amano, and I. Akasaki, J. Appl. Phys. 85, 3786 (1999).

[89] O. Ambacher, J. Majewski, C. Miskys, A. Link, M. Hermann, M. Eickhoff, M. Stutzmann, F. Bernardini, V. Fiorentini, V. Tilak, B. Schaff and L. F. Eastman, J. Phys.: Cond. Matt. 13, 1 (2001).

[90] G. Snider, 1D Poisson Band Diagram Calculator, South Bend, IN, Univ. of Notre Dame Press, available at http://www.nd.edu/~gsnider/

[91] O. Ambacher, B. Foutz, J. Smart, R. Shealy, N. G. Weimann, K. Chu, M. Murphy, A. J. Sierakowski, W. J. Schaff, L. F. Eastman, R. Dimitrov, A. Mitchell, and M. Stutzmann, J. App. Phys. 87, 334 (2001).

[92] D. C. Look, J.W. Hemsky, and J.R. Sizelove, Phys. Rev. Lett. 82 (1999).

[93] Rashmi, A. Kranti, S. Haldar, and R. S. Gupta, Microelectron. Jour. 33, 205 (2002).

[94] L. Polenta, Z.-Q.Fang, and D.C.Look, Appl. Phys. Lett. 76, 2086 (2000).

[95] D. C. Look, D. C. Reynolds, J. W. Hemsky, J. R. Sizelove, R. L. Jones, and R. J. Molnar, Phys. Rev. Lett. 79, 2273 (1997).

[96] D. C. Look, Phys. Stat. Sol. B 228, 293 (2001).

[97] S.M.Khanna, A. Jorio, C. Carlone, M. Parenteau, A. Houdayer, and J.W. Gerdes Jr., IEEE Trans. Nucl. Sci. 42, 2095 (1995).

[98] B. Luo, J. J. Kim, F. Ren, J. K. Gillespie, R. C. Fitch, J. Sewell, R. Dettmer, G. D. Via, A. Crespo, T. J. Jenkins, B. P. Gila, A. H. Onstine, K. K. Alums, C. R. Abernathy, S. J. Pearton, R. Dwivedi, T. N. Fogarty, and R. Wilkins, Appl. Phys. Lett. 82, 1428 (2003).

[99] B. D. White, M. Bataiev, L. J. Brillson, B. K. Choi, D. M. Fleetwood, R. D. Schrimpf, S. T. Panelides, R. W. Dettmer, W. J. Schaff, J. G. Champlain, and U. K. Mishra, IEEE Trans. Nucl. Sci. 49, 2695 (2002).

[100] W. T. Anderson, A. R. Knudson, A. Meulenberg, H.-L. Hung, J. A. Roussos, and G. Kiriakidis, IEEE Trans. Nucl. Sci. 37, 2065 (1990).

[101] D. K. Schroder, Semiconductor Material and Device Characterization, 2nd Ed., Wiley-Interscience, 1999.

[102] Q. Wang, H. Q. Xu, P. Omling, C. Yang, K. G. Malmqvist, Nucl. Intr. Meth. Phys. Res. B 160, 33 (2000).

[103] D. Drouin, A. R. Couture, R. Gauvin, Micr. & Microanal. 7, 684 (2001).

[104] J. F. Ziegler, J. P. Biersack, U. Littmark, The Stopping and Range of Ions in Solids, 2nd ed., Pergamon Press, New York, 1996.

[105] A. Y. Polyakov, A. S. Usikov, B. Theys, N. B. Smirnov, A. V. Govorkov, F. Jomard, N. M.Shmidt, W. V. Lundin, Solid-State Electron. 44, 1971 (2000).

[106] A. Motayed, R. Bathe, M. C. Wood, O. S. Diouf, R. D. Vispute, and S. N. Mohammad, J. Appl. Phys. 93, 1087 (2003).

[107] F. A. Padovani and R. Stratton, Solid-State Electron. 9, 695 (1966).

[108] V. V. Kozlovskii, V. A. Kozlov, and V. N. Lomasov, Semiconductors 34, 123 (2000).

[109] R. R. Sumathi, M. Udhayasankar, J. Kumar, P. Magudapathy, and K. J. M. Nair, Physica B 308-310, 1209 (2001).

[110] R. Oberhuber, G. Zandler, and P. Vogl, Appl. Phys. Lett. 73, 818 (1998).

[111] J. Antoszewski, M. Gracey, J. M. Dell, L. Faraone, T. A. Fisher, G. Parish, Y.-F. Yu, and U. K. Mishra, J. Appl. Phys. 87, 3900 (2000).

[112] Rashmi, A. Kranti, S. Haldar, and R. S. Gupta, Microelectron. Jour. 33, 205 (2002).

[113] M. A. Khan, R. A. Skogman, R. G. Schulze, and M. Gershenzon, Appl. Phys. Lett. 43, 492 (1983).

[114] F. D. Auret, S. A. Goodman, M. Hayes, M. J. Legodi, S. S. Hullavarad, E. Friedland, B. Beaumont, and P. Gibart, Nucl. Inst. & Meth. Phys. Res. B 175-177, 292 (2001).

[115] O. Ambacher, B. Foutz, J. Smart, J. R. Shealy, N. G. Weimann, K. Chu, M. Murphy, A. J. Sierakowski, W. J. Schaff, L. F. Eastman, R. Dimitrov, A. Mitchell, and M. Stutzmann, J. Appl. Phys. 87, 334 (2000).

[116] B.L. Sharma, Metal-Semiconductor Schottky Barrier Junctions and Their Applications, (Plenum, New York, 1984).

[117] E.H. Rhoderick and R.H. Williams, Metal-Semiconductor Contacts, (Clarendon, Oxford, 1988).

[118] F. A. Padovani and R. Stratton, Solid-State Electronics, 9, 695 (1966).

[119] B. D. White, M. Bataiev, S. H. Goss, X. Hu, A. Karmarkar, D. M. Fleetwood, R. D. Schrimpf, W. J. Schaff, and L. J. Brillson, IEEE Transactions on Nuclear Science, 50, 1934 (2003).

[120] D.K. Schroder, Semiconductor Material and Device Characterization, (Wiley-Interscience, New York, 1998).

[121] M. Hayes, F.D. Auret, L. Wu, W.E. Meyer, J.M. Nel and M.J. Legodi, Phys. B 340-342, 421 (2003).

[122] K. K. Ng, "Complete Guide to Semiconductor Devices" 2nd Ed., Wiley, 2002.

[123] S.M. Khanna, D. Estan, L.S. Erhardt, A. Houdayer, C.. Carlone, A. Ionascut-Nedelcescu, S.R. Messenger, R.J. Walters, G.P. Summers, J.H. Warner, and I. Jun, IEEE Trans. Nucl. Sci. 51, 2729 (2004).

[124] X. Hu, B.K. Choi, H.J. Barnaby, D.M. Fleetwood, R.D. Schrimpf, S.C. Lee, S. Shojah-Ardalan, R. Wilkins, U.K. Mishra, and R.W. Dettmer, IEEE Trans. Nucl. Sci. 51, 293 (2004).

[125] S.A. Goodman, F.D. Auret, F.K. Koschnick, J.-M. Spaeth, B. Beaumont and P. Gibart, Mat. Sci. & Eng. B 71, 100 (2000).

[126] T. Mattila, A. P. Seitsonen, and R. M. Nieminen, Phys. Rev. B 54, 1474 (1996).

[127] C. W. Wang, Jour. Vac. Sci. Technol. B 20, 1821 (2002).

[128] M. Linde, S. J. Uftring, G. D. Watkins, V. Harle and F. Scholz, Phys. Rev. B 55, R10177 (1997).

[129] K. H. Chow, G. D. Watkins, A. Usui and M. Mizuta, Phys. Rev. Lett. 85, 2761 (2000).

[130] S.O. Kucheyev, H. Boudinov, J.S. Williams, C. Jagadish, and G. Li, Jour. Appl. Phys. 91, 4117 (2002).

[131] A.P. Karmarkar, B.D. White, D. Buttari, D.M. Fleetwood, R.D. Schrimpf, R.A. Weller, L.J. Brillson, and U.K. Mishra, IEEE Trans. Nucl. Sci. 52, 2239 (2005).

[132] H. H. Tan, J. S. Williams, J. Zou, D. J. H. Cockayne, S. J. Pearton, and R. A. Stall, Appl. Phys. Lett. 69, 2354 (1996).

[133] Q. Zhou, M.O. Manasreh, M. Pophristic, S. Guo, and I.T. Ferguson, Appl. Phys. Lett. 79, 2901 (2001).

[134] Y.-J. Lin, Q. Ker, C.-Y. Ho, H.-C. Chang, and F.-T. Chien, Jour. Appl. Phys. 94, 1819 (2003).

[135] Y.-J. Lin, Y.-M. Chen, T.-J. Cheng, and Q. Ker, Jour. Appl. Phys. 95, 571 (2004).

[136] C.C. Kim, J.K. Kim, J.-L. Lee, M.-S. Yi, J.-W. Kim, D.Y. Noh, Y. Hwu, P. Ruterana, and J.H. Je, GaN and Related Alloys – 2000. Symposium (Mat. Res. Soc. Symposium Proc. V. 639) G11.7.1-6 (2001).

[137] J. Kuzmik, P. Javorka, A. Alam, M. Marso, M. Heuken, and P. Kordos, IEEE Trans. Elec. Dev. 49, 1496 (2002).

[138] S. J. Pearton, F. Ren, A. P. Zhang, and K. P. Lee, Mat. Sci. and Eng. R30, 55 (2000).

[139] Z. Lin, H. Kim, J. Lee, and W. Lu, Appl. Phys. Lett. 84, 1585 (2004).

[140] A. Kuliev, V. Kumar, R. Schwindt, D. Selvanathan, A.M Dabiran, P. Chow, and I. Adesida, IEEE Lester Eastman Conference on High Performance Devices, 428 (2002).

[141] W. K. Wang, P.C. Lin, C.H. Lin, C.K. Lin, Y.J. Chan, G.T. Chen, J.I. Chyi, IEEE Elec. Dev. Lett. 26, 5 (2005)

[142] B.L. Sharma, Metal-Semiconductor Schottky Barrier Junctions and Their Applications, (Plenum, New York, 1984).

[143] S. Kurtin, T.C. McGill, C.A. Mead, Phys. Rev. Lett. 22, 1433 (1969).

[144] J. Rennie, M. Onomura, S. Nunoue, G. Hatakoshi, H. Sugawara, and M. Ishikawa, Jour. Cryst. Growth 189/190, 711 (1998).

[145] S. Arulkumaran, T. Egawa, G.-Y. Zhao, H. Ishikawa, T. Jimbo, and M. Umeno, Jap. Jour. Appl. Phys. 39, L351 (2000).

[146] A.C. Schmitz, A. T. Ping, M.A. Khan, Q. Chen, J. W. Yang, and I. Adesida, Semicond. Sci. and Tech. 11, 1464 (1996).

[147] J. Dumont, E. Monroy, E. Munoz, R. Caudano, and R. Sporken, Jour.Cryst. Growth 230, 558 (2001).

[148] E.H. Rhoderick and R.H. Williams, Metal-Semiconductor Contacts, (Clarendon, Oxford, 1988).

[149] A. M. Cowley and S.M. Sze, Jour. Appl. Phys. 36, 3212 (1965).

[150] K. Suze, S.N. Mohammad, Z.F. Fan, W. Kim, O. Aktas, A.E. Botchkarev, and H. Morkoc, Jour. Appl. Phys. 80, 4467 (1996).

[151] R. Sporken, C. Silien, F. Malengreau, K. Grigorov, R. Caudano, F.J. Sanchez, E. Calleja, E. Munoz, B. Beaumont, and P. Gibart, MRS Internet Jour. of Nitride Semi. Res. 2, (1997).

[152] T. Sawada, Y. Ito, N. Kimura, K. Imai, K. Suzuki, and S. Sakai, Appl. Surf. Sci. 190, 326 (2002).

[153] K.M. Tracy, P.J. Hartlieb, S. Einfeldt, R.F. Davis, E.H. Hurt, and R.J. Nemanich, Jour. Appl. Phys. 94, 3939 (2003).

[154] R. Mehandru, S. Kang, S. Kim, F. Ren, I. Kravchenko, W. Lewis, and S.J. Pearton, Mat. Sci. in Semi. Proc. 7, 95 (2004).

[155] V. Kumar, D. Selvanathan, A. Kuliev, S. Kim, J. Flynn, and I. Adesida, Elec. Lett. 39, 747 (2003).

[156] M.R.H. Khan, H. Nakayama, T. Detchprohm, K. Hiramatsu, and N. Sawaki, Sol.-State Elec. 41, 287 (1997).

[157] L. Zhou, F.A. Khan, G. Cueva, V. Kumar, I. Adesida, M.R. Sardela, Jr., and F.D. Auret, Appl. Phys. Lett. 81, 1624 (2002).

[158] D. Qiao, L.S. Yu, S. S. Lau, J.M. Redwing, J.Y. Lin, and H.X. Jiang, Jour. Appl. Phys. 87, 801 (2000).

[159] Q.Z. Liu, L.S. Ya, S.S. Lau, J.M. Redwing, N.R. Rerkins and T.F. Kuech, Appl. Phys. Lett. 70, 1275 (1997).

[160] J. Wang, D.G. Zhao, Y.P. Sun, L.H. Duan, Y.T. Wang, S.M. Zhang, H. Yang, S. Zhou, and M. Wu, Jour. Phys. D: Appl. Phys. 36, 1018 (2003).

[161] E. Monroy, F. Calle, R. Ranchal, T. Palacios, M. Verdu, F.J. Sanchez, M.T. Montojo, M. Eickhoff, F. Omnes, Z. Bougrioua, and I. Moerman, Semi. Sci. Tech. 17, L47 (2002).

[162] J.S. Foresi and T.D. Moustakas, Appl. Phys. Lett. 62, 2859 (2003).

[163] B.A. Hull, S.E. Mohney, U. Chowdhury, and R.D. Dupuis, Jour. Vac. Sci. Tech. B 22, 654 (2004).

[164] K.J. Duxstad, E. E. Haller, and K.M. Yu, Jour. Appl. Phys. 81, 3134 (1997).

[165] A. Kuliev, V. Kumar, R. Schwindt, D. Selvanathan, A.M Dabiran, P. Chow, and I. Adesida, IEEE Lester Eastman Conference on High Performance Devices, 428 (2002).

[166] V. Kumar, A. Kuliev, T. Tanaka, T. Otoki, and I. Adesida, Elec. Lett. 39, 1758 (2003).

[167] S.A. Campbell, The Science and Engineering of Microelectronic Fabrication (Oxford University Press, Oxford, 2001).

[168] R.J. Shul, G.B. McClellan, S.A. Casalnuovo, D.J. Rieger, S.J. Pearton, C. Constantine, C. Barratt, R.F. Karlicek, Jr., C. Tran, and M. Schurman, Appl. Phys. Lett. 69, 1119 (1996).

[169] S.A. Smith, C.A. Wolden, M.D. Bremser, A.D. Hanser, R.F. Davis, and W.V. Lampert, Appl. Phys. Lett. 71, 3631 (1997).

[170] F.A. Khan, L. Zhou, A.T. Ping, and I. Adesida, Jour. Vac. Sci. & Tech. B 17, 2750 (1999).

[171] J. Nemergut, B.D. White, L.J. Brillson, and I. Adesida, unpublished.

[172] F.A. Khan, L. Zhou, V. Kumar, and I. Adesida, Jour. Vac. Sci. Tech. 19, 2926 (2001).

[173] T. Hashizume and H. Hasegawa, Appl. Surf. Sci. 234, 387 (2004).

[174] K.J. Choi, H.W. Jang, and J.-L. Lee, Phys. Stat. Sol. C. 1, 835 (2002).

[175] V. Kumar, W. Lu, F.A. Khan, R. Schwindt, E. Piner, and I. Adesida, Elec. Lett. 37, 1483 (2001).

[176] M. Gao, Y. Lin, S.T. Bradley, S.A. Ringel, J. Hwang, W.J. Schaff, and L.J. Brillson, Appl. Phys. Lett. 87, 191906 (2005).

[177] M.D. McCluskey, C.G. Van de Walle, N.M. Johnson, D.P. Bour, and M. Kneissl, Int. Jour. Mod. Phys. B 13, 1363 (1999).

[178] S.P. Grabowski, M. Schneider, H. Nienhaus, W. Monch, R. Dimitrov, O. Ambacher, and M. Stutzmann, Appl. Phys. Lett. 78, 2503 (2001).

[179] V.M. Bermudez, C.-I. Wu, and A. Kahn, Jour. Appl. Phys. 89, 1991 (2001).

[180] D.K. Schroder, Semiconductor Material and Device Characterization, (Wiley-Interscience, New York, 1998).

[181] H.B. Michaelson, Jour. Appl. Phys. 48, 4729 (1977).

[182] H.L. Mosbacker, B.D. White, and L.J. Brillson, unpublished.

[183] J. Osvald, J. Kuzmik, G. Konstantinidis, P. Lobotka, and A. Georgakilas, Microelectron. Eng. 81, 181 (2005).

[184] J.K. Sheu, M.L. Lee, and W.C. Lai, Appl. Phys. Lett. 86, 052103 (2005).

[185] E.D. Readinger, B.P. Luther, S.E. Mohney, and E.L. Piner, Jour. Appl. Phys. 89, 7983 (2001).

[186] C.M. Jeon, H.W. Jang, and J.-L. Lee, Appl. Phys. Lett. 82, 391 (2003).

[187] H. Hasegawa , T. Inagaki, S. Ootomo, and T. Hashizume, Jour. Vac. Sci. Tech. 21, 1844 (2003).

[188] J.W.P. Hsu, K.J. Manfra, R.J. Molnar, B. Heying, and J.S. Speck, Appl. Phys. Lett. 81, 79 (2002).

[189] M. Kuball, J.M. Hayes, M.J. Uren, T. Martin, J.C.H. Birbeck, R.S. Balmer, and B.T. Hughes, IEEE Elec. Dev. Lett. 23, 7 (2002).

[190] M. Kuball, S. Rajasinggam, A. Sarua, M.J. Uren, T. Martin, B.T. Hughes, K.P. Hilton, and R.S. Balmer, Appl. Phys. Lett. 82, 124 (2003).

[191] C.-C. Lee, C.-F. Shih, C.-P. Lee, R.-C. Tu, C.-C. Chuo, and J. Chi, Jpn. Jour. Appl. Phys. 43, L740 (2004).

[192] Y.P. Varshni, Phsyica 39, 149 (1967).

[193] A.P. Young and L.J. Brillson, Appl. Phys. Lett. 77, 699 (2000).

[194] J.W. Johnson, E.L. Piner, A. Vescan, R. Therrien, P. Rajagopal, J.C.Roberts, J.D. Brown, S. Singhal, and K.J. Linthicum, IEEE Elec. Dev. Lett. 25, 459, (2004).

[195] W.G. Perry, M.B. Bremser, and R.F. Davis, Jour. Appl. Phys. 83, 469 (1998).

[196] Y.-J. Lin, Y.-M. Chen, T.-J. Cheng, and Q. Kerr, Jour. Appl. Phys. 95, 571 (2004).

[197] S. Tripathy, A. Ramam, S.J. Chua, J.S. Pan, and A. Huan, Jour. Vac. Sci. & Tech. A 19, 2522 (2001).

[198] T. Hashizume and R. Nakasaki, Appl. Phys. Lett. 80, 4564 (2002).

[199] T. Hashizume and H. Hasegawa, Appl. Surf. Sci. 234, 387 (2004).

[200] Q. Zhou, M.O. Manasreh, M. Pophristic, S. Guo, and I.T. Ferguson, Appl. Phys. Lett. 79, 2901 (2001).

[201] C.M. Jeon and J.-L. Lee, Appl. Phys. Lett. 82, 4301 (2003).

[202] H.L. Mosbacker, Y.M. Strzhemechny, B.D. White, P.E. Smith, D.C. Look, D.C. Reynolds, C.W. Litton, and L.J. Brillson, Appl. Phys. Lett. 87, 012102 (2005).

[203] S. Tumakha, S.H. Goss, L.J. Brillson, R.S. Okojie, Jour. Vac. Sci. & Tech. B 23, 594 (2005).

[204] G.H. Jessen, R. Fitch, J.K. Gillespie, G.D. Via, B.D. White, S.T. Bradley, D.E. Walker, Jr., and L.J. Brillson, Appl. Phys. Lett. 83, 485 (2003).

[205] S.T. Bradley, S.H. Goss, J. Hwang, W.J. Schaff, and L.J. Brillson, Jour. Appl. Phys. 97, 084502 (2005).

[206] S.T. Bradley, S.H. Goss, J. Hwang, W.J. Schaff, and L.J. Brillson, Appl. Phys. Lett. 85, 1368 (2004).

[207] J.I. Pankove, Optical Processes in Semiconductors, (Dover, New York, 1971).

[208] M.A. Reshchikov and H. Morkoc, Jour. Appl. Phys. 97, 061301 (2005).

[209] G.R. James, A.W.R. Leitch, M.C.Wagener, and F. Omnes, Phys. Stat. Sol. (c) 1, 2316 (2004).

[210] K.B. Nam, J. Li, M.L. Nakarmi, J.Y. Lin, and H.X. Jiang, Appl. Phys. Lett. 81, 1038 (2002).

[211] M.C. Wagener, G.R. James, A.W.R. Leitch, and F. Omnes, Phys. Stat. Sol. (c) 1, 2322 (2004).

[212] K.B. Nam, M.L. Nakarmi, J.Y. Lin, and H.X. Jiang, Appl. Phys. Lett. 86, 222108 (2005).

[213] M.C. Wagener, G.R. James, and F. Omnes, Appl. Phys. Lett. 83, 4193 (2003).

[214] S.M. Myers and C.H. Seager, Jour. Appl. Phys. 97, 093517 (2005).

[215] N. Nepal, K.B. Nam, M.L. Nakarmi, J.Y. Lin, H.X. Jiang, J.M. Zavada, and R.G. Wilson, Appl. Phys. Lett. 84, 1090 (2004).

[216] A. Ionascit-Nedelcescu, C. Carlone, A. Houdayer, H.J. von Bardeleben, J.-L. Cantin, and S. Raymond, IEEE Trans. Nucl. Sci. 49, 2733 (2002).

[217] M.D. McCluskey, N.M. Johnson, C.G. Van de Walle, D.P. Bour, M. Kneissl, and W. Walukiewicz, Phys. Rev. Lett. 80, 4008 (1998).

[218] Y. Nakano, O. Fujishima, T. Kachi, K. Abe, O. Eryu, K. Nakashima, and T. Jimbo, Jour. Electrochem. Soc. 151, G801 (2004).

[219] Q. Zhou, M.O. Manasreh, M. Pophristic, S. Guo, and I.T.Ferguson, Appl. Phys. Lett. 79, 2901 (2001).

[220] G. Popovici, W. Kim, A. Botchkarev, H. Tang, H. Morkoc, and J. Solomon, Appl. Phys. Lett. 71, 3385 (1997).

[221] H. Hasegawa and S. Oyama, Jour. Vac. Sci. Technol. B 20, 1647 (2002).

[222] J.E. Northrup, Appl. Phys. Lett. 78, 2288 (2001).

[223] E.J. Miller, D.M. Schaadt, E.T. Yu, C. Poblenz, C. Elsass, and J.S. Speck, Jour. Appl. Phys. 91, 9821 (2002).

[224] T. Wu, Z.-B. Hao, G. Tang, and Y. Luo, Jpn. Jour. Appl. Phys. 42, L257 (2003).

[225] C.B. Soh, S.J. Chua, H.F. Lim, D.Z.Chi, W. Liu, and S. Tripathy, Jour. Phys.: Condens. Matt. 16, 6305 (2004).

[226] A.V. Vertiatchikh and L.F. Eastman, IEEE Elec. Dev. Lett. 24, 535 (2003).